AIR, WATER AND SOIL POLLUTION SCIENCE AND TECHNOLOGY

INDOOR AIR QUALITY

CONTROL, HEALTH IMPLICATIONS AND CHALLENGES

ROBERT M. RIDGWAY
EDITOR

NOVA

Air, Water and Soil Pollution Science and Technology

Air, Water and Soil Pollution Science and Technology

Urban Air Pollution and Avenue Trees: Benefits, Interactions and Future Prospects
Abhijit Sarkar, PhD (Editor), Sujit Das
2021. ISBN: 978-1-68507-175-2 (Hardcover)
2021. ISBN: 978-1-68507-474-6 (eBook)

Soil Conservation: Strategies, Management and Challenges
António Avelino Batista Vieira (Editor),
António José Bento Gonçalves (Editor)
2021. ISBN: 978-1-53619-513-2 (Hardcover)
2021. ISBN: 978-1-53619-600-9 (eBook)

Air Pollution: Effects and Dangers
Jorge Esteban Colman Lerner (Editor)
2021. ISBN: 978-1-53619-544-6 (Hardcover)
2021. ISBN: 978-1-53619-556-9 (eBook)

Air Quality Observation in the U.S.: Systems, Needs, and Standards
Malcolm Parisi (Editor)
2014. ISBN: 978-1-63117-154-3 (Hardcover)
2014. ISBN: 978-1-63117-164-2 (eBook)

Air Quality: Environmental Indicators, Monitoring and Health Implications
Arthur Hermans (Editor)
2013. ISBN: 978-1-62808-259-3 (Hardcover)
2013. ISBN: 978-1-62808-260-9 (eBook)

More information about this series can be found at
https://novapublishers.com/product-category/series/air-water-and-soil-pollution-science-and-technology/

Robert M. Ridgway
Editor

Indoor Air Quality

Control, Health Implications and Challenges

Library of Congress Cataloging-in-Publication Data

ISBN: 979-8-88697-181-1 (e-book)

Published by Nova Science Publishers, Inc. † New York

Contents

Preface vii

Chapter 1 **Prediction of Heat Ventilation in Solar Air Heater Systems** 1
Bdis Bakri, Ahmed Ketata, Slah Driss, Hani Benguesmia and Zied Driss

Chapter 2 **Air Pollution in Primary Educational Environments in a European Context** 37
K. Slezakova, B. Kotlík and M. C. Pereira

Chapter 3 **Computational Study and Experimental Validation of Heat Ventilation in a Box Prototype** 53
Bdis Bakri, Slah Driss, Ahmed Ketata, Hani Benguesmia and Zied Driss

Chapter 4 **Ventilation System Performance in a Heated Room Testing the Indoor Air Quality and Thermal Comfort**.....77
Sondes Ifa and Zied Driss

Chapter 5 **Evaluation of Airflow in Spaces Equipped with Vertical Confluent Jets Ventilation Systems**.....101
Eusébio Conceição, Mª Inês Conceição, João Gomes, Mª Manuela Lúcio and Hazim Awbi

Index 115

Preface

This book includes five chapters that explore the topic of indoor air quality from several perspectives. Chapter One investigates the efficiency of a solar air heater system. Chapter Two examines the effect of indoor air pollution in child populations in educational settings. Chapter Three studies the impact of numerical parameters on heat ventilation in a box prototype. Chapter Four includes simulations of airflow related to a room containing a sitting person and a computer to determine ventilation system performance. Lastly, Chapter Five analyzes airflow in spaces equipped with a vertical confluent jets ventilation system.

Chapter 1 - In this chapter, the authors are interested on the design and the realization of a new solar air heater test bench to investigate the efficiency of the solar system. The considered test bench consists of two passages solar air heater separated by an absorber and powered by a fan working in a delivery mode. On the glass side, it is connected to the box prototype through a pipe. On this system, a glass is hanging on the front side and an absorber is inserted inside. The hot air flow is routed towards the box prototype. Two circular holes are located in the same face of the box prototype. The inlet hole allows the hot air supply. However, the outlet hole allows its escape into the ambient environment. Indeed, the authors have developed numerical simulations to study the turbulent flow in the considered test bench over the day. In these conditions, it has been observed a decrease in the flow and an appearance of the recalculation zones in the first passage. This phenomenon is more prominent during the transition of the flow to the second passage. However, the flow becomes uniform until the exit of the solar air heater. Via the pipe separating the solar air heater from the box prototype, a discharge area appears in the hole inlet and invaded the reverse wall. By comparing the local characteristics for the different instances, a similar appearance has been observed with a maximum value at t=12 hours. For the magnitude velocity, a small difference between the calculated values has been noted. However, this difference is more clear for the temperature distribution and the turbulent

characteristics. For the energy efficiency, it presents very low values at the beginning of the day. With the increase of the temperature through the day, there is a gradual increase of the energy efficiency until t=12 hours, with a value equal to η= 31,8%. This technology will be very useful since it can provide sustainable energy and substitute the expensive traditional technologies.

Chapter 2 - As the modern population grows, most residents live in cities with inadequate ambient air quality. While daily exposure to outdoor air pollution is inevitable, people spend most of their time indoors. Thus, indoor air quality (IAQ) has significant impacts on human health, possibly leading to greater risks than outdoor pollution, which is especially relevant for susceptible populations. Children spend a large part of their daily time in education settings (such as nurseries, kindergartens, preschools, primary and elementary schools). The respective indoor air quality is a significant parameter for their health. However, despite the relevance of these specific environments, the current knowledge concerning the respective levels of pollution and child exposures is far from comprehensive. The present chapter introduces the topic of indoor air pollution in child populations. It outlines the relevance of child education settings, emphasizing large-scale studies conducted in primary schools within the European context.

Chapter 3 - In this chapter, the impact of the numerical parameters on the heat ventilation was studied in a box prototype. Particularly, a computational study and an experimental validation have been developed to compare the standard k-ω turbulence model, the BSL k-ω turbulence model, the SST k-ω turbulence model, the standard k-ε turbulence model, the RNG k-ε turbulence model and the Realizable k-ε turbulence model. From the obtained results, it is noticed that the aerodynamic characteristics present the same emergence nevertheless the maximum values depend on the turbulence model. Particularly, it has been noted that the value founded with the standard k-ω turbulence model is nearest to the experimental results. This study tends to show that the standard k-ω turbulence model is the most efficient to study the air flow in the box prototype. For this model, the meshing effect on the CFD results was studied to choose the adequate mesh with a minimum calculated time. The numerical results were compared using experimental results developed in the authors' laboratory. The good agreements confirm the numerical method.

Chapter 4 - In relation with the study of the indoor air quality (IAQ) and the thermal comfort, the main goal of the major researches was the prediction of the thermal sensation for the existing persons in daily and working spaces.

In this chapter, the authors are interested on the numerical simulations in room containing a sitting person and computer. The considered study uses the computational fluid dynamic (CFD) tool. In this case, ANSYS Fluent 17. software was employed. It is based on the resolution of the Navier Stokes equation using the finite volume method. The distribution of the temperature, velocity, turbulent kinetic energy, turbulent viscosity and dissipation rate were evaluated in different visualization directions and planes. Similarly, the indoor thermal comfort was tested by determining the predicted mean vote (PMV). The developed numerical results demonstrate that the presence of the heat sources affects the indoor air flow. Indeed, it causes the perturbation of the air flow and the non-homogeneity of the air characteristic. In addition, the thermal sensation is slightly hot. The adequate mesh and turbulence model are in good accord with the experimental data found from the literature.

Chapter 5 - In this research the evaluation of airflow in spaces equipped with vertical confluent jets ventilation system is analyzed. The influence of the airflow rate in the airflow topology, namely the air velocity field and the air quality acceptable airflow rate, is analyzed. This vertical confluent jets ventilation system consists of two sets of 50 nozzles located in a horizontal inlet ventilation ducts system, placed on each of the opposite walls. The horizontal inlet ventilation ducts system is placed near the wall surface, at 1.8m high. The exhaust of the vertical confluent jets ventilation system is made in the lower area of a vertical duct placed in the central area of the occupation area. The exhaust area is placed at 1.5 m high. Three different airflow rates are analyzed. The first, second and third airflow rate guarantee an acceptable airflow rate, according to international standards, for 4.7, 5.8 and 7.0 persons. The two sets of 50 nozzles guarantee a uniform airflow at the bottom of the wall. For all airflow rates, considering the current design, the air velocity field promotes good air distribution along the floor. The interaction between the different airflows in the occupied central zone causes an upward flow of air towards the exhaust zone.

Chapter 1

Prediction of Heat Ventilation in Solar Air Heater Systems

Bdis Bakri[1], Ahmed Ketata[2], Slah Driss[2], Hani Benguesmia[3] and Zied Driss[2,*]

[1]Mechanical Engineering Department,
Faculty of Technology,
University of M'sila, M'sila, Algeria
[2]Laboratory of Electro-Mechanic Systems (LASEM),
National School of Engineers of Sfax (ENIS),
University of Sfax (US), Sfax, Tunisia
[3]LGE Laboratory,
Electrical Engineering Department,
Faculty of Technology,
University of M'sila, M'sila, Algeria

Abstract

In this chapter, we are interested on the design and the realization of a new solar air heater test bench to investigate the efficiency of the solar system. The considered test bench consists of two passages solar air heater separated by an absorber and powered by a fan working in a delivery mode. On the glass side, it is connected to the box prototype through a pipe. On this system, a glass is hanging on the front side and an absorber is inserted inside. The hot air flow is routed towards the box prototype. Two circular holes are located in the same face of the box prototype. The inlet hole allows the hot air supply. However, the outlet hole allows its escape into the ambient environment. Indeed, we have developed numerical simulations to study the turbulent flow in the

* Corresponding Author's Email: zied.driss@enis.tn.

In: Indoor Air Quality
Editor: Robert M. Ridgway
ISBN: 979-8-88697-134-7

considered test bench over the day. In these conditions, it has been observed a decrease in the flow and an appearance of the recalculation zones in the first passage. This phenomenon is more prominent during the transition of the flow to the second passage. However, the flow becomes uniform until the exit of the solar air heater. Via the pipe separating the solar air heater from the box prototype, a discharge area appears in the hole inlet and invaded the reverse wall. By comparing the local characteristics for the different instances, a similar appearance has been observed with a maximum value at t=12 hours. For the magnitude velocity, a small difference between the calculated values has been noted. However, this difference is more clear for the temperature distribution and the turbulent characteristics. For the energy efficiency, it presents very low values at the beginning of the day. With the increase of the temperature through the day, there is a gradual increase of the energy efficiency until t=12 hours, with a value equal to η= 31,8%. This technology will be very useful since it can provide sustainable energy and substitute the expensive traditional technologies.

Keywords: solar air heater, sustainable energy, ventilation, aerodynamic structure, CFD

1. Introduction

The use of the solar energy in heat ventilation is widely applied, such as hospitals, residential and commercial buildings. The objective is to minimize energy consumption with the use of renewable energy [1-21]. In this context, Yang et al. [22] designed a solar air heater with offset strip fins optimized by numerical modeling. Then, a series of experiments based on ASHRAE Standard 93-2003 was conducted to test the detailed thermal performance of the heater in the light of time constant, thermal efficiency, incident angle modifier and the synthetically resistance coefficient. Altaa et al. [23] compared three different types of designed flat-plate solar air heaters, two having fins and the other without fins. One of the heater with a fin had single glass cover and the others had double glass covers. Based on the energy output rates, heater with double glass covers and fins is more effective and the difference between the input and output air temperature is higher than of the others. Zukowski [24] presented a novel construction of a forced air solar heater based on a confined single slot jet of air impinging on the flat surface of an absorber plate. The results of experimental research showed that the efficiency of energy conversion ranges from 66% up to 90%. El-Sebaii et al.

[25] developed a comparison between the measured outlet temperatures of flowing air, temperature of the absorber plate and output power of the double pass-finned and v-corrugated plate solar air heaters. The results confirmed that the double pass v-corrugated plate solar air heater is 9.3–11.9% more efficient compared to the double pass-finned plate solar air heater. Wazed et al. [26] confirmed that the fabricated solar air heater is working efficiently. Esen [27] presented an experimental energy and exergy analysis for a novel flat plate SAH with several obstacles and without obstacles. The results confirm that the optimal value of efficiency is a middle level of absorbing plate in flow channel duct for all operating conditions. The double-flow collector supplied with obstacles appears significantly better than that without obstacles. Based on these previous studies, it is clear that the use of the SAH system with the double pass is more efficient. For this, we focused our attention on the study of a new SAH system with double pass designed and realized in our laboratory. In the present chapter, we are interested on the prediction of the heat ventilation and the experimental validation with the considered test bench.

2. Solar Air Heater System

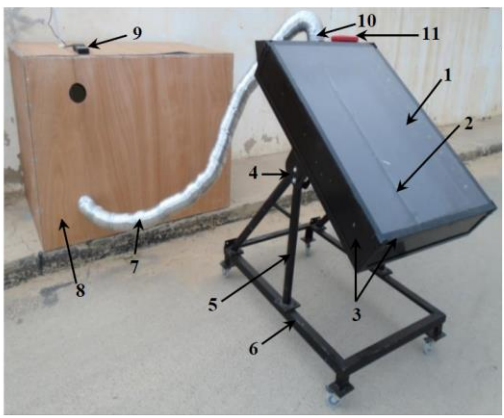

N°	Designation
1	Glass cover
2	Absorber plate
3	Insulation
4	Clevis
5	Mounting brackets
6	Mobile base
7	Duct
8	Box prototype
9	Anemometer
10	Fan
11	Multi meter

Figure 1. Solar air heater test bench.

Figure 1 presents the new solar air heater test bench designed and realized in our LASEM laboratory to investigate the efficiency of the solar system. The considered system consists of a two passages solar air heater separated by an absorber and powered by a fan working in a delivery mode and placed in the

inlet, side the insulation. On the glass side, it is connected to the box prototype through a pipe.

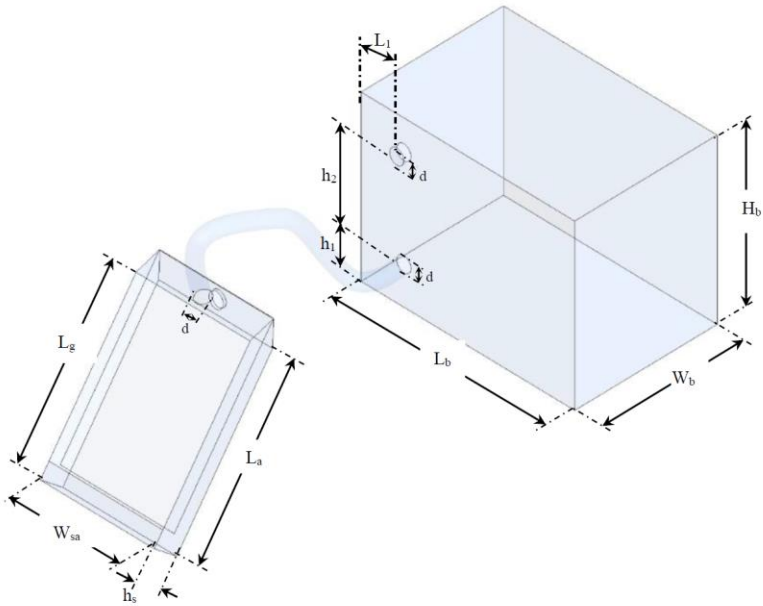

Parameters	Value(mm)
Length of the box prototype L_b	1500
Height of the box prototype H_b	1100
Width of the box prototype W_b	1000
Longitude of the holes L_1	300
Length of the absorber L_a	1086
Length of the glass L_g	1000
Width of the solar air heater W_s	778
Height of the solar air heater h_s	194
Altitude of the holes inlet h_1	250
Distance between of the two holes h_2	900
Diameters of the holes d	100

Figure 2. Geometrical arrangements.

The geometrical arrangements of the computational domain are presented in Figure 2, which is composed of two domains separated by a circular pipe with a diameter d=100 mm. The first one is the solar air heater with a height h_s=194 mm and a width W_s=778 mm. On this system, a glass is hanging on the front side with a length L_g=1000 mm and an absorber is inserted inside

with a length L_a=1086 mm. The hot air flow is routed towards the box prototype with a length L_b=1500 mm, a height H_b=1100 mm and a width W_b=1000 mm. Two circular holes, with a distance h_2=900 mm, are located in the same face of the box prototype. The inlet holes, placed in the altitude h_1=250 mm and a longitude L_1=300 mm, allows the hot air supply. However, the outlet hole allows its escape into the ambient environment.

3. Numerical Model

3.1. Boundary Conditions

A boundary condition is required anywhere fluid enters or exits the system and can be set as a pressure inlet, mass flow inlet, interior, internal or interface. General interpretation was given on the basis of numerical simulation of the solar air heater. A physical model was simulated using ANSYS Fluent 17.0, based on the geometrical dimensions of the solar air heater. The boundary conditions are illustrated in Figure 3. Wall boundary was applied for the solar air heater with heat flux of value equal zero to obtain the adiabatic wall. Wall boundary was used for the absorber and the mirror and convective heat transfer option was applied for different parts of the device such as glass and absorber. For the inlet velocity, it has been taken a magnitude velocity equal to V=3 $m.s^{-1}$. For the pressure outlet, a value of p=101325 Pa is set. This means that at this opening the fluid exits the model to an area of static atmospheric pressure condition.

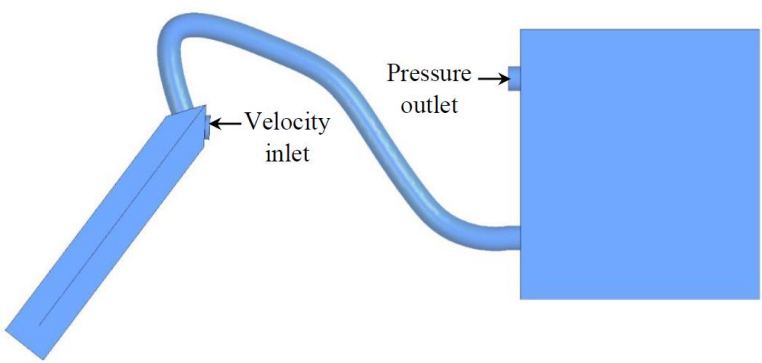

Figure 3. Boundary conditions.

3.2. Meshing

The automatically generated mesh is usually appropriate and intricate problems with thin and small meshing. Geometrical and physical features can result in extremely high number of cells, for which the computer memory is too small. “Meshing” options allow us to manually adjust the computational mesh to solve problems features and to resolve them better. In this application, we have adopted the refined model consisting of a maximum number of cells equal to N=1578369 cells that gives the lower numerical diffusion inside the solar air heater with an unstructured and tetrahedral meshing as presented in Figure 4.

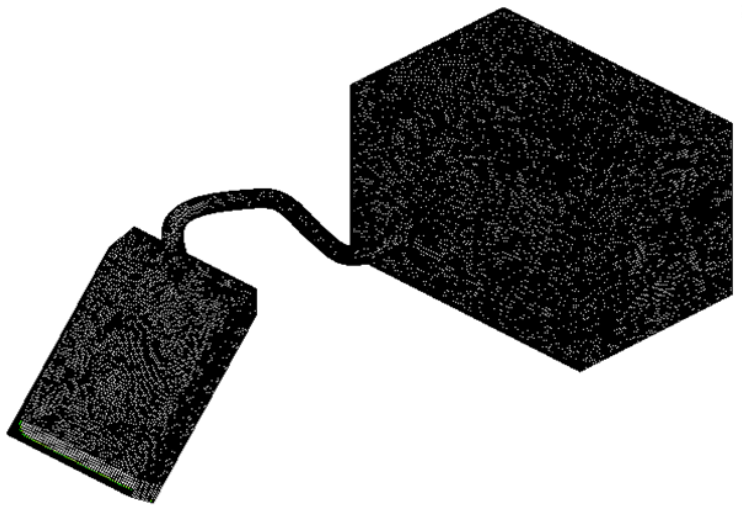

Figure 4. Meshing of the computational domain.

4. Results and Discussion

The distribution of the velocity fields, the temperature, the Do irradiation, the total pressure, the turbulent kinetic energy, the turbulence eddy frequency and the turbulent viscosity are presented in this section. In our case, the Reynolds number is evaluated to be equal to Re=20000. Particularly, we have considered different longitudinal and transverse planes for the first and second passages of the solar air heater supplying the box prototype, as presented in Figure 5.

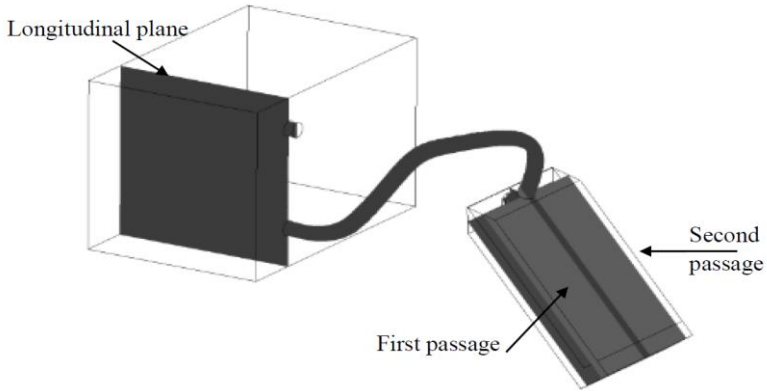

Figure 5. Visualization planes.

4.1. Velocity Fields

Figures 6, 7 and 8 show the velocity fields distribution in the different longitudinal and transverse planes for the first and second passages of the solar air heater supplying the box prototype at t=10 hours, t=12 hours, t=14 hours and t=16 hours. According to these results, it is clear that the velocity fields present the same distribution at the different considered instances. For example, at t=12 hours the inlet velocity is governed by the boundary condition defined by V=3 $m.s^{-1}$. In the first passage, a decrease in the flow has been observed and a recirculation zone is created. This phenomenon is more prominent during the transition of the flow to the second passage. In this side, the flow becomes uniform until the exit of the solar air heater.

Indeed, the velocity reaches a very important value equal to V=5 $m.s^{-1}$. Via the pipe separating the solar air heater from the box prototype, a discharge area appears in the hole inlet and invaded the reverse wall. At this level, the velocity changes his direction and two axial flows have been observed. The first ascending flow is responsible on the recirculation zone appeared in the wholes area of the box prototype. This movement continues until the exit of the air flow through the hole outlet and reaches the maximum value equal to V=4 $m.s^{-1}$. The second descending flow is due to the dead zone appeared in the down area. Globally, the averaged velocity value is about V=1.5 $m.s^{-1}$ in the discharge area. Elsewhere, the averaged velocity presents a very low value. By comparing the velocity fields for the different instances, it is clear that the maximum value of the average velocity is obtained at t=12 hours. For the other

instances, the magnitude velocity decreases and the minimum values are obtained at t=16 hours.

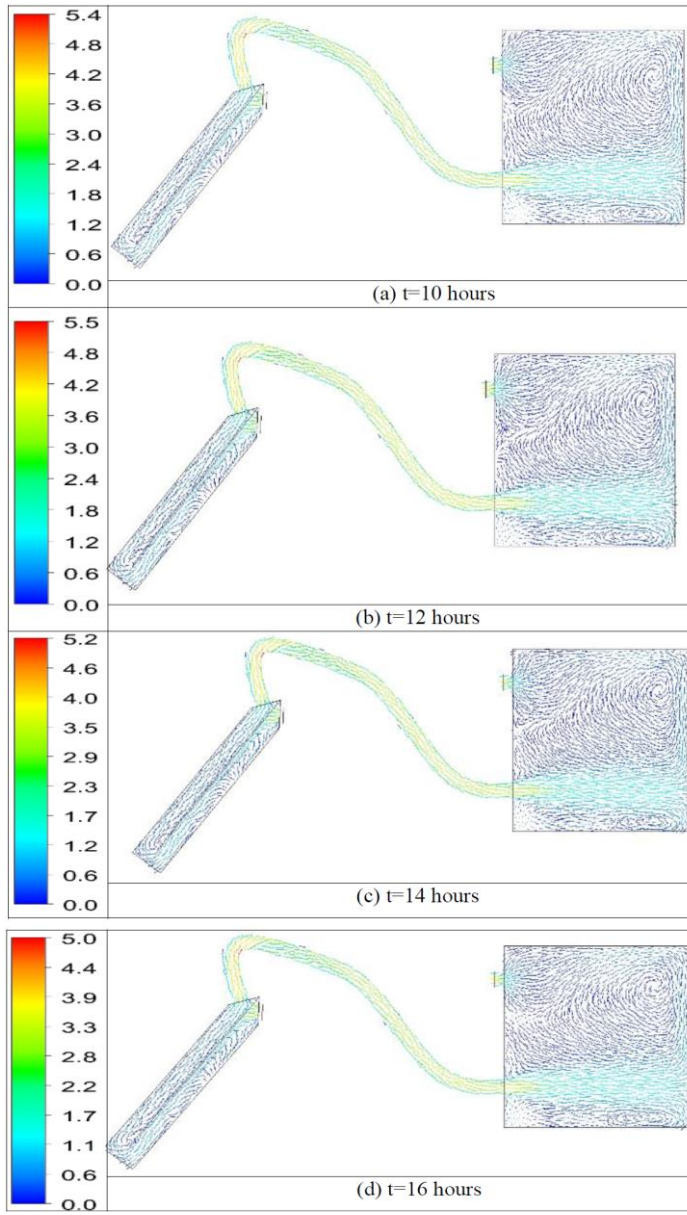

Figure 6. Distribution of the velocity fields in the longitudinal plane.

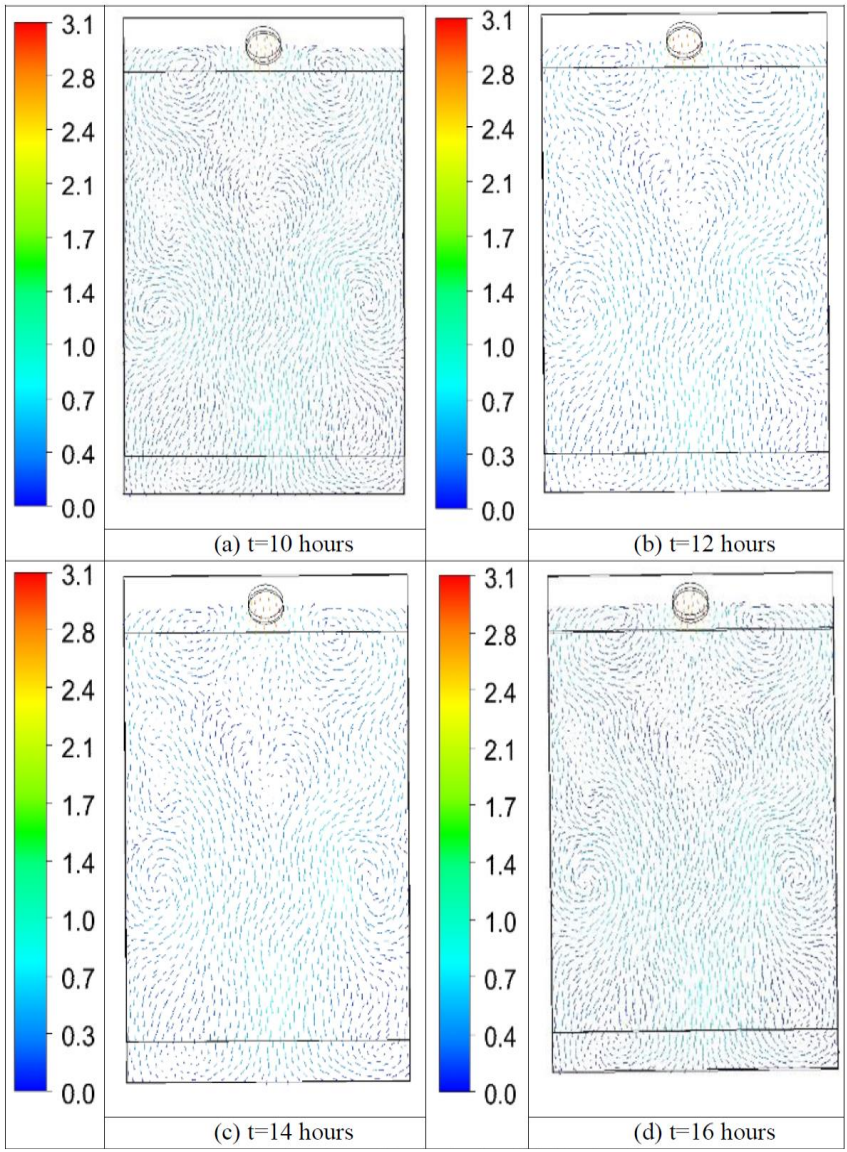

Figure 7. Distribution of the velocity field in the first passage.

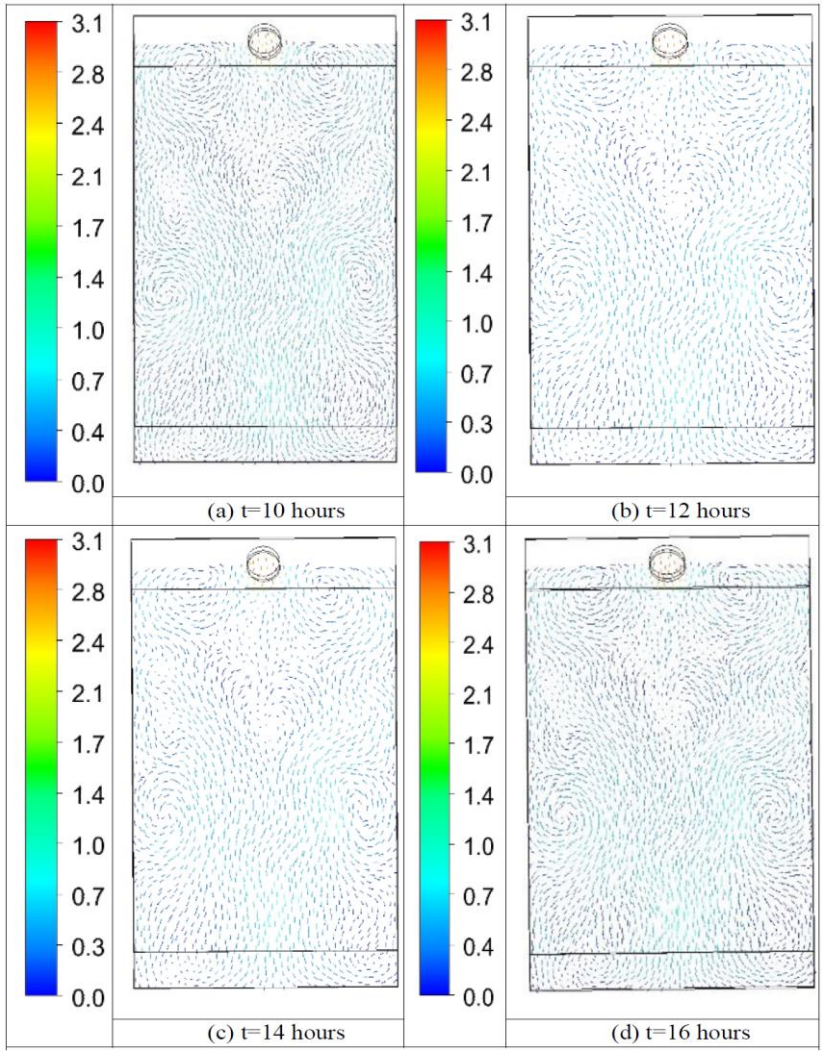

Figure 8. Distribution of the velocity field in the second passage.

4.2. Temperature

Figures 9, 10 and 11 show the distribution of the temperature in the different longitudinal and transverse planes for the first and second passages of the solar air heater supplying the box prototype at t=10 hours, t=12 hours, t=14 hours

and t=16 hours. According to these results, it is clear that the temperature presents the same distribution at the different considered instances. For example, at t=12 hours it has been noted that the inlet temperature is governed by the boundary condition defined by T=308 K. This value increases immensely and reaches an average value equal to T=338 K in the first passage and T=347 K in the second passage. This fact can be explained by the air flow incoming at ambient temperature and flowing the channel between the absorber plane and the insulation, which starts warming up by the convection with the absorber. In the second passage, the temperature of the air flow is more important since the flowing between the glass and the absorber is affected by the solar radiations. Thereby, the box prototype is powered by a continuous air heater characterized by the maximum temperature value equal to T=349 K. By comparing the temperature for the different instances, it is clear that the maximum value of the temperature is obtained at t=12 hours. For the other instances, the temperature decreases and the minimum values are obtained at t=16 hours. At this instance, the maximum value of the temperature is equal to T=340 K.

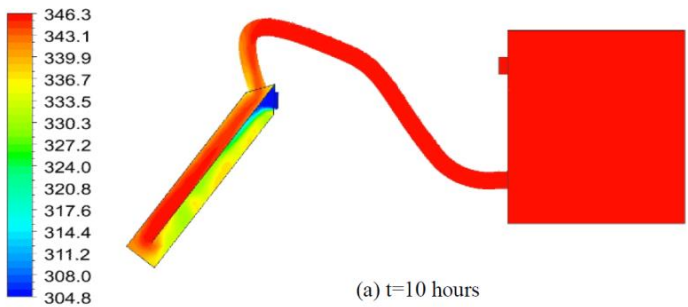

(a) t=10 hours

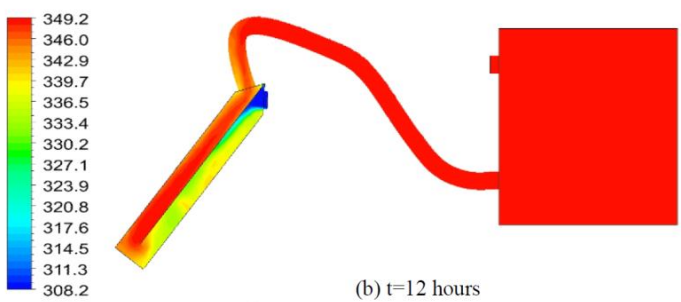

(b) t=12 hours

Figure 9. (Continued onto next page).

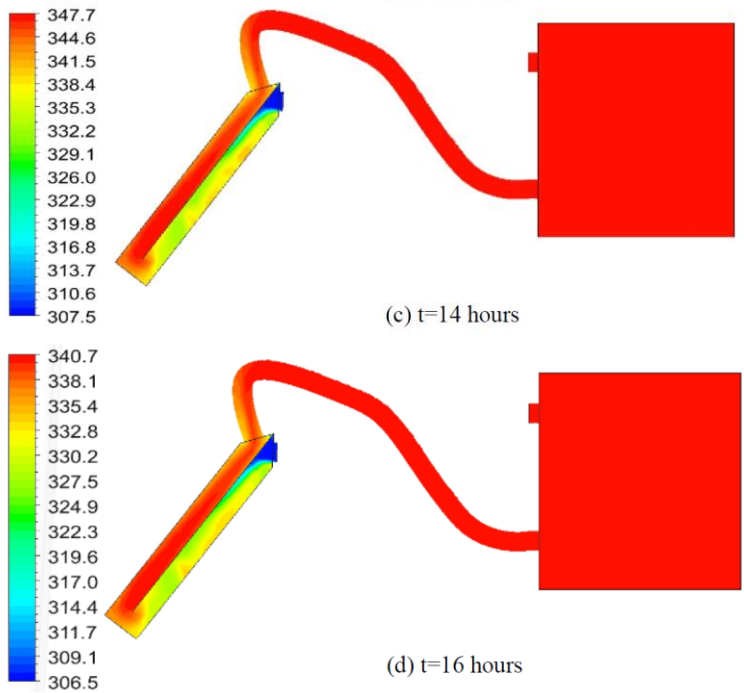

Figure 9. Distribution of the temperature in the longitudinal plane.

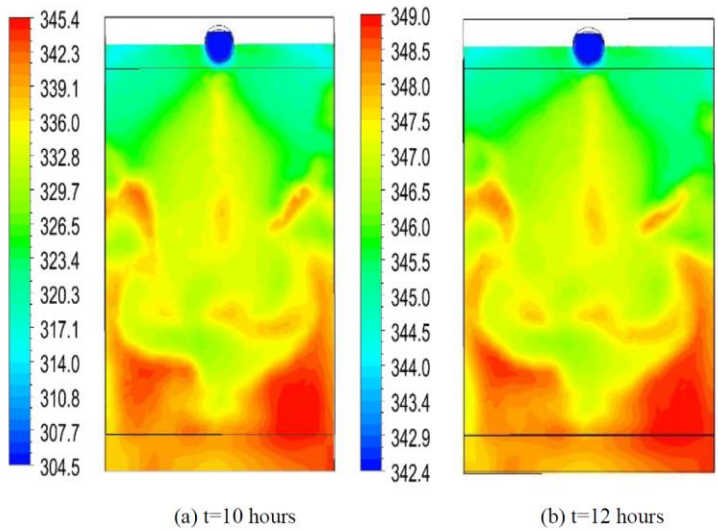

Figure 10. (Continued onto next page).

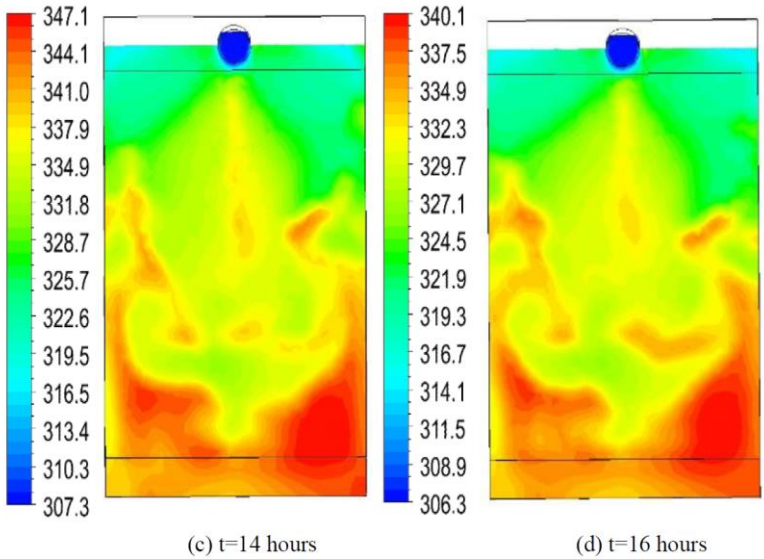

Figure 10. Distribution of the temperature in the first passage.

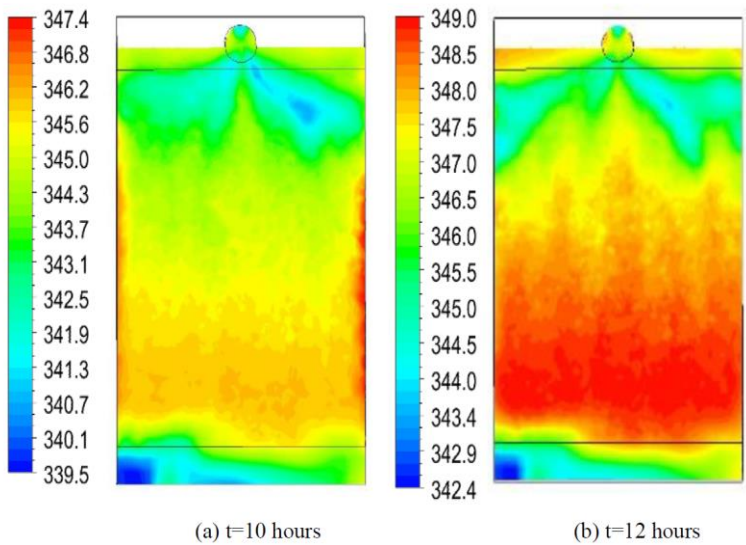

Figure 11. (Continued onto next page).

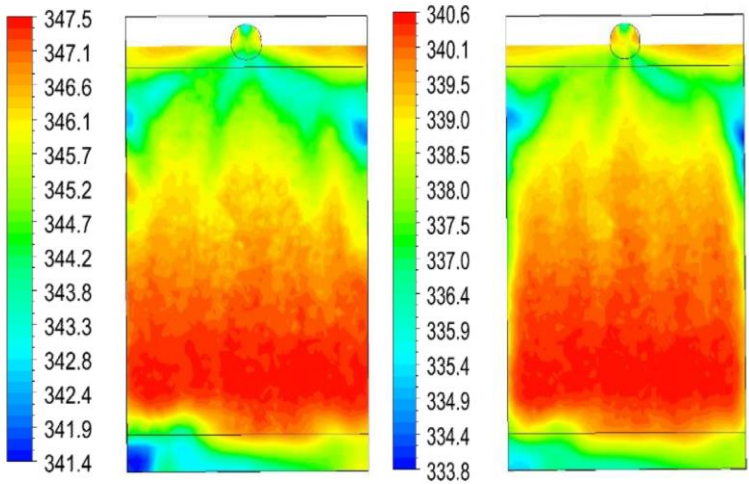

Figure 11. Distribution of the temperature in the second passage.

4.3. Distribution of the Do Irradiation

Figures 12, 13 and 14 show the distribution of the Do irradiation in the different longitudinal and transverse planes for the first and second passages of the solar air heater supplying the box prototype at t=10 hours, t=12 hours, t=14 hours and t=16 hours. From these results, it is clear that the Do irradiation presents the same distribution at the different considered instances. For example, at t=12 hours it has been observed that the Do irradiation presents a low value equal to I=2500 $W.m^{-2}$ in the inlet of the solar air heater. This value increases immensely and reaches the maximum value I=3375 $W.m^{-2}$ near the absorber in the second mid-plane of the first passage of the solar air heater. In the second passage a gradual decrease of the Do irradiation has been observed with an average value equal to I=3200 $W.m^{-2}$. The minimum value of the Do irradiation equal to I=2650 $W.m^{-2}$ has been observed in the second mid-plane of the second passage of the solar air heater. From the inlet of the pipe, attached to the solar air heater, the Do irradiation reaches the maximum value equal to I=3375 $W.m^{-2}$ in all the field of the box prototype. By comparing the Do irradiation for the different instances, it is clear that the maximum value of the Do irradiation is obtained at t=12 hours. For the other instances, the Do irradiation decreases and the minimum values are obtained at t=16 hours. At

this instance, the maximum value of the Do irradiation is equal to I=3060 $W.m^{-2}$.

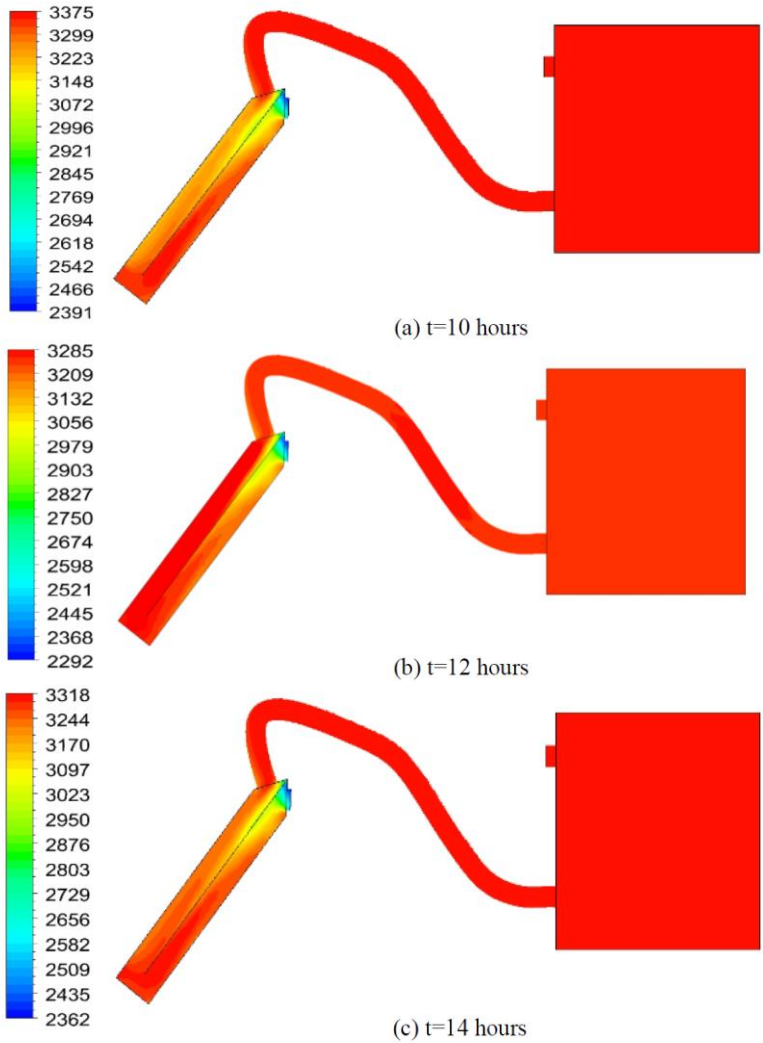

Figure 12. (Continued onto next page).

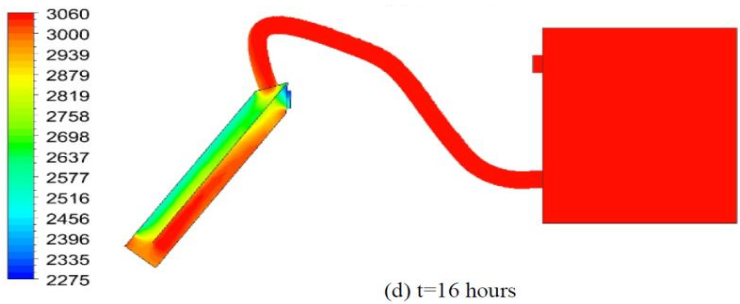

Figure 12. Distribution of the Do Irradiation in the longitudinal plane.

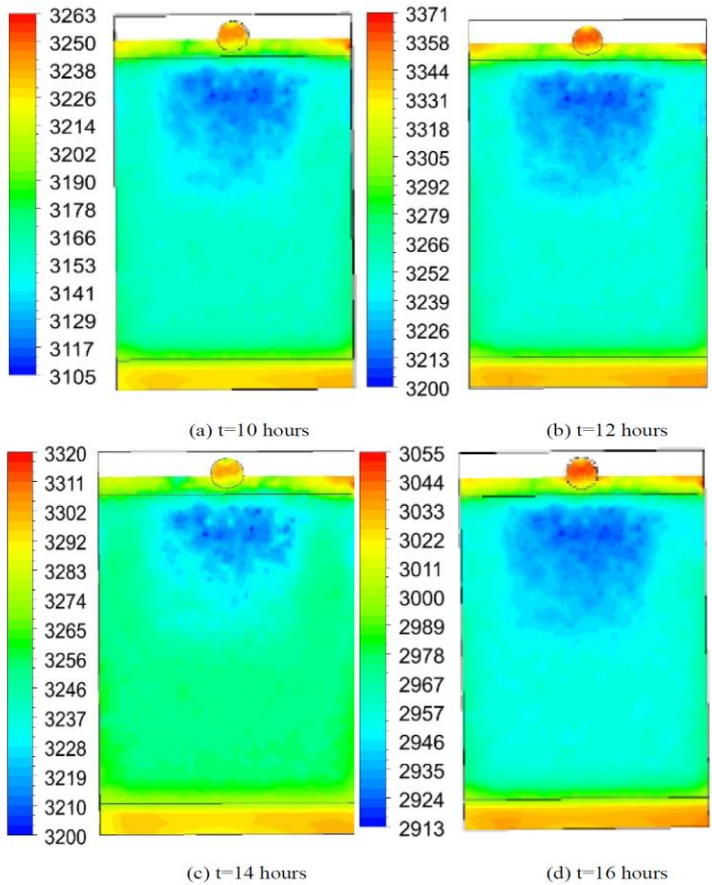

Figure 13. Distribution of the Do Irradiation in the first passage.

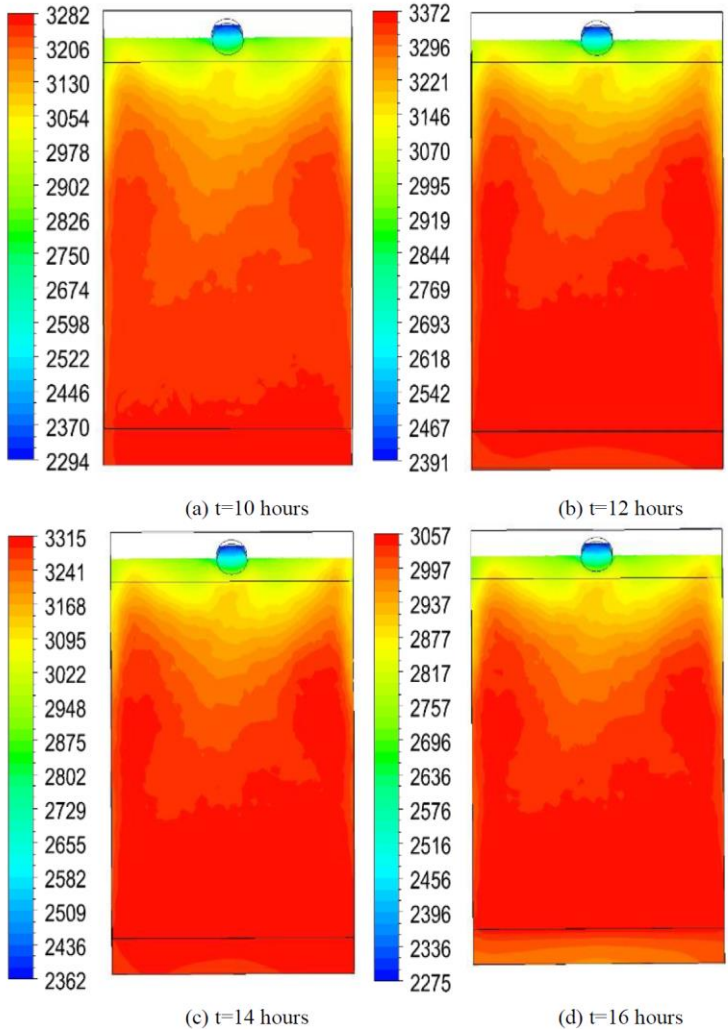

Figure 14. Distribution of the Do Irradiation in the second passage.

4.4. Total Pressure

Figures 15, 16 and 17 show the distribution of the total pressure in the different longitudinal and transverse planes for the first and second passages of the solar air heater supplying the box prototype at t=10 hours, t=12 hours, t=14 hours and t=16 hours. From these results, it is clear that the total pressure presents

the same distribution at the different considered instances. For example, at t=12 hours a compression zone characteristic of the maximum value of the total pressure has been observed in the collector inlet. Then, the total pressure decreases and presents a stabilized value, equal to p=101365 Pa, in the remaining domain of the two passages of the solar air heater. At the exit of the second passage, the total pressure continues decreasing along the pipe and reaches a value equal to p=101347 Pa in the inlet of the box prototype. Through the air advancement, the total pressure decreases quietly in the expulsion area, produced from the hole inlet and invaded until the reverse wall. This fact can be explained by the recirculation zone appeared in the wholes area of the box prototype. In the hole outlet, a depression zone characteristic of the minimum value, equal to p=101327 Pa, has been observed. By comparing the total pressure for the different instances, it is clear that the maximum value of the total pressure is obtained at t=12 hours and it is equal to p=101372 Pa. For the other instances, the total pressure decreases and the minimum values are obtained at t=16 hours. At this instance, the maximum value of the total pressure is equal to p=101351 Pa.

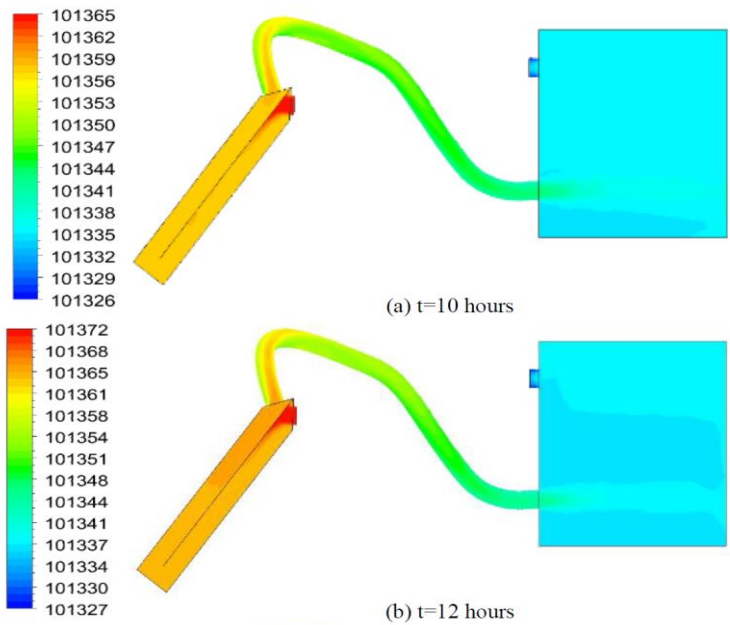

Figure 15. (Continued onto next page).

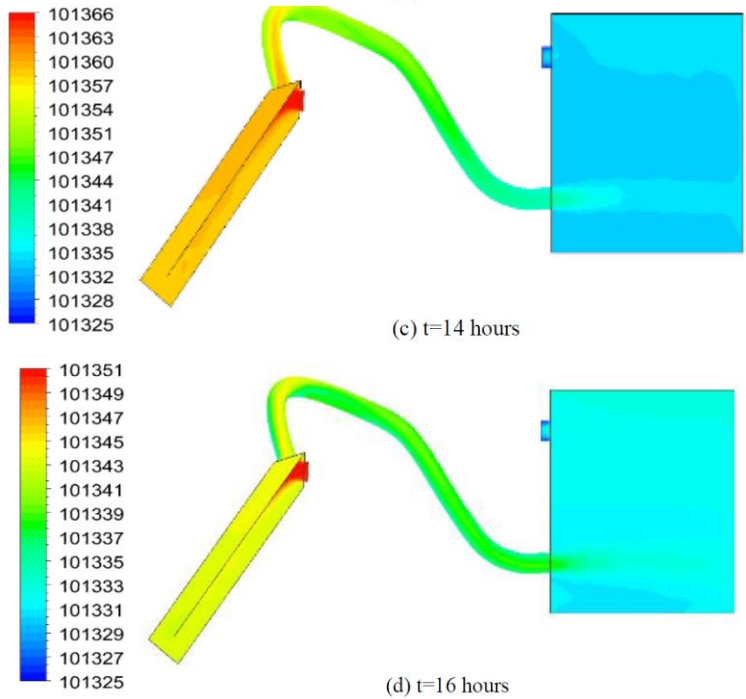

Figure 15. Distribution of the total pressure in the longitudinal plane.

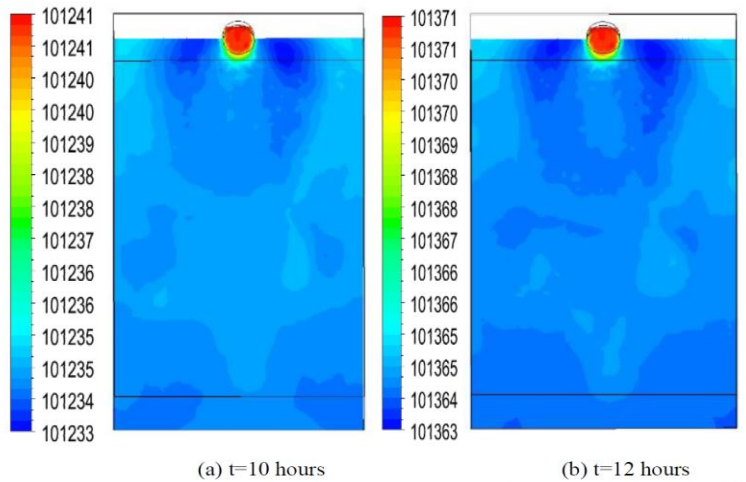

Figure 16. (Continued onto next page).

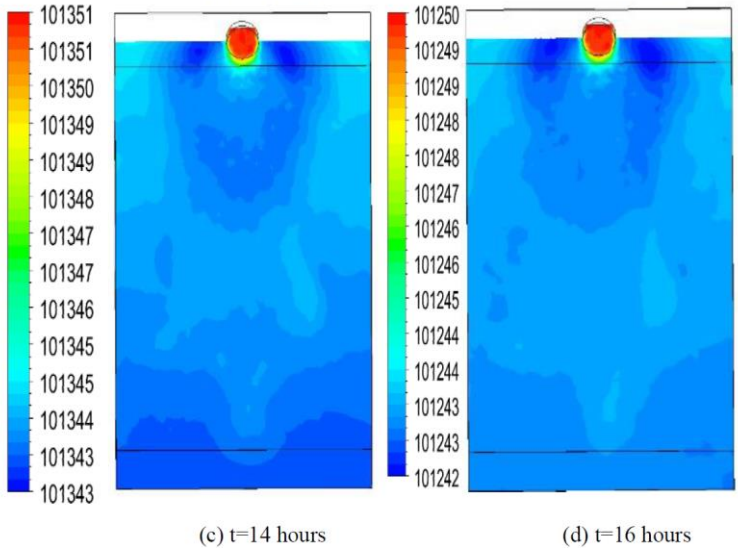

Figure 16. Distribution of the total pressure in the first passage.

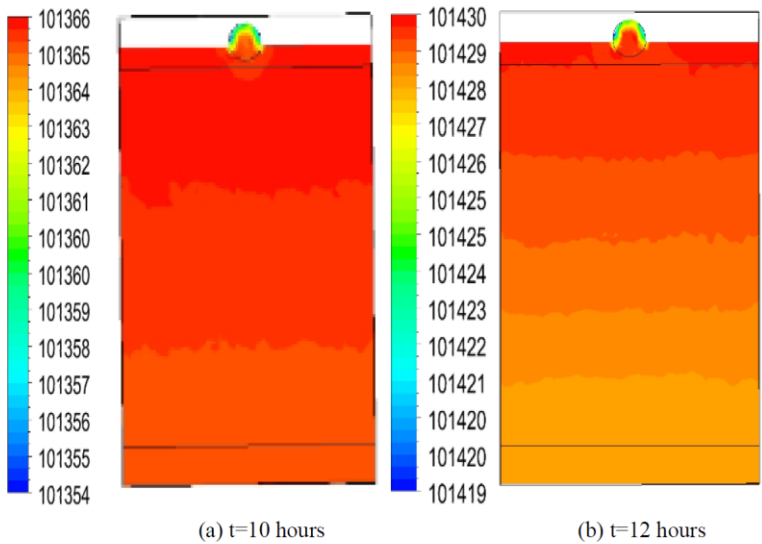

Figure 17. (Continued onto next page).

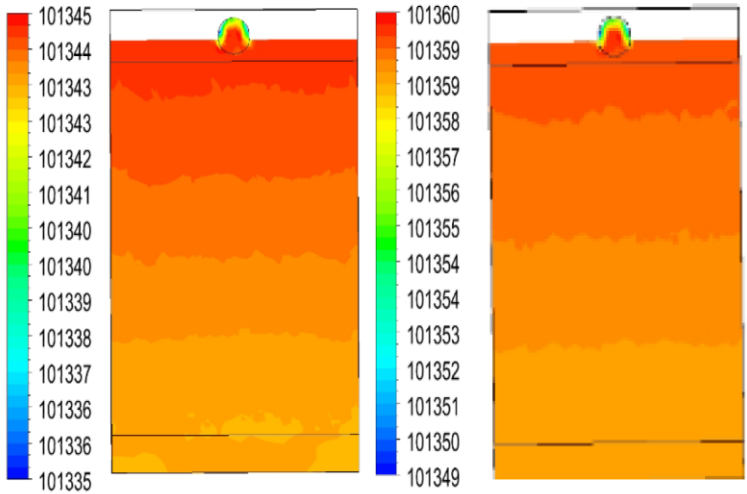

Figure 17. Distribution of the total pressure in the second passage.

4.5. Turbulent Kinetic Energy

Figures 18, 19 and 20 show the distribution of the turbulent kinetic energy in the different longitudinal and transverse planes for the first and second passages of the solar air heater supplying the box prototype at t=10 hours, t=12 hours, t=14 hours and t=16 hours. According to these results, it is clear that the turbulent kinetic energy presents the same distribution at the different considered instances. For example, at t=12 hours a wake zone characteristic of the maximum value of the turbulent kinetic energy has been observed around the collector inlet of the solar air heater. This wake is expanded in the first passage near the absorber side and until the mid-plane. In these conditions, the maximum value of the turbulent kinetic energy is equal to $k=0.98\ m^2.s^{-2}$. Away from this area, the turbulent kinetic energy presents a very weak value excepting the lower leading edge of the absorber, where the turbulent kinetic energy is equal to $k=0.09\ m^2.s^{-2}$. At the exit of the second passage, a second wake zone characteristic of the maximum value of the turbulent kinetic energy appears and extends along the first part of the pipe connecting the solar air heater with the box prototype. After the decrease of the turbulent kinetic energy in the second part of the pipe, an expulsion area appears in the hole inlet of the box prototype and invaded in the discharge area

until the reverse wall. This fact can be explained by the recirculation zone appeared in the whole area of the box prototype. Indeed, a slightly decrease of the turbulent kinetic energy has been observed outside this area. However, in the outlet of the box prototype, a wake zone characteristic of the maximum value of the turbulent kinetic energy has been appeared. By comparing the turbulent kinetic energy for the different instances, it is clear that the maximum value of the turbulent kinetic energy is obtained at t=12 hours and it is equal to k=1.157 $m^2.s^{-2}$. For the other instances, the turbulent kinetic energy decreases and the minimum values are obtained at t=16 hours. At this instance, the maximum value of the turbulent kinetic energy is equal to k=1.111 $m^2.s^{-2}$.

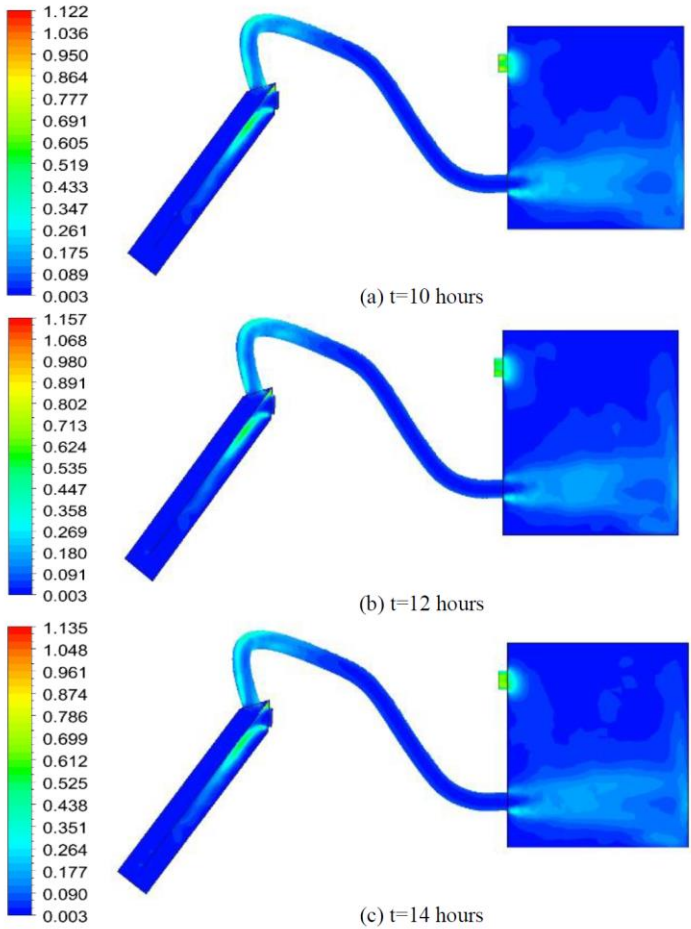

Figure 18. (Continued onto next page).

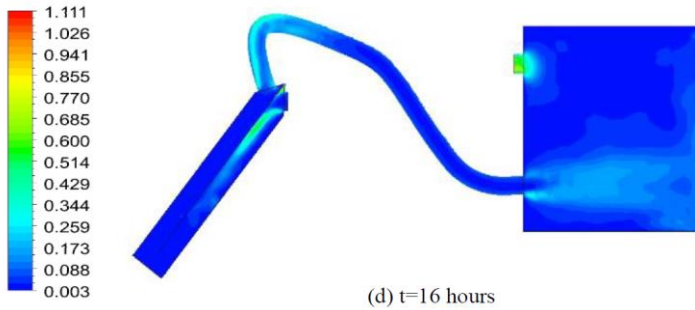

Figure 18. Distribution of the turbulent kinetic energy in the longitudinal plane.

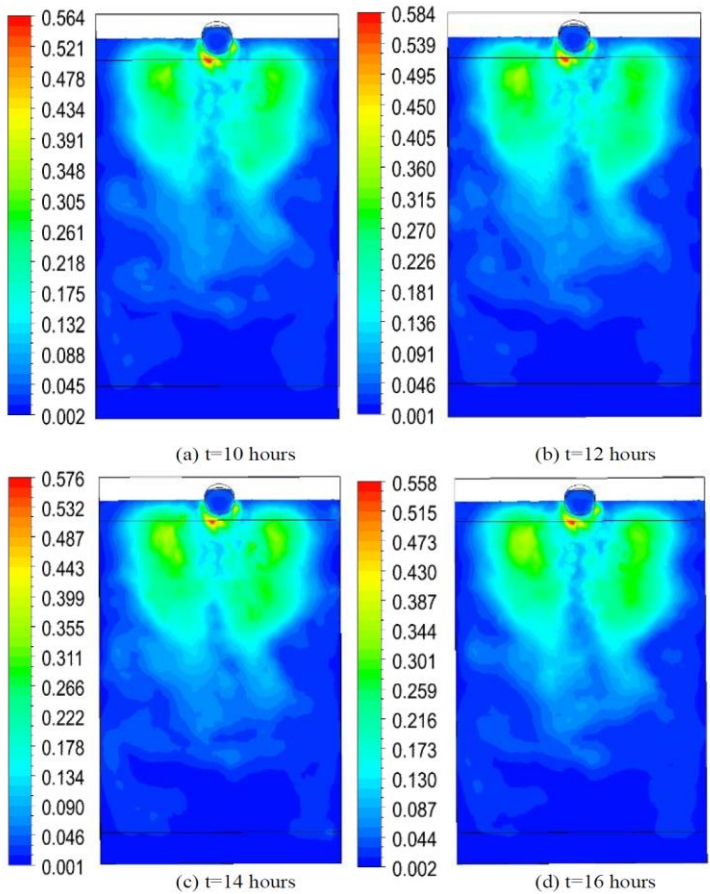

Figure 19. Distribution of the turbulent kinetic energy in the first passage.

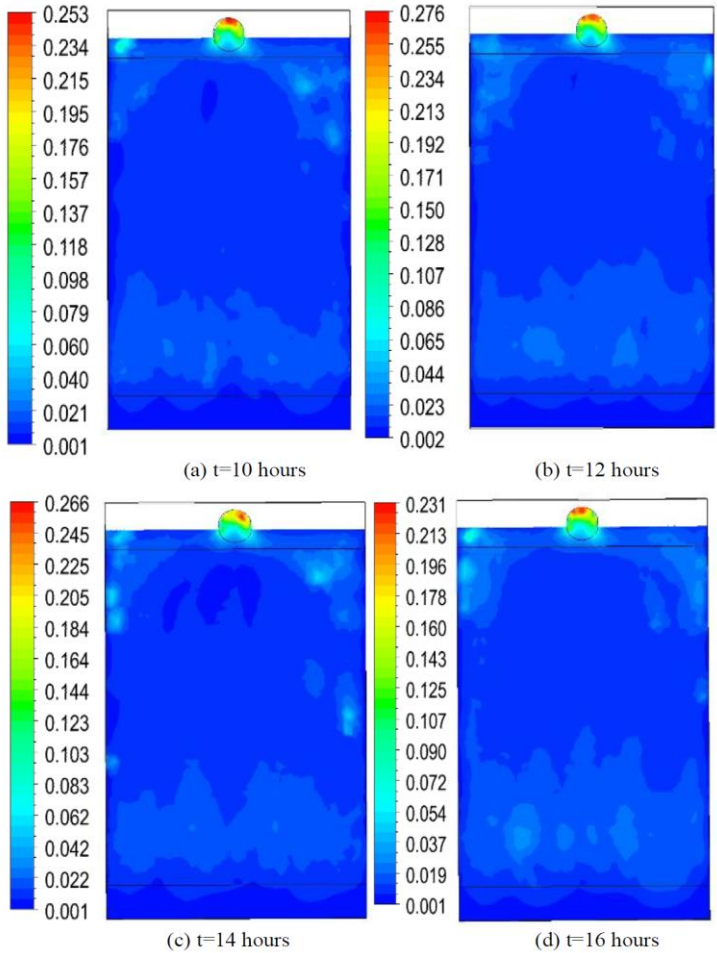

Figure 20. Distribution of the turbulent kinetic energy in the second passage.

4.6. Turbulent Eddy Frequency

Figures 21, 22 and 23 show the distribution of the turbulent eddy frequency in the different longitudinal and transverse planes for the first and second passages of the solar air heater supplying the box prototype at t=10 hours, t=12 hours, t=14 hours and t=16 hours. According to these results, it is clear that the turbulent eddy frequency presents the same distribution at the different considered instances. For example, at t=12 hours, a wake zone characteristic

of the maximum value of the turbulent eddy frequency has been created from the collector inlet of the solar air heater, with a moderate value of the turbulent eddy frequency equal to ω=300 s^{-1}. This wake is expanded in the first passage near the absorber side and until the mid-plane. In these conditions, the maximum value of the turbulente eddy frequency is equal to ω=500 s^{-1}. Away from this area, the turbulent eddy frequency decreases and reaches a low value equal to ω=40 s^{-1} at the bottom of the collector where the insulator is localized. Through the second passage and away from the glass and the absorber, the turbulent eddy frequency continues the decreases even more and reaches a null value in the upper half plane. In the pipe connecting the solar air heater with the box prototype, the turbulent eddy frequency increases and reaches a maximum value equal to ω=500 s^{-1}. By comparing the turbulent eddy frequency for the different instances, it is clear that we found the same results. In all these cases, the maximum value of the frequency is equal to ω=308 s^{-1}.

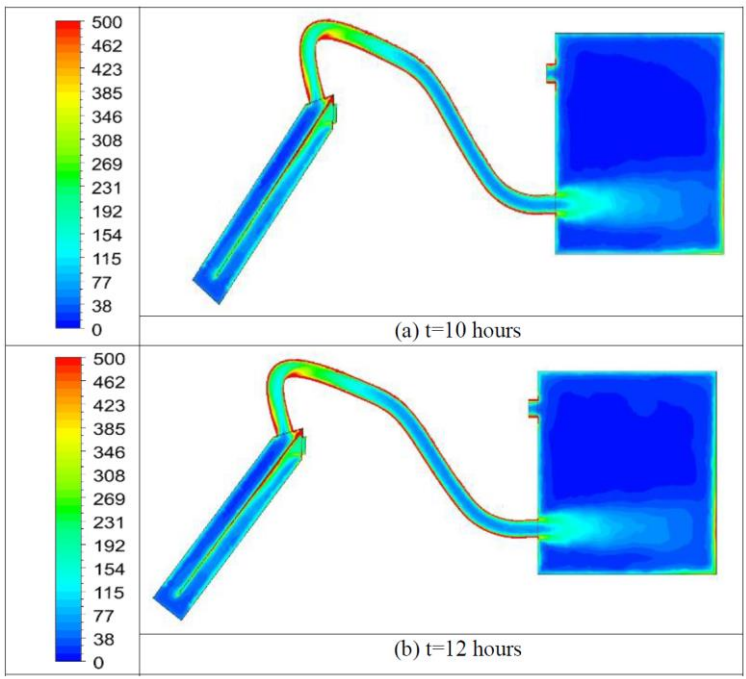

Figure 21. (Continued onto next page).

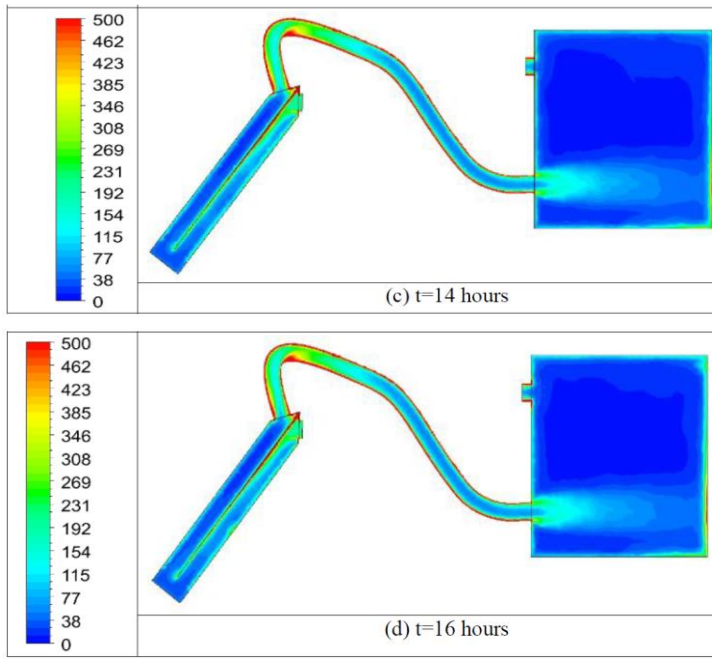

Figure 21. Distribution of the Turbulence Eddy Frequency in the longitudinal plane.

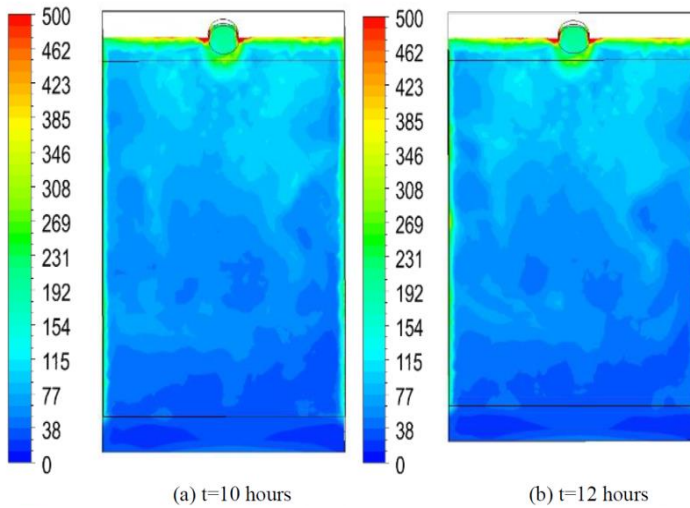

Figure 22. (Continued onto next page).

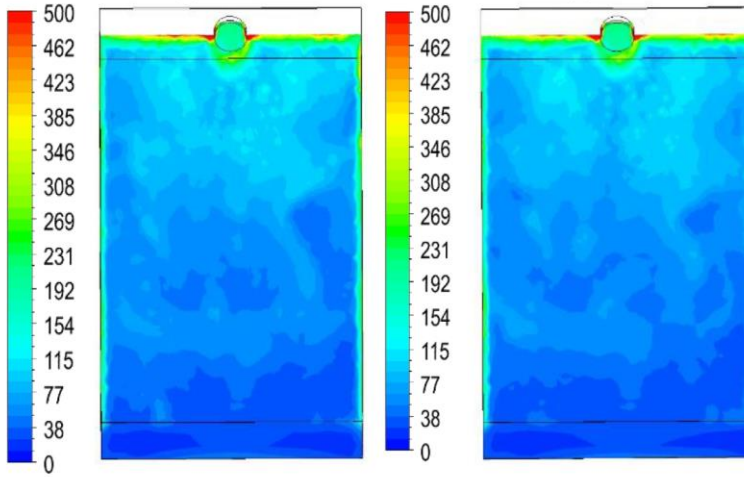

Figure 22. Distribution of the turbulent eddy frequency in the first passage.

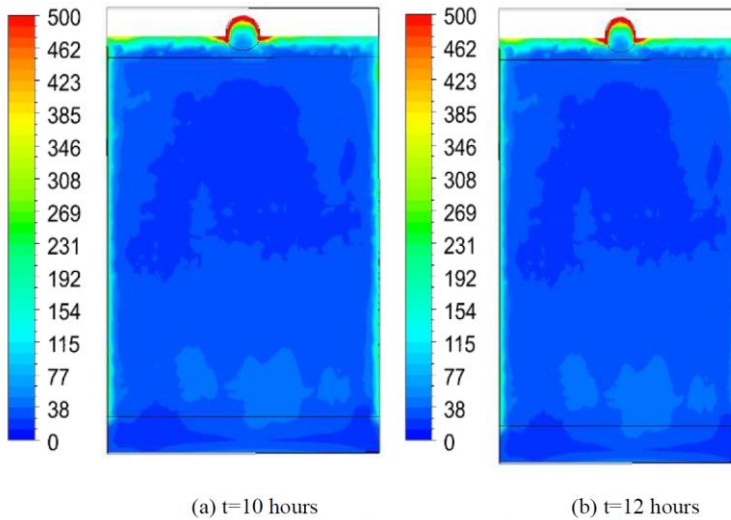

Figure 23. (Continued onto next page).

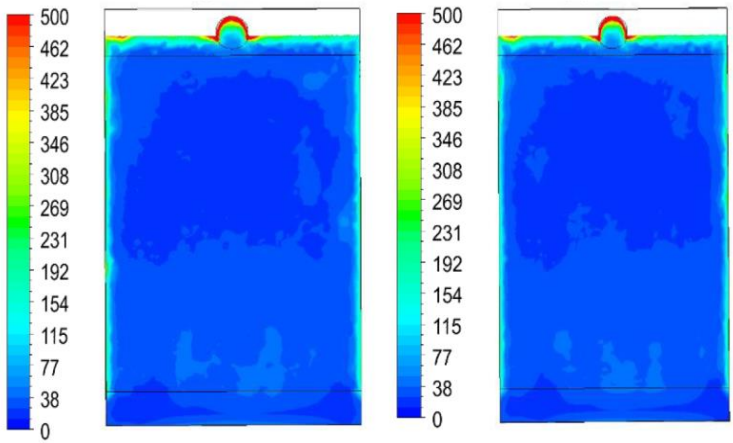

Figure 23. Distribution of the turbulent eddy frequency in the second passage.

4.7. Turbulent Viscosity

Figures 24, 25 and 26 show the distribution of the turbulent viscosity in the different longitudinal and transverse planes for the first and second passages of the solar air heater supplying the box prototype at t=10 hours, t=12 hours, t=14 hours and t=16 hours. According to these results, it is clear that the turbulent viscosity presents the same distribution at the different considered instances. For example, at t=12 hours, a wake zone characteristic of the maximum value of the turbulent viscosity has been observed around the collector inlet of the solar air heater. This wake is expanded in the first passage near the absorber side. In these conditions, the maximum value of the turbulent viscosity is equal to μ_t=0.002 kg.m^{-1}.s^{-1}. Away from this area, the turbulent viscosity presents a very weak value. The same fact has been observed in the second passage, where the maximum value is equal to μ_t=0.001 kg.m^{-1}.s^{-1} in the first mid-plane. In the absorber, the turbulent viscosity reaches a null value. At the exit of the second passage, a slight increase of the turbulent viscosity until μ_t=0.002 kg.m^{-1}.s^{-1} has been observed in the first part of the pipe connecting the solar air heater with the box prototype. In the remainder of the pipe, the turbulent viscosity decreases and presents very low values. In the hole inlet of the box prototype, the low values of the turbulent viscosity continue to appear in the first part of the discharge area. In the second part, a slight increase of the turbulent viscosity has been observed on the side of the

reverse wall. In the rest of the domain of the box prototype, a wake zone characteristic of the maximum value of the turbulent viscosity, equal to μ_t=0.007 kg.m^{-1}.s^{-1}, has been created. This fact can be explained by the recirculation zone appeared in the whole area of the box prototype. Indeed, a rapid expansion of the turbulent viscosity until μ_t=0.012 kg.m^{-1}.s^{-1} has been observed in the hole outlet of the box prototype. By comparing the turbulent viscosity for the different instances, it is clear that the maximum value of the turbulent viscosity is obtained at t=12 hours and it is equal to μ_t=0.0131 kg.m^{-1}.s^{-1}. For the other instances, the turbulent viscosity decreases and the minimum values are obtained at t=16 hours. At this instance, the maximum value of the turbulent viscosity is equal to μ_t=0.012 kg.m^{-1}.s^{-1}.

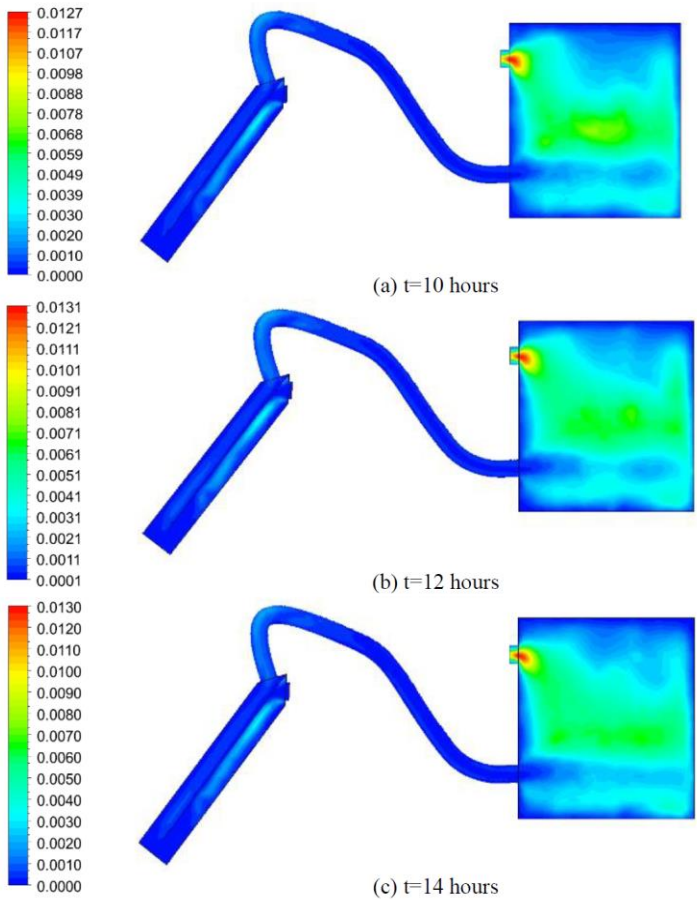

Figure 24. (Continued onto next page).

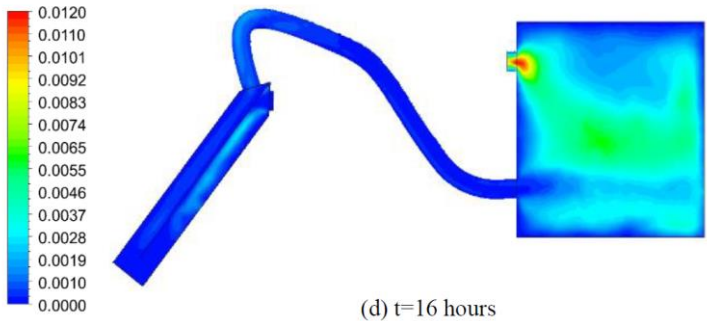

Figure 24. Distribution of the turbulent viscosity in the longitudinal plane.

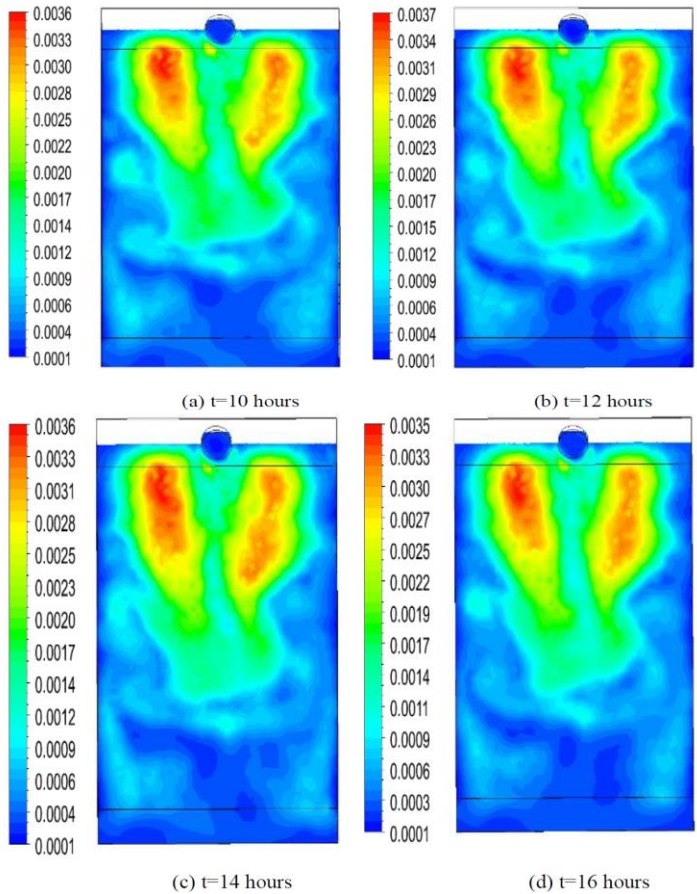

Figure 25. Distribution of the turbulent viscosity in the second passage.

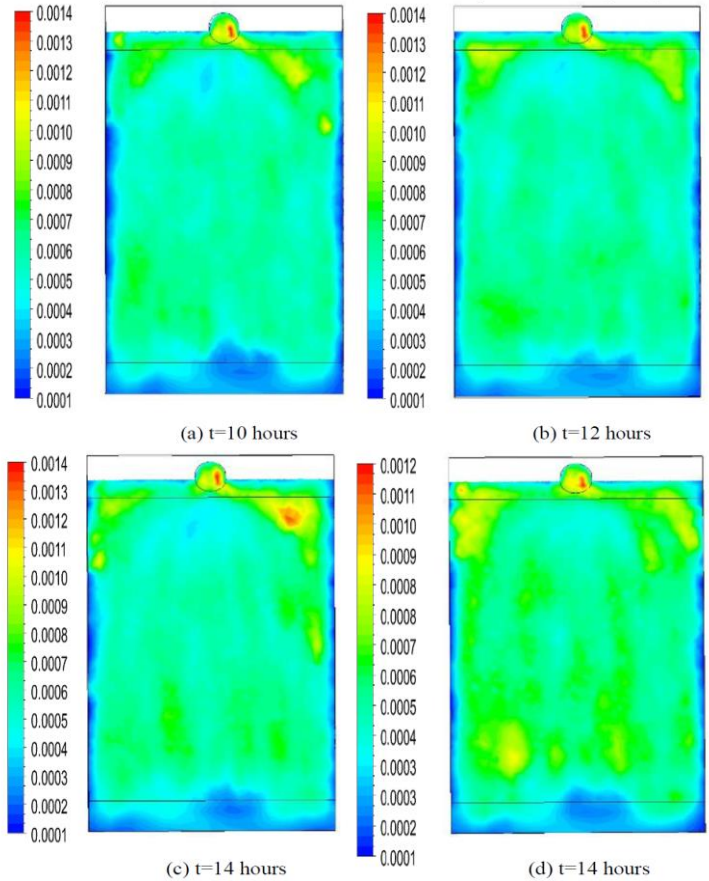

Figure 26. Distribution of the turbulent viscosity in the second passage.

5. Comparison with Experimental Results

Figures 27 and 28 compare the numerical results of the temperature and velocity profiles in the second channel superposed with our experimental results in a fan delivery mode side the insulation. Different instances equal to t=8 hours, t=10 hours, t=12 hours, t=14 hours, t=16 hours and t=18 hours have been considered. According to these results, a similar appearance between the curves has been observed for the magnitude velocity with a small difference between the calculated values. However, this difference is more clear for the temperature profiles. In fact, in these conditions, the maximum values of the

temperature are obtained at t=12 hours. By comparing these obtained results, it has been observed that the temperature values decrease slightly at t=14 hours. However, the minimum values of the temperature is obtained at t=18 hours. For the others instances t=10 hours, t=16 hours and t=8 hours, the temperature values decrease immensely. The comparison of the numerical results with our experimental data picked up on 28 August 2017 at t=12 hours, presents a good agreement with a gap equal to 6%. These results confirm the validity of our numerical method.

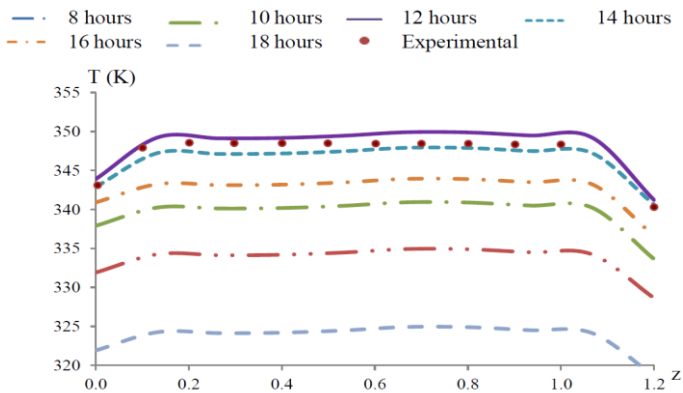

Figure 27. Profiles of the temperature in the second channel.

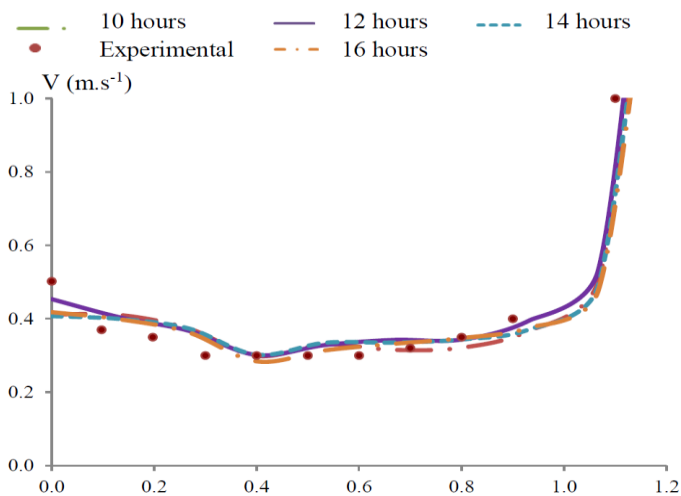

Figure 28. Profile of the magnitude velocity in the second channel.

6. Energy Efficiency

Figure 29 presents the profile of the energy efficiency which confirms the results obtained over the time. In fact, at the beginning of the day, the energy efficiency has very low values. With the increase of the temperature through the day, there is a gradual increase of the energy efficiency until t=12 hours, with a value equal to η= 31.8%. In the first half day, it has been noted that the increase of the energy efficiency is more important after t=10 hours. Afternoon, the energy efficiency starts to decrease with a constant slope. At t=18 hours, the energy efficiency is very low and it is equal to η= 24.8%.

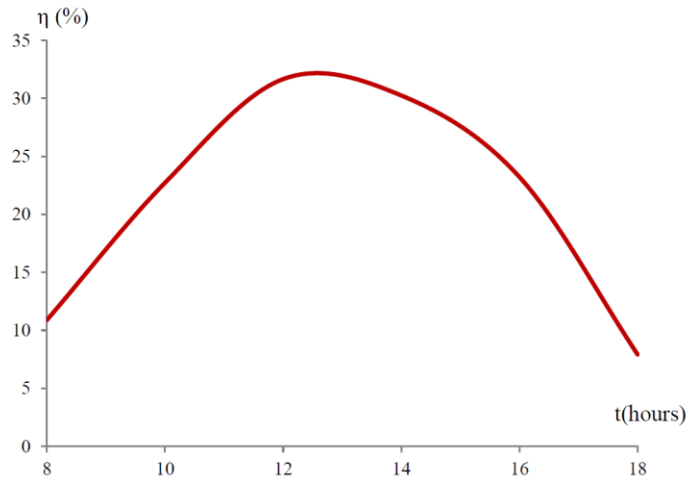

Figure 29. Energy efficiency profile.

Conclusion

Since the solar air heater is not very commonly used in the domestic and industrial applications, we are interested on the design and the realization of a new solar air heater test bench to investigate the efficiency of the solar system. The considered test bench consists of two passages solar air heater separated by an absorber and powered by a fan working in a delivery mode and placed in the inlet, side the insulation. On the glass side, it is connected to the box prototype through a pipe. On this system, a glass is hanging on the front side and an absorber is inserted inside. The hot air flow is routed towards the box

prototype. Two circular holes, are located in the same face of the box prototype. The inlet hole allows the hot air supply. However, the outlet hole allows its escape into the ambient environment. Indeed, we have developed numerical simulations to study the turbulent flow in the considered test bench over the day. In these conditions, it has been observed a decrease in the flow and an appearance of the recalculation zones in the first passage. This phenomenon is more prominent during the transition of the flow to the second passage. However, the flow becomes uniform until the exit of the solar air heater. Via the pipe separating the solar air heater from the box prototype, a discharge area appears in the hole inlet and invaded the reverse wall. By comparing the local characteristics for the different instances, a similar appearance has been observed with a maximum value at t=12 hours. For the magnitude velocity, a small difference between the calculated values has been noted. However, this difference is more clear for the temperature distribution and the turbulent characteristics. For the energy efficiency, it presents very low values at the beginning of the day. With the increase of the temperature through the day, there is a gradual increase of the energy efficiency until t=12 hours, with a value equal to η= 31,8%. This technology will be very useful since it can provide sustainable energy and substitute the expensive traditional technologies.

References

[1] Bakri, B., H. Benguesmia, A. Ketata, S. Driss, Z. Driss, Prediction of the unsteady turbulent flow in a solar air heater test bench, *Modelling, Measurement and Control B*, Vol. 89(1-4), 2020, 7-13.

[2] Ayadi, A., Z. Driss, A. Bouabidi, H. Nasraoui, M. Bsisa, M. S. Abid, A computational and an experimental study on the effect of the chimney height on the thermal characteristics of a solar chimney power plant, *Journal of Process Mechanical Engineering*, 231 (2017) 1-14.

[3] Driss, S., Z. Driss, I. Kammoun, Numerical simulation and wind tunnel experiments on wind-induced natural ventilation in isolated building with patio, *Energy*, 90 (2015) 917-925.

[4] Benguesmia, H., B. Bakri, Z. Driss, Effect of the turbulence model on the heat ventilation analysis in a box prototype, *Diagnostyka*, 21(3) (2020), 55-66.

[5] Bakri, B., S. Driss, A. Ketata, Z. Driss, H. Benguesmia, F. Hamrit, Study of the Heat Ventilation in a Box Prototype With the k-ω Turbulence Model, *Transylvanian Review Journal*, Vol XXXVI (30) (2018)7989-8000.

[6] Bakri, B., O. Eleuch, A. Ketata, S. Driss, Z. Driss, H. Benguesmia, Study of the turbulent flow in a newly solar air heater test bench with natural and forced convection modes, *Energy*, 161(2018)1028-1041.

[7] Bakri, B., A. Ketata, S. Driss, H. Benguesmia, Z. Driss, F. Hamrit, Unsteady investigation of the heat ventilation in a box prototype, *International Journal of Thermal Sciences*, 135 (2019)285–297.

[8] Bakri, B., S. Driss, A. Ketata, H. Benguesmia, F. Hamrit, Z. Driss, Study of the meshing effect on the turbulent flow in a building system with a k-ω turbulence model. *International Conference on Mechanics and Energy (ICME'2016)*, December 22-24 2016, Hammamet, Tunisia.

[9] Bakri, B., A. Ketata, S. Driss, H. Benguesmia, F. Hamrit, Z. Driss, Effect of the turbulence model on the aerodynamic structure to evaluate the thermal comfort in a building system, *International Conference on Mechanics and Energy (ICME'2016)*, December 22-24 2016, Hammamet, Tunisia.

[10] Bakri, B., A. Ketata, S. Driss, Z. Driss, H. Benguesmia, F. Hamrit, Unsteady simulation of the aerodynamic structure in a heated box prototype, *International Conference on Mechanics and Energy (ICME'2017)*, December 18-20 2017, Sousse, Tunisia.

[11] Bakri, B., S. Driss, A. Ketata, Z. Driss, H. Benguesmia, F. Hamrit, Study of the turbulent flow in a box prototype with the k-ω turbulence model, *Congrès Algérien de Mécanique, (CAM2017-289)*, 26-30 Novembre, Constantine-Algérie.

[12] Bakri, B., H. Benguesmia, A. Ketata, S. Driss, Z. Driss, F. Hamrit, Study of the Natural Convection Flow in a Solar Air Heater Test Bench, *International Conference on Mechanics and Energy (ICME'2018)*, December 20-22 2018, Hammamet, Tunisia.

[13] Bakri, B., H. Benguesmia, A. Ketata, H. Nasraoui, Z. Driss, Performance evaluation of the natural-convection of a solar air-heater with a plate absorber, *International Conference on Mechanics and Energy (ICME'2018)*, December 19-21 2019, Monastir, Tunisia.

[14] Bakri, B., H. Benguesmia, Study of the forced convective heat transfer in a solar air heater, *The First International Conference on Materials, Energy and Environment (MEE'2020, N°: EO05)*, January 20-21, 2020, El Oued University, Algeria.

[15] Bakri, B., H. Benguesmia, A. Ketata, S. Driss, Z. Driss, A comparative study of the turbulence models on the heat ventilation in a box prototype, *1ère Conférence National sur: la Transition Énergétique en Algérie Conférence (CNTEA1-2020)*, Mars 8-9, 2020, M'sila, Algeria.

[16] Bakri, B., H. Benguesmia, A. Ketata, S. Driss, Z. Driss, Choice of the appropriate turbulence model for modeling the air flow inside a room, *1ère Conférence National sur: la Transition Énergétique en Algérie Conférence (CNTEA1-2020)*, Mars 8-9, 2020, M'sila, Algeria.

[17] Bakri, B., H. Benguesmia, A. Ketata, S. Driss, Z. Driss, CFD based performance analysis of a solar air heater test bench with unsteady turbulent flow, 9ème *Journées des sciences de l'ingénieur JSI'2020,* September 25-27, 2020, Sfax, Tunisia.

[18] Driss, Z., O. Mlayeh, D. Driss, M. Maaloul, M.S. Abid, Numerical simulation and experimental validation of the turbulent flow around a small incurved Savonius wind rotor. *Energy*, 74 (2014) 506-517.

[19] Driss, Z., G. Bouzgarrou, W. Chtourou, H. Kchaou, M.S. Abid. Computational studies of the pitched blade turbines design effect on the stirred tank flow characteristics. *European Journal of Mechanics B/Fluids*, 29, 2010, 236-245.

[20] Driss, Z., O. Mlayah, S. Driss, M. Maaloul, M.S. Abid, Study of the incidence angle effect on the aerodynamic structure characteristics of an incurved Savonius wind rotor placed in a wind tunnel, *Energy*, 113 (2016) 894-908.

[21] Driss, Z., O. Mlayah, S. Driss, D. Driss, M. Maaloul, M.S. Abid, Study of the bucket design effect on the turbulent flow around unconventional Savonius wind rotors, *Energy*, 89 (2015) 708-729.

[22] Yang, M., X. Yang, X. Li, Z.Wang, P. Wang, Design and optimization of a solar air heater with offset strip fin absorber plate, *Applied Energy*, 113 (2014) 1349-1362.

[23] Altaa, D., E. Bilgilib, C.Ertekina, O. Yaldiza, Experimental investigation of three different solar air heaters: Energy and exergy analyses, *Applied Energy*, Volume 87 (2010) 2953-2973.

[24] Zukowski, M., Experimental investigations of thermal and flow characteristics of a novel microjetair solar heater, *Applied Energy*, 142 (2015) 10-20.

[25] El-Sebaii, A. A., S. Aboul-Enein, M. R. I. Ramadan, S. M. Shalaby, B. M. Moharram, Thermal performance investigation of double pass-finned plate solar airheater, *Applied Energy*, 88 (2011) 1727–1739.

[26] Wazed, M. A., Y. Nukman, M. T. Islam, Design fabrication of a cost effective solar air heater for Bangladesh, *Applied Energy*, 87 (2010) 3030–3036.

[27] Esen, H., Experimental energy and exergy analysis of a double-flow solar airheater having different obstacles on absorber plates, *Building and Environment*, 43 (2008) 1046-1054.

Chapter 2

Air Pollution in Primary Educational Environments in a European Context

K. Slezakova[1,2], B. Kotlík[3] and M. C. Pereira[1,2]

[1]LEPABE- Faculty of Engineering, University of Porto, Porto Portugal
[2]ALiCE- Faculty of Engineering, University of Porto, Porto Portugal
[3]National Institute of Public Health, Prague, Czech Republic

Abstract

As the modern population grows, most residents live in cities with inadequate ambient air quality. While daily exposure to outdoor air pollution is inevitable, people spend most of their time indoors. Thus, indoor air quality (IAQ) has significant impacts on human health, possibly leading to greater risks than outdoor pollution, which is especially relevant for susceptible populations. Children spend a large part of their daily time in education settings (such as nurseries, kindergartens, preschools, primary and elementary schools). The respective indoor air quality is a significant parameter for their health. However, despite the relevance of these specific environments, the current knowledge concerning the respective levels of pollution and child exposures is far from comprehensive. The present chapter introduces the topic of indoor air pollution in child populations. It outlines the relevance of child education settings, emphasizing large-scale studies conducted in primary schools within the European context.

Keywords: air pollution, indoors, schools, susceptible populations, traffic emissions particulate matter (PM), gaseous pollutants

In: Indoor Air Quality
Editor: Robert M. Ridgway
ISBN: 979-8-88697-134-7

1. Introduction

The learning process is a crucial parameter in forming children's personalities and how they deal with various situations of their lives. Schools represent the environment in which children spend most of the day. Studies have shown that depending on the national habits, children spend up to 930 h in schools each year (Palacios Tempertano et al., 2020); time at school can constitute up to 30% of the lifetime (Korsavi et al., 2021). Considering the substantial amount of time, environmental conditions in these settings may profoundly impact the respective occupants.

A growing body of evidence has shown associations between indoor air quality and adverse effects on cardiorespiratory health, psychological wellbeing, and cognitive performance (Dong et al., 2019; Palacios Temprano et al., 2020; Savelieva et al., 2020; Wang et al., 2021). Children represent a particularly susceptible group to health effects related to poor indoor air quality (IAQ). They breathe a greater air volume relative to their body weight than adults (Gilliland et al., 2017). As they often breathe through mouths, they may avoid the natural defenses of the nasal passages. In addition, as school attendance is compulsory, it is necessary to provide an environment suitable for all children, including those that may be even more susceptible to poor IAQ (due to allergies or other kinds of hypersensitivity). Therefore, this chapter summarizes the largest and the most relevant studies of IAQ in schools conducted in the European context during the last decade.

2. Importance of Education

In nowadays society, education is a necessity for humans. Over the last decades, education has transformed from a process of gathering knowledge to being a tool to a well-adjusted overall development. It encourages critical thinking while helping kids to develop future life goals. It facilitates the formation of a healthy thought process and grooms cognitive abilities. Education teaches social skills and helps to build confidence, encourages critical thinking while helping to develop future life goals.

In general, education includes four aspects that are essential for a child's healthy development: (i) mental, (ii) social, (iii) physical, and (iv) overall development (Young, 2011). In terms of the mental aspect, the school environment represents a source of knowledge to which children are exposed,

which allows them to acquire information across various subjects (literature, history, mathematics, politics, etc.). Secondly, schools are the first opportunity for a child to be socializing. Until then, extended family members and parents represent the child's only social interactions. At schools, children build new interactions, which introduce them to social skills such as empathy, friendship, and participation relevant to their growth. Furthermore, schools are an essential environment for physical development, where, unlike at home, children can direct their energy into more sociable forms. In addition, sports activities and different crafts can help children shift their focus towards productive learning processes. Finally, the schools are the relevant environment for a child's overall development. In the current educational scenarios, children learn beyond the traditional way of learning. They are taught to develop their mind, curiosity, and the importance of imagination. Play is supported (Milteer et al., 2012), and an encompassing educational curriculum allows for suitable cognitive system development.

3. Structural Organization of Education

Despite several similarities between European societies, there are several types of schools. The parameters that reflect the main differences between them are education curriculum and the form of assessment, financing, personnel management, governance, and accountability. In terms of age levels, the first phase of education is represented by early childhood (pre-primary) education (ECE), which is based on the principle of a child's universal right to develop and learn.

Early childhood education comprises the following educational groups/organizations: nurseries, daycare centers, kindergartens, and preschools. The exact definitions may differ between each country, and the specifics are always given by each country's educational system (Couchenour and Chrisman, 2016). However, in general, nurseries typically provide an education for kids six weeks old until they start primary school. They generally open for longer hours (often between 7 a.m. and 7 p.m.) to accommodate parents' work hours and are frequently operational during the summer holidays. Nurseries also include in the daily program various social activities, which is not often feasible at preschools. Preschools typically provide education for children between 3-5 years. They provide educational exercises and assessments to prepare children for primary school education. They are required to follow the national curriculum and usually have similar

time schedules as schools (i.e., long summer and half-term holidays, etc.). In most European education systems, compulsory education typically begins at six years at primary schools (level 1 of the International Standardization Classification of Education, ISCED) (European Commission, 2016). However, the attendance of the last year of pre-primary education, usually at the age of 5, is often already compulsory (European Commission, 2016). In several European (though non-English speaking) countries, the term "kindergarten" then refers to this first stage of formal education (ISCED level 0). It is necessary to emphasize that in the United States, the terminology used somewhat differs. The term "kindergarten" typically refers to an institution for 5 to 6 years old children. In contrast, pre-kindergarten is for children 4-5 years old (per national efforts to increase the availability of pre-primary education). Daycare centers are then typically education institutions in the US context for children up to 2 ½ years old (Dustmann et al., 2008).

Primary schools represent the first level of compulsory education in Europe and most parts of the world. The term "primary" is preferred in the United Kingdom and several Commonwealth countries (STANDS4 LLC, 2022). In most European education systems, the duration of full-time compulsory education is 9-10 years and ends at the age of 15-16 years. The primary level is typically followed by the secondary education level and corresponds to full-time school attendance (European Commission, 2016). It shall be pointed out that in North America, primary schools usually refer to only the first three years of elementary education (i.e., grades 1-3), and the term "elementary school" is used more frequently in this geographical context.

One of the most relevant aspects that influence school governance is its financing. Based on the source of the economic resources, the schools can be considered either as "public" or "private." The government financially supports public schools, and there are accessible to anyone. These schools then follow regulations set forth by the government (via different authorities of the respective country). Students in public schools are assessed (either annually or twice to three times per year, depending on each country's system). Their performance is evaluated, typically using some scoring system (Couchenour and Chrisman, 2016).

Private (or independent) schools are not administrated or financially supported by the government. The school's funding is requested through a tuition fee for a student (entirely or partially with the help of a scholarship). Private schools are administered by an independently voted executive board, ensuring the school's autonomous operation. However, private schools must be accredited and may be financially supported by different organizations.

Finally, the term “boarding schools” implies providing accommodation and food for students apart from education. Once again, these can be fully private or supported by a state, thus offering a free education but charging additional fees for accommodation and food.

4. Relevance of Indoor Air Exposure

The quality of the indoor environment and its impacts on health have gained much scientific interest as the relevant studies have shown that indoor air is a significant health concern (Morawska et al., 2017; Salonen et al., 2018, 2019; Salthammer et al., 2016). In developed societies, indoor exposure represents 90% of our lifetime.

The quality of indoor air is influenced by many parameters, which include not only the surroundings of the environment (building structure and its design, material, etc.) but also the activities of respective occupants and the presence of indoor emission sources (Slezakova et al., 2019; Madureira et al., 2020b). A large portion of indoor pollution, without a doubt, originates from outdoors air (Health Effects Institute, 2018; Slezakova et al., 2013; Madureira et al., 2020a), either via openings that can be somewhat limited (such as doors, windows, air exhausts), but also via those uncontrolled (cracks and leaks). This is especially relevant as WHO’s recent report once again showed that 99% of the nowadays population lives in urban areas where ambient air quality is insufficient (WHO, 2021).

Children are particularly vulnerable to the detrimental health impacts of poor air quality. As they spend a significant proportion of their time at schools, initiatives to mitigate their exposure to air pollution in these spaces are of utmost importance (Jantunen et al., 2011). Over the last decade, there have been various studies focusing problematic of child exposure in schools. Meíja et al., (2011) extensively summarized methodologies to assess child exposure. Other authors in detail addressed the use biomonitoring assays for child exposure (to PM and polycyclic aromatic hydrocarbons - i.e., PAHs) in school environments (Oliveira et al., 2019).

In addition, across the EU region, there have several initiatives which, on a large scale, addressed the lack of information concerning air pollution and its levels in schools (Table 1).

Table 1. Summary of the relevant studies on IAQ in schools in Europe during the last decade

Acronym	Period	Region	Data set	Study design	Relevant references
SINPHONIE	2010-2012	25 EU countries	114 primary schools	Walkthrough checklist; IAQ: comfort parameters; chemical pollutants; biological agents; Concurrent indoor/outdoor air monitoring; Health questionnaires (8-10 yr. old)	Annesi-Maesano et al., 2013; Csobod et al., 2014; EC, 2014; Baloch et al., 2020
BREATHE	2011-2016	Spain – Barcelona	39 primary schools	Environment characterization; IAQ: traffic-related pollutants – NO_2, particulate matter: $PM_{<0.25}$, $PM_{0.25-2.5}$, $PM_{2.5-10}$, ultrafine particles, elemental carbons, organic compounds (VOCs, PAHs); Concurrent monitoring in classrooms and schools' yards; Population (7-10 yr.), n = 2897	Amato et al., 2014; Reche et al., 2014; Rivas et al., 2014; Viana et al., 2015; Sunyer et al., 2015; Forns et al., 2016; Alemany et al., 2018; Rivas et al., 2018; van Drooge et al., 2020;
InArQ	2016-2019	5 Central EU countries	64 primary schools	Building inspections; IAQ: comfort parameters; chemical pollutants; Concurrent indoor/outdoor air assessment; Time activity diary; National vulnerability assessment via questionnaires (6-14 yr. old)	InAirQ, 2020; Szabados et al., 2021

4.1. SINFONIE Study (Schools Indoor Pollution and Health – Observatory Network)

Up to this date, SINFONIE (Csobod et al., 2014) was one of the most significant projects concerned with IAQ in schools in Europe. It was conducted between 20010-2012, 114 schools participated in the study. They were divided into four groups based on geographical and climatic conditions.

Group 1 (North) included Finland, Sweden, Estonia, and Lithuania. Group 2 (West) consisted of France, the UK, Belgium, Germany, and Austria. Group 3 (Central Eastern Europe) encompassed the Czech Republic, Poland, Slovakia, Hungary, Bulgaria, Romania, Serbia, Bosna, and Herzegovina. The last Group 4 was designated for South and composed of the following countries: Italy, Portugal, Malta, Greece, Cyprus, and Albania. The study design encompassed six steps: (1) background study, (2-3) assessment of the indoor and outdoor environments and the related health effects; (4) creation of the database; (5) health risk assessment; and (6) recommendation and guidelines.

One of the highlights of this study was the harmonized and standardized methodology that was used across all schools, which allowed suitable comparisons between the various geographical groups (Baloch et al., 2020). In the first step, walkthrough checklists were developed and used to characterize the school buildings and selected classrooms sufficiently. Building checklist described outdoor conditions and covered parameters such as descriptions of schools' surroundings, construction materials, ventilation, or occurrence of past problems, etc. In contrast, classroom surveys focused on the report and characterization of indoor environments to support sufficient descriptors to support the overall analysis.

The indoor and outdoor monitoring was very comprehensive, and the selected classrooms were assessed considering a wide range of parameters, as summarized in Table 2.

Table 2. Physical and comfort parameters, chemical pollutants, and microbiological agents assessed in SINFONIE schools

Physical and comfort parameters	Chemical pollutants	Biological agents
Relative humidity (RH)	Particulates (PM_{10}, $PM_{2.5}$)	Fungal and bacteria DNA
Air temperature (T)	Ozone (O_3)	Endotoxins
Carbon dioxide (CO_2)	Nitrogen oxides (NO_X)	Allergens
Ventilation rate	Carbon monoxide (CO)	
	Formaldehyde	
	Benzene	
	Trichloroethylene	
	Tetrachlorethylene	
	Naphthalene	
	d-limone, α-pinene	
	Radon	

The air sampling in the selected schools (EC, 2014) was done during five weekdays (Monday till Friday) during the occupied hours (8:00-16:00). The methodology encompassed passive samplings for organic chemicals (formaldehyde, pinene, limonene, benzene, trichloroethylene, tetrarchloroethylene), nitrogen oxides (NO_X) and ozone (O_3), combined with consequent analytical procedures (spectrophotometry, gas or liquid chromatography, ion chromatography). Optical light scattering samplers were used for PM_{10} and $PM_{2.5}$; the latter being also collected gravimetrically over a filter. Carbon monoxide and dioxide were measured continuously by low-cost monitors. Benzo(α)pyrene and naphthalene were collected in the gas phase on a sorbent tube and then analyzed by gas chromatography-mass spectrometry. Concentrations of radon were measured by a passive method (track counts on exposed film). Association with various health effects (eye, skin, upper-, lower respiratory, and systemic disorder symptoms) were collected through standardized questionnaires (Baloch et al., 2020; EC, 2014).

In terms of indoor air pollution, the results of this study demonstrated that suitable IAQ in schools is highly dependent on its geographical position, with outdoor air being the major source of emissions indoors (EC, 2014). Within the SINPHONIE project, 67% of the selected schools were located in the vicinity of trafficked streets and hot spots (Csobod et al., 2014) with high concentrations (above WHO recommended guidelines) for $PM_{2.5}$, formaldehyde, benzene, and radon (Baloch et al., 2020). Poor IAQ in schools cannot be fully addressed without considering outdoor emissions. Thus, ambient air quality in urban environments must be fully ensured and suitably controlled on a national level. Further, consideration has to be given to indoor environment design strategies (use of clean and sustainable materials and technologies) as insufficient indoor conditions were identified in 20% of the schools (occupancy densities of less than 2 m^2/child; EC, 2014).

4.2. BREATHE Study (BRain dEvelopment and Air polluTion ultrafine particles in scHool childrEn)

The BREATHE was conducted on the national level only during 2011–2015 in 39 Spanish (Barcelona) primary schools. In addition to Spanish schools not being included in the SINFONIE, the results obtained in BREATHE were highly relevant. The main aim of this study was to address child exposure to traffic-related air pollutants (TRAPs) in schools and their association with neurodevelopment. The respective population included 2897 subjects (7-10

years old), and the assessed health outcomes included working memory development, executive attention, impulsivity, and selective attention. The child's responsible reported the behavior problems (Questionnaire on Strengths and Difficulties), whereas teachers reported the child's attention deficit and hyperactivity disorder.

Like SINFONIE, IAQ sampling employed one week per school approach, conducted simultaneously inside the classroom and in the courtyard. In order to address the impacts of traffic emissions, the selected pollutants included NO_2 and different fractions of PM, namely (Amato et al., 2014; Rivas et al., 2014): quasi-ultrafine (<0.25 μm; $PM_{<0.25}$), accumulation (0.25 to 2.5 μm; $PM_{0.25-2.5}$), and coarse mode (2.5 to 10 μm; $PM_{2.5-10}$). In addition, the study also included ultrafine particle numbers (i.e., aerodynamic diameters smaller than 100 nm; UFP) as well as organic compounds (VOCs and PAHs) (Reche et al., 2014; Viana et al., 2015). The results of this study clearly indicated the much-needed interventions (Rivas et al., 2018). The authors demonstrated a strong impact of ambient emissions indoors, as outdoor emissions contributed 53% of indoor PM. Specifically, traffic emissions resulted in 1-10 $\mu g/m^3$ indoors being significantly higher for classrooms oriented directly to the streets, rather than to those with windows oriented for interior building and playgrounds (Amato et al., 2014). Ultrafine particles (UFP) and elemental carbon highly penetrated indoors (indoor/outdoor ratio 94% and 70%, respectively) (Reche et al., 2014; Viana et al., 2015). The rest of indoor $PM_{2.5}$ (47%) originated from indoor sources, either from continuous resuspension of soil particles (13%) or a mixed source (34%) comprising organic (skin flakes, clothes fibers, possible condensation of VOCs) and Ca-rich particles (from chalk and building deterioration). Concerning the health impacts of traffic emissions, children attending schools with higher exposure to NO_2, UFP, and elemental carbon experienced substantially smaller growth in cognitive development for the selected parameters (n-back and the attentional network tests – working memory, superior working memory, and inattentiveness; Rivas et al., 2018; Sunyer et al., 2015). Similarly, traffic emissions' pollutants show associations with behavioral problems (Forns et al., 2015).

4.3. InAirQ Study (Transnational Adaptation Actions for Integrated Indoor Air Quality Management)

The InAirQ project (InAirQ, 2020) was the most recent European study (2016-2019). It aimed to assess the health risk of indoor air pollutants on a vulnerable

population (6-14 yrs.) and take the respective action for improvement. This study included 64 primary schools across five Central European countries, namely Hungary, Poland, Czech Republic, Slovenia, and Italy. In terms of organization, the first step of the study included the building and classroom characterizations. Air pollution assessment was then conducted concurrently indoors and outdoors in 12 schools of each country. Similarly, with the previous studies, sampling protocol followed the strategy of "one week in each school" (during winter 2017-2018). Microbiological agents were not considered. The measured parameters included: (i) comfort indicators (T, RH, CO_2), and (ii) chemical pollutants – VOCs (benzene, toluene, xylene ethylbenzene, trichloroethylene, tetrachloroethylene, α-pinene, limonene, 2-ethyl hexanol, naphthalene), aldehydes (formaldehyde, acetaldehyde, propionaldehyde, benzaldehyde, hexanal), CO, NOx, ozone, particulate matter (PM_{10} and $PM_{2.5}$), and radon. In addition, the monitoring approach was not standardized among all partners. While passive monitoring (on absorbent pods) was used in the classrooms during lessons, continuous real-time monitoring was conducted only in selected countries (InAirQ, 2020). Despite some regional similarities between these countries, the obtained ranges of pollutants (VOCs, aldehydes, $PM_{2.5}$, carbon dioxide, radon) and comfort parameters varied significantly (Szabados et al., 2021). Indoor air pollution was categorized in the form of "Indoor Health Index" (calculated as threshold values determined by the health effects of the air pollutants/physical parameters) with the severity of scale in the following order: dangerous > very unhealthy > unhealthy > moderate > healthy. It shall be emphasized that 58% of the schools presented possible health risks in terms of insufficient IAQ, whereas 42% of schools exhibited poor comfort. The most alarming situation was in Italy, where indoor air pollution of 42% of schools was "dangerous" and 50% either "very unhealthy" or "unhealthy." The schools in the study were located in Turino, one of the most polluted European areas due to traffic emissions (Rizza et al., 2020; EEA, 2019). The poor indoor conditions were caused by extremely high concentrations of benzene (4.9-20.1 $\mu g/m^3$) due to the local trafficked roads (with high volume and speed of vehicles). In addition, comfort levels for the respective students were also inadequate, with insufficient levels of RH (20-35%). Hungary was the second-worst country where IAQ possessed some health risks in almost all schools (31% "very unhealthy," 63% "unhealthy"), in the majority of cases due to high $PM_{2.5}$ (51-79 $\mu g/m^3$; and 29-50 $\mu g/m^3$, respectively). In addition, 62% of all assessed schools were poorly ventilated with increased CO_2 and RH (InAirQ, 2020). Finally, in the Czech Republic, 38% of the schools were either "very

unhealthy" or "unhealthy" (due to high indoor $PM_{2.5}$ from ambient air emissions); similar to Italy, comfort conditions were unhealthy due to extremely low RH (26-35%).

Conclusion

In the present competitive world, education is a necessity for humans. Our society fully depends on adequate education accessible to everyone. Education also has a crucial role in society's economic and political growth, among other social developments. In that view, schools represent a significant role for our future population; they play a vital role that defines essential parts of each country.

Schools represent an environment where children spend long hours every day. The available studies have demonstrated that IAQ in schools is still far from acceptable in the European context. In addition, environmental conditions in schools have vast implications on the physical health and emotional wellbeing of children. The COVID-19 pandemic has brought about the most extensive disruption to formal education in recent history and has resulted in school closures and temporarily moved to online teaching and learning across the globe. Additionally, the respective pandemic vividly illustrated deficiencies of buildings with respect to traditional technical solutions for achieving good indoor air prominently demonstrated in school buildings. As daily life returns to face-to-face activities and learning, we face new challenges requiring suitable air supply and proper ventilation of indoor spaces. The existing ventilation strategies, though, typically depend on natural ventilation or mixing mechanical ventilation, and they are not fully capable of dealing with both long-range and short-range pollutants. While some solutions are actionable, it is necessary to develop pandemic-related science-based and practice-oriented guidelines on the safe operation of indoor spaces, emphasizing susceptible subjects.

Funding

This work was financially supported by: LA/P/0045/2020 (ALiCE) and UIDB/00511/2020 - UIDP/00511/2020 (LEPABE) funded by national funds through FCT/MCTES (PIDDAC). Additional funding was provided by

PTDC/CTA-AMB/3040/2021 from Fundação para a Ciência e a Tecnologia (FCT) through national funds.

References

Alemany, S., Vilor-Tejedor, N., García-Esteban, R., Bustamante, M., Dadvand, P., Esnaola, M., Mortamais, M., Forns, J., van Drooge, B. L., Álvarez-Pedrerol, M., Grimalt, J. O., Rivas, I., Querol, X., Pujol, J. and Sunyer, J. (2018). Traffic-related air pollution, APOE ∈4 status, and neurodevelopmental outcomes among school children enrolled in the BREATHE project (Catalonia, Spain). *Environmental Health Perspectives* 126(8), 087001.

Amato, F., Rivas, I., Viana, M., Moreno, T., Bouso, L., Reche, C., Àlvarez-Pedrerol, M., Alastuey, A., Sunyer, J. and Querol, X. (2014). Sources of indoor and outdoor PM2.5 concentrations in primary schools. *Science of The Total Environment* 490, 757-765.

Annesi-Maesano, I., Baiz, N., Banerjee, S., Rudnai, P., Rive, S. and SINPHONIE Group. (2013). Indoor air quality and sources in schools and related health effects. *Journal of Toxicology and Environmental Health, Part B Critical Reviews* 16(8):491-550.

Baloch, R. M., Maesano, C. N., Christoffersen, J., Banerjee, S., Gabriel, M., Csobod, É., de Oliveira Fernandes, E., Annesi-Maesano, I. and SINPHONIE Study group. (2020). Indoor air pollution, physical and comfort parameters related to schoolchildren's health: Data from the European SINPHONIE study. *Science of the Total Environment* 15 (739:139870).

Couchenour, D. and Chrisman, D. K. (2016). The SAGE encyclopedia of contemporary early childhood education. *Thousand Oaks*, California, USA: Sage Publication, Inc.

Csobod, E., Annesi-Maesano, I., Carrer, P., Kephalopoulos, S., Madureira, J., Rudnai, P., De Oliveira Fernandes, E., Barrero, J., Beregszászi, T., Hyvärinen, A., Moshammer, H., Norback, D., Páldy, A., Pándics, T., Sestini, P., Stranger, M., Taubel, M., Varró, M., Vaskovi, E., Ventura Silva, G. and Viegi, G. (2014). SINPHONIE (Schools Indoor Pollution and Health Observatory Network in Europe): *Executive Summary of the Final Report*. Luxembourg: Publications Office of the European Union.

Definitions.net, STANDS4 LLC. (2022). *Primary School*. Accessed January 2, 2022. https://www.definitions.net/definition/primary+school.

Dong, W., Liu, S., Chu, M., Zhao, B., Yang, D., Chen, C., Miller, M. R., Loh, M., Xu, J., Chi, R., Yang, X., Guo, X. and Deng, F. (2019) Different cardiorespiratory effects of indoor air pollution intervention with ionization air purifier: Findings from a randomized, double-blind crossover study among school children in Beijing. *Environmental Pollution* 254, 113054.

Dustmann, C., Fitzenberger, B. and Machin, S. (2008). *The Economics of Education and Training*. Heidelberg, Germany: Physica-Verlag.

European Commission (EC), Joint Research Centre, Directorate-General for Health and Consumers, Institute for Health and Consumer Protection, Varró, M., Hyvärinen, A., Rudnai, P., et al., (2014). SINPHONIE: Schools Indoor Pollution & Health

Observatory Network in Europe: final report, *Luxembourg: Publications Office of the European Union*.

European Commission/EACEA/Eurydice. (2016). Compulsory education in Europe – 2016/17: Eurydice facts and figures. *Luxembourg: Publications Office of the European Union*.

European Environmental Agency (EEA). (2019). Air quality in Europe – 2019 report; EEA report 10/2019. *Luxembourg: Publications Office of the European Union*, 2019.

Forns, J., Dadvand, P., Foraster, M., Alvarez-Pedrerol, M., Rivas, I., López-Vicente, M., Suades-Gonzalez, E., Garcia-Esteban, R., Esnaola, M., Cirach, M., Grellier, J., Basagaña, X., Querol, X., Guxens, M., Nieuwenhuijsen, M. J. and Sunyer, J. (2016). Traffic-related air pollution, noise at school, and behavioral problems in Barcelona schoolchildren: A cross-sectional study. *Environmental Health Perspective* 124(4), 529-535.

Gilliland, F., Avol, E., McConnell, R., Berhane, K., Gauderman, W. J., Lurmann, F. W., Urman, R., Chang, R., Rappaport, E. B. and Howland S. (2017). The effects of policy-driven air quality improvements on children's respiratory health. *Research Report* 190. Boston, MA: Health Effects Institute.

Health Effects Institute. (2018). State of global air 2018. *Special Report.* Boston, MA: Health Effects Institute.

InAirQ. (2020). *The Summary Report. Interreg Central Europe Programme. European Union, European Regional Development Fund.* Available at https://www.interreg-central.eu/Content.Node/InAirQ/CE69-INAIRQ-Summary-report.pdf, lastly accessed in January 2022.

Jantunen, M., De Oliveira Fernandes, E., Carrer, P. and Kephalopoulos, S. (2011). Promoting actions for healthy indoor air (IAIAQ). *Luxembourg: European Commission Directorate-General for Health & Consumers*.

Korsavi, S. S., Montazami, A. and Mumovic, D. (2021). Perceived indoor air quality in naturally ventilated primary schools in the UK: Impact of environmental variables and thermal sensation. *Indoor Air* 31, 480-501.

Madureira, J., Slezakova, K., Costa, C., Pereira, M. C. and Teixeira, J. P. (2020a). Assessment of indoor air exposure among newborns and their mothers: Levels and sources of PM10, PM2.5 and ultrafine particles at 65 home environments. *Environmental Pollution* 264, 114746.

Madureira, J., Slezakova, K., Silva, A. I., Lage, B., Mendes, A., Aguiar, L., Pereira, M. C., Teixeira, J. P. and Costa, C. (2020b). Assessment of indoor air exposure at residential homes: Inhalation dose and lung deposition of PM10, PM2.5 and ultrafine particles among newborn children and their mothers. *Science of the Total Environment* 717, 137293.

Mejía, J. F., Choy, S. L., Mengersen, K. and Morawska, L. (2011). Methodology for assessing exposure and impacts of air pollutants in school children: Data collection, analysis and health effects - A literature review. *Atmospheric Environment* 45 (4), 813-823.

Milteer, R. M., Ginsburg, K. R., Mulligan, D. A., Ameenuddin, N., Brown A., Christakis, D. A., Cross, C., Falik, H. L., Hill, D. L., Hogan, M. J., Levine, A. E. and O'Keeffe, G. S. (2012). The importance of play in promoting healthy child development and

maintaining strong parent-child bond: Focus on children in poverty. *Pediatrics* 129 (1), 204-213.

Morawska, L., Ayoko, G. A., Bae, G. N., Buonanno, G., Chao, C. Y. H., Clifford, S., Fu, S. C., Hänninen, O., He, C., Isaxon, C., Mazaheri, M., Salthammer, T., Waring, M. S. and Wierzbicka, A. (2017). Airborne particles in indoor environment of homes, schools, offices and aged care facilities: The main routes of exposure. *Environment International* 108, 75-83.

Oliveira, M., Slezakova, K., Delerue-Matos, C., Pereira, M. C. and Morais, S. (2019). Children environmental exposure to particulate matter and polycyclic aromatic hydrocarbons and biomonitoring in school environments: A review on indoor and outdoor exposure levels, major sources and health impacts. *Environment International*, 124, 180-204.

Palacios Temprano, J., Eichholtz, P., Willeboordse, M. and Kok, N. (2020). Indoor environmental quality and learning outcomes: protocol on large-scale sensor deployment in schools. *BMJ Open* 10, e031233.

Reche, C., Viana, M., Rivas, I., Bouso, L., Àlvarez-Pedrerol, M., Alastuey, A., Sunyer, J., and Querol, X. (2014). Outdoor and indoor UFP in primary schools across Barcelona, *Science of The Total Environment* 493, 943-953.

Rivas, I., Querol, X., Wright, J. and Sunyer, J. (2018). How to protect school children from the neurodevelopmental harms of air pollution by interventions in the school environment in the urban context. *Environment International* 121, 199-206.

Rivas, I., Viana, M., Moreno, T., Pandolfi, M., Amato, F., Reche, C., Bouso, L., Àlvarez-Pedrerol, M., Alastuey, A., Sunyer, J. and Querol, X. (2014). Child exposure to indoor and outdoor air pollutants in schools in Barcelona, Spain. *Environment International* 69, 200-212.

Rizza, V., Torre, M., Tratzi, P., Fazzini, P., Tomassetti, L., Cozza, V., Naso, F., Marcozzi, D. and Petracchini, F. (2021). Effects of deployment of electric vehicles on air quality in the urban area of Turin (Italy). *Journal of Environmental Management* 297, 113416.

Salonen, H., Salthammer, T. and Morawska, L. (2018). Human exposure to ozone in school and office indoor environments. *Environment International* 119, 503-514.

Salonen, H., Salthammer, T. and Morawska, L. (2019). Human exposure to NO2 in school and office indoor environments. *Environment International*, 130, art. no. 104887.

Salthammer, T., Uhde, E., Schripp, T., Schieweck, A., Morawska, L., Mazaheri, M., Clifford, S., He, C., Buonanno, G., Querol, X., Viana, M. and Kumar, P. (2016). Children's wellbeing at schools: Impact of climatic conditions and air pollution. *Environment International* 94, 196-210.

Savelieva, K., Elovainio, M., Lampi, J., Ung-Lanki, S. and Pekkanen, J. (2020). Psychosocial factors 700 and indoor environmental quality in respiratory symptom reports of pupils: a cross-sectional study 701 in Finnish schools. *BMJ Open 10*, e036873.

Slezakova, K., de Oliveira Fernandes, E. and Pereira, M. C. (2019). Assessment of ultrafine particles in primary schools: Emphasis on different indoor microenvironments. *Environmental Pollution* 246, 885-895.

Slezakova, K., Pires, J. C. M., Castro, D., Alvim-Ferraz, M. C. M., Delerue-Matos, C., Morais, S. and Pereira, M. C. (2013). PAH air pollution at a Portuguese urban area:

Carcinogenic risks and sources identification. *Environmental Science and Pollution Research* 20 (6), 3932-3945.

Sunyer, J., Esnaola, M., Alvarez-Pedrerol, M., Forns, J., Rivas, I., López-Vicente, M., Suades-González, E., Foraster, M., Garcia-Esteban, R., Basagaña, X., Viana, M., Cirach, M., Moreno, T., Alastuey, A., Sebastian-Galles, N., Nieuwenhuijsen, M. and Querol, X. (2015). Association between traffic-related air pollution in schools and cognitive development in primary school children: A Prospective Cohort Study. *PLOS Medicine* 12(3): e1001792.

Szabados, M., Csákó, Z., Kotlík, B., Kazmarová, H., Kozajda, A., Jutraz, A., Kukec, A., Otorepec, P., Dongiovanni, A., Di Maggio, A., Fraire, S. and Szigeti. T. (2021). Indoor air quality and the associated health risk in primary school buildings in Central Europe - The InAirQ study. *Indoor Air* 31(4), 989-1003.

van Drooge, B. L., Rivas, I., Querol, X., Sunyer, J. and Grimalt, J. O. (2020). Organic air quality markers of indoor and outdoor PM2.5 aerosols in primary schools from Barcelona. *International Journal of Environmental Research and Public Health* 17(10), 3685.

Viana, M., Rivas, I., Querol, X., Alastuey, A., Álvarez-Pedrerol, M., Bouso, L, Sioutas, C., and Sunyer J. (2015). Partitioning of trace elements and metals between quasi-ultrafine, accumulation and coarse aerosols in indoor and outdoor air in schools. *Atmospheric Environment* 106, 392-401.

Wang, C., Zhang, F., Wang, J., Doyle, J. K., Hancock, P. A., Mak, C. M. and Liu, S. (2021). How indoor environmental quality affects occupants' cognitive functions: A systematic review. *Building and Environment* 193, 107647.

World Health Organization (WHO). (2021). WHO global air quality guidelines: particulate matter (PM2.5 and PM10), ozone, nitrogen dioxide, sulfur dioxide and carbon monoxide. *World Health Organization*.

Young, M. (2011). What are schools for? *Educação, Sociedade & Culturas* 32, 145-155.

Chapter 3

Computational Study and Experimental Validation of Heat Ventilation in a Box Prototype

Bdis Bakri[1], Slah Driss[2], Ahmed Ketata[2], Hani Benguesmia[3] and Zied Driss[2,*]

[1]Mechanical Engineering Department,
Faculty of Technology, University of M'sila, Algeria
[2]Laboratory of Electro-Mechanic Systems (LASEM),
National School of Engineers of Sfax (ENIS),
University of Sfax (US), Sfax, Tunisia
[3]LGE Laboratory,
Electrical Engineering Department,
Faculty of Technology,
University of M'sila, Algeria

Abstract

In this chapter, the impact of the numerical parameters on the heat ventilation was studied in a box prototype. Particularly, a computational study and an experimental validation have been developed to compare the standard k-ω turbulence model, the BSL k-ω turbulence model, the SST k-ω turbulence model, the standard k-ε turbulence model, the RNG k-ε turbulence model and the Realizable k-ε turbulence model. From the obtained results, it is noticed that the aerodynamic characteristics present the same emergence nevertheless the maximum values depend on the turbulence model. Particularly, it has been noted that the value founded with the standard k-ω turbulence model is nearest to the experimental

* Corresponding Author's Email: zied.driss@enis.tn.

In: Indoor Air Quality
Editor: Robert M. Ridgway
ISBN: 979-8-88697-134-7

results. This study tends to show that the standard k-ω turbulence model is the most efficient to study the air flow in the box prototype. For this model, the meshing effect on the CFD results was studied to choose the adequate mesh with a minimum calculated time. The numerical results were compared using experimental results developed in our laboratory. The good agreements confirm the numerical method.

Nomenclature

A_0	Model constant
A_s	Model constant
C_1	Model constant
$C_{1\varepsilon}$	Constant of the k-ε turbulence model (dimensionless)
$C_{2\varepsilon}$	Constant of the k-ε turbulence model (dimensionless)
C_μ	Constant of the k-ε turbulence model (dimensionless)
E	Total energy (J)
F_i	Force components on the i direction (N)
G_k	Generation of the turbulent kinetic energy ($kg.m^{-1}.s^{-3}$)
G_b	Generation of turbulence kinetic energy ($kg.m^{-1}.s^{-3}$)
G_v	Production of turbulent viscosity ($kg.m.s^{-2}$)
G_ω	Generation of the dissipation rate of the turbulent kinetic energy ($kg.m^{-1}.s^{-3}$)
H	Height (m)
h	Thermal enthalpy ($J.kg^{-1}$)
k	Turbulent kinetic energy ($m^2.s^{-2}$)
l	Length (m)
p	Pressure (Pa)
P_r	Prandt number
Q_H	Heat source or sink per unit volume ($kg.m^{-1}.s^{-3}$)
q_i	Diffusive heat flux (J)
Re	Reynolds number (dimensionless)
R_k	Constant of the k-ω turbulence model (dimensionless)
R_ω	Constant of the k-ω turbulence model (dimensionless)
S	Scalar measure of the deformation tensor
S_i	Mass-distributed ($kg.m^{-2}.s^{-2}$)
S_{ij}	Mean rate-of-strain tensor (s^{-1})
S_ω	Source terms of the specific dissipation rate of the turbulent kinetic energy ($kg.m^{-1}.s^{-3}$)

S_k	Source terms of the turbulent kinetic energy ($kg.m^{-1}.s^{-3}$)
S_ε	Source terms of the dissipation rate of the turbulent kinetic energy ($kg.m^{-1}.s^{-3}$)
T	Temperature (K)
t	Time (s)
u	Velocity components ($m.s^{-1}$)
u_i'	Fluctuating velocity components ($m.s^{-1}$)
V	Magnitude velocity ($m.s^{-1}$)
x_i	Cartesian coordinate (m)
x	Cartesian coordinate (m)
y	Cartesian coordinate (m)
Y_M	Fluctuating dilatation in compressible turbulence ($kg.m^{-1}.s^{-3}$)
Y_k	Turbulence dissipation of k
Y_ω	Turbulence dissipation of ω
z	Cartesian coordinate (m)
U	Free-stream velocity (m/s)
η_0	Constant of the k-ε turbulence model (dimensionless)
α_0	Constant of the k-ω turbulence model (dimensionless)
α_∞	Constant of the k-ω turbulence model (dimensionless)
α^*_∞	Constant of the k-ω turbulence model (dimensionless)
δ_{ij}	Kronecker delta function (dimensionless)
β	Constant of the k-ε turbulence model (dimensionless)
ε	Dissipation rate of the turbulent kinetic energy ($m^2.s^{-3}$)
μ	Dynamic viscosity (Pa.s)
μ_t	Turbulent viscosity (Pa.s)
μ_{eff}	Effective viscosity (Pa.s)
ω	Specific dissipation rate (s^{-1})
ρ	Density ($kg.m^{-3}$)
β_i	Constant of the k-ω turbulence model (dimensionless)
σ_k	Constant of the k-ε turbulence model (dimensionless)
σ_ε	Constant of the k-ε turbulence model (dimensionless)
σ_k	Turbulent Prandtl number for k (dimensionless)
σ_ω	Turbulent Prandtl number for ω (dimensionless)
τ_{ij}	Viscous shear stress tensor (Pa)
$(\tau_{ij})_{eff}$	Deviatoric stress tensor (Pa)
Φ	Equivalence ratio (dimensionless)
Γ_k	Effective diffusivity of k

Γ_ω	Effective diffusivity of ω
Ω	Swirl number (dimensionless)
Ω_{ij}	Rate of rotation tensor (s^{-1})

Keywords: heat ventilation, box prototype, turbulence model effect, experimental validation, CFD

1. Introduction

Heat ventilation by solar energy is used for wide range applications, such as hospitals, residential and commercial buildings. One of the chief benefits the solar ventilation is the reduction of the energy consumption by using renewable sources [1-7]. The mechanism of Heat ventilation has been investigated by many researchers. In particular, Driss et al. [1] investigated thermal comfort evaluation and the heat ventilation in a living room. In other applications, Teodosiu et al. [8] presented experimental-numerical comparisons to give the precision of a CFD model. Du et al. [9] conducted experimental measurements to present the characteristics of a Chinese house. Homod et al. [10] studied and proposed a new system by coupling reasons of internal conditions that are influenced by the outdoor environment. Terrados and Moreno [11] integrated the architectural concepts with energy efficient. Yasa [12] analysed the inside regions and the surrounding areas of education buildings and performed the microclimatic comfort. Premrov et al. [13] studied a single storey house wood frame case for objective to avoid the last energy. Johnston [14] predicted and measured performance of the building fabric in new build dwellings. Chan et al. [15] modeled a building of 21 floors by using Energy plus. The results of simulations indicate that the apartments flat presents satisfactory periods for the environment. Ibrahim et al. [16] planned technical coating projection. The proposed mathematical model was compared with experimental results. Nam and Chae [17] developed an optimal design of the grounding by using a numerical method. Alam et al. [18] improves a method of releasing heat from the building to reduce the energy demand of the building in a tropical environment. Rode [19] illustrated global relations to highlight the building performance. Han et al. [20] investigated hybrid solar energy system. A general view of the architectural envelope designs and innovative system was presented. Watson [21] reviewed design quality research on buildings in relation to users. Sailor et al. [22] describe the

system use implications that lead to building energy of green roof design decisions.

From these different anterior works, it has been noted that the design of buildings based on the reduction of the energy consumed. For thus, we have involved the study of the heat ventilation in a box prototype. Particularly, we have considered the turbulence models effect to choose the most effective model. The numerical results obtained in this work are validated via a box prototype realized in our LASEM laboratory.

2. Box Prototype System

Figure 1 depicts the physical domain of the considered box prototype. The box is characterized by a 0.22 m of height, 0.2 m of width and 0.3 m of length. Both square holes are localized at the same wall of the box. It has the same edge which is equal to 0.02 m, while it has different distance from the bottom wall of the box. The down hole is situated with a distance equal to h_1 = 0.05 m from the bottom wall, which is used to receive the air flow coming from the outside of the box prototype. However, the top hole is responsible on the evacuation of the air flow from the box to the surrounding air [1]. It is situated from the box base with a distance equal to h_2 = 0.18 m.

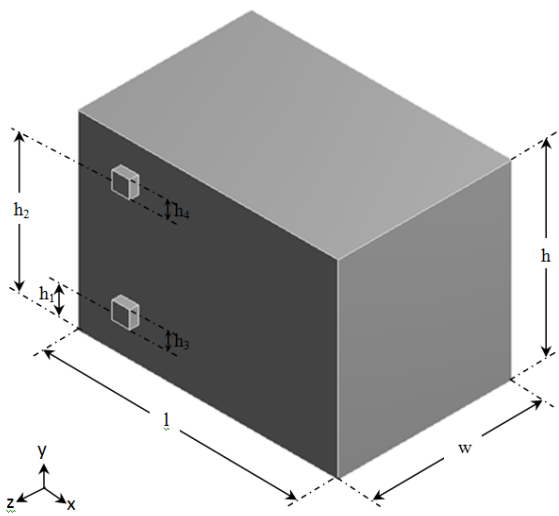

Figure 1. 3D view of the prototype.

3. Numerical Model

3.1. Boundary Conditions

The applied boundary conditions of the considered system are shown in Figure 2. The hot airflow enters to the box prototype through the down hole which is assumed as the inlet system. The velocity and the temperature at the inlet are respectively equal to V = 3.4 m.s-1 and T = 310 K. After the fluid recirculation inside the box, the airflow exits the system through a top hole with a pressure outlet value identical to the ambient static pressure. A no slip wall is applied for the outer walls of the domain.

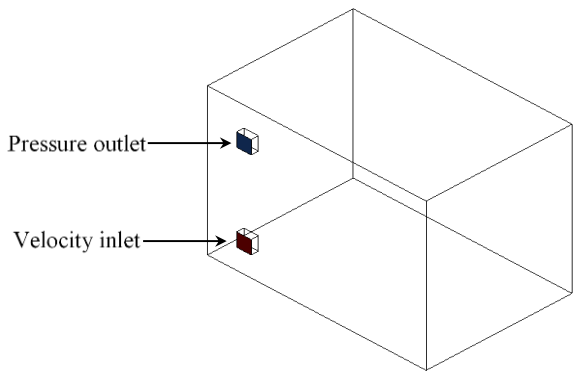

Figure 2. Boundary conditions.

3.2. Meshing

The meshing is an amportant step in the simulation procudure which affects directly the accuracy of the computantional findings. Then, a meshing analysis is required to minimize the error calculation. In the present study, the employed mesh density is taken from an anterior meshing analysis [23-32] which compares different meshing cases with our experimental data. The meshing choice is based on both accuracy and calculation time [33]. Figure 3 shows a view of the used optimal mesh with a tetrahedral volume cells. The 3D computantional domain is characterized by 167400 cells and 64312 nodes.

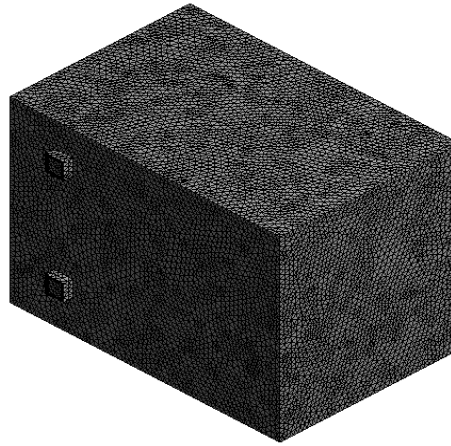

Figure 3. Meshing.

3.3. Mathematical Formulation

Table 1. Constants of the turbulence models

(a) Standard *k*-*ε* model

$C_{1\varepsilon}$	$C_{2\varepsilon}$	C_u	σ_k	σ_ε
1.44	1.92	0.09	1.0	1.3

(b) RNG *k*-*ε* model

C_1	$C_{2\varepsilon}$	β	..
1.44	1.92	0.012	4.38

(c) Realizable *k*-*ε* model

C_1	$C_{2\varepsilon}$	σ_k	σ_ε
1.44	1.9	1.0	1.2

(d) Standard *k*-*ω* model

α_0	α_∞	α^*_∞	R_ω	R_k	σ_k	σ_ω
1/9	1.9	1.0	2.95	6.0	2.0	2.0

Table 1. (Continued)

(e) BSL k-ω model

$\sigma_{k,1}$	$\sigma_{k,2}$	$\sigma_{\omega,1}$	$\sigma_{\omega,2}$	$\beta_{i,1}$	$\beta_{i,2}$
2.0	1.0	2.0	1.168	0.075	0.0828

(f) SST *k-ω* model

$\sigma_{k,1}$	$\sigma_{k,2}$	$\sigma_{\omega,1}$	$\sigma_{\omega,2}$	$\beta_{i,1}$	$\beta_{i,2}$	a_1
1.176	1.0	2.0	1.168	0.075	0.0828	0.31

The considered governing equations are the continuity equation, the momentum equations and the energy equation [34-26]. Taking a time average yields in the instantaneous equations, the Reynolds-averaged Navier-Stokes (RANS) equations can be written as follows:

$$\frac{\partial \rho}{\partial t} + \frac{\partial}{\partial x_i}(\rho u_i) = 0 \tag{1}$$

$$\frac{\partial}{\partial t}(\rho u_i) + \frac{\partial}{\partial x_j}(\rho u_i u_j) = -\frac{\partial p}{\partial x_j}\left[\mu\left(\frac{\partial u_i}{\partial x_j} + \frac{\partial j_i}{\partial x_i} - \frac{2}{3}\right)\right] + \frac{\partial}{\partial x_j}(-\rho\overline{u_i' u_j'})F_i \tag{2}$$

To close equation (2), these Reynolds stresses $-\rho\overline{u_i' u_j'}$ must be modeled by using the Boussinesq hypothesis, written as follows:

$$-\rho\overline{u_i' u_j'} = \mu_t\left(\frac{\partial u_i}{\partial x_j} + \frac{\partial u_j}{\partial x_i}\right) - \frac{2}{3}\left(\rho k + \mu_t \frac{\partial u_k}{\partial x_k}\right)\delta_{ij} \tag{3}$$

The energy equation is expressed as follows:

$$\frac{\partial}{\partial t}(\rho E) + \frac{\partial}{\partial x_i}\left[u_i(\rho E + p)\right] = \frac{\partial}{\partial x_j}\left[\left(k + \frac{c_p \mu_t}{Pr_t}\right)\frac{\partial T}{\partial x_j} + u_i(\tau_{ij})_{eff}\right] + S_h \tag{4}$$

where K is the thermal conductivity and E is the total energy. $\left(\tau_{ij}\right)_{eff}$ is the deviatoric stress tensor and is written as follows:

$$\left(\tau_{ij}\right)_{eff} = \mu_{eff}\left(\frac{\partial u_j}{\partial x_i} + \frac{\partial u_i}{\partial x_j}\right) - \frac{2}{3}\mu_{eff}\frac{\partial u_k}{\partial x_k}\delta_{ij} \tag{5}$$

The standard model k-ε is modeling by both transport equations of the turbulent kinetic energy k and its dissipation rate ε. These equations are obtained from the following expressions:

$$\frac{\partial}{\partial t}(\rho k) + \frac{\partial}{\partial x_j}(\rho k u_i) = \frac{\partial}{\partial x_j}\left[\left(\mu + \frac{\mu_t}{\sigma_k}\right)\frac{\partial k}{\partial x_j}\right] + G_k + G_b - \rho\varepsilon - Y_M + S_k \tag{6}$$

$$\frac{\partial}{\partial t}(\rho \varepsilon) + \frac{\partial}{\partial x_i}(\rho \varepsilon u_i) = \frac{\partial}{\partial x_j}\left[\left(\mu + \frac{\mu_t}{\sigma_\varepsilon}\right)\frac{\partial \varepsilon}{\partial x_j}\right] + C_{1\varepsilon}\frac{\varepsilon}{k}\left(G_k + C_{3\varepsilon}G_b\right) - C_{2\varepsilon}\frac{\varepsilon^2}{k} + S_\varepsilon \tag{7}$$

μ_t is the turbulent viscosity computed from the combination of k and ε:

$$\mu_t = \rho\, C_\mu \frac{k^2}{\varepsilon} \tag{8}$$

Table 1 (a) illustrates the different constants employed in the k-ε turbulence model.

The RNG k-ε model presents similarity with the standard k-ε turbulence model:

$$\frac{\partial}{\partial t}(\rho k) + \frac{\partial}{\partial x_i}(\rho k u_i) = \frac{\partial}{\partial x_j}\left(\alpha_k \mu_{eff}\frac{\partial k}{\partial x_j}\right) + G_k + G_b - \rho\varepsilon - Y_M + S_k \tag{9}$$

$$\frac{\partial}{\partial t}(\rho \varepsilon) + \frac{\partial}{\partial x_i}(\rho \varepsilon u_i) = \frac{\partial}{\partial x_j}\left(\alpha_\varepsilon \mu_{eff}\frac{\partial \varepsilon}{\partial x_j}\right) + C_{1\varepsilon}\frac{\varepsilon}{k}\left(G_k + C_{3\varepsilon}G_b\right) - C_{2\varepsilon}\rho\frac{\varepsilon^2}{k} - R_\varepsilon + S_\varepsilon \tag{10}$$

In these conditions, we have to write:

$$d\left(\frac{\rho^2 k}{\sqrt{\varepsilon\mu}}\right) = 1.72\,\frac{\hat{v}}{\sqrt{\hat{v}^3 - 1 + C_v}}\,d\hat{v} \tag{11}$$

$$\hat{v} = \frac{\mu_{eff}}{\mu} \tag{12}$$

The difference between the RNG and the standard k-ε turbulence models consists in the addition of this term:

$$R_\varepsilon = \frac{C_\mu \rho \eta^3 (1 - \eta/\eta_0)}{1 + \beta\eta^3}\,\frac{\varepsilon^3}{k} \tag{13}$$

where:

$$\eta = S\,\frac{k}{\varepsilon} \tag{14}$$

$$S = \sqrt{2 S_{ij} S_{ij}} \tag{15}$$

Table 1 (b) illustrates the different constants employed in the RNG k-ε turbulence model.

In the realizable k-ε turbulence model, the transport equation is giving as follows:

$$\frac{\partial}{\partial t}(\rho k) + \frac{\partial}{\partial x_j}(\rho k u_j) = \frac{\partial}{\partial x_j}\left[\left(\mu + \frac{\mu_t}{\sigma_k}\right)\frac{\partial k}{\partial x_j}\right] + G_k + G_b - \rho\varepsilon - Y_M + S_k \tag{16}$$

$$\frac{\partial}{\partial t}(\rho\varepsilon) + \frac{\partial}{\partial x_j}(\rho\varepsilon u_j) = \frac{\partial}{\partial x_j}\left[\left(\mu + \frac{\mu_t}{\sigma_\varepsilon}\right)\frac{\partial \varepsilon}{\partial x_j}\right] + \rho C_1 S\varepsilon - \rho C_2 \frac{\varepsilon^2}{k + \sqrt{\nu\varepsilon}} + C_{1\varepsilon}\frac{\varepsilon}{k} C_{3\varepsilon} G_b + S_\varepsilon \tag{17}$$

where:

$$C_1 = \max\left[0.43\frac{\eta}{\eta+5}\right] \tag{18}$$

As other k-ε turbulence models, the turbulent viscosity is calculated as follows:

$$\mu_t = \rho\, C_\mu \frac{k^2}{\varepsilon} \tag{19}$$

The difference between the realizable k-ε, the standard k-ε and the RNG k-ε turbulence models consists on the calculation of C_μ as:

$$C_\mu = \frac{1}{A_0 + A_s \frac{kU^*}{\varepsilon}} \tag{20}$$

Table 1 (c) illustrates the different constants employed in the realizable k-ε model.

In the k-ω standard turbulence model, the transport equations of the turbulent kinetic energy k and the specific dissipation rate ω are written as follows:

$$\frac{\partial}{\partial t}(\rho k) + \frac{\partial}{\partial x_i}(\rho k u_i) = \frac{\partial}{\partial x_j}\left(\Gamma_\omega \frac{\partial k}{\partial x_j}\right) + G_k + Y_k + S_k \tag{21}$$

$$\frac{\partial}{\partial t}(\rho \omega) + \frac{\partial}{\partial x_i}(\rho \omega u_i) = \frac{\partial}{\partial x_j}\left(\Gamma_\omega \frac{\partial k}{\partial x_j}\right) + G_\varpi + Y_\omega + S_\omega \tag{22}$$

Table 1 (d) illustrates the different constants employed in the k-ω turbulence model.

The BSL (Baseline) k-ω turbulence model presents a similar form:

$$\frac{\partial}{\partial t}(\rho k)+\frac{\partial}{\partial x_i}(\rho k u_i)=\frac{\partial}{\partial x_j}\left(\Gamma_k \frac{\partial k}{\partial x_j}\right)+G_k+Y_k+S_k \tag{23}$$

$$\frac{\partial}{\partial t}(\rho \omega)+\frac{\partial}{\partial x_i}(\rho \omega u_i)=\frac{\partial}{\partial x_j}\left(\Gamma_k \frac{\partial \omega}{\partial x_j}\right)+G_\omega+Y_\omega+D_\omega+S_\omega \tag{24}$$

Constants of the BSL k-ω model are presented in Table 1 (e).

Table 1 (e) illustrates the different constants of the BSL k-ω turbulence model.

To make the SST k-ω turbulence model more accurate, it includes all the refinements of the BSL k-ω turbulence model. Constants of the SST turbulence k-ω model are presented in Table 1 (f).

3.4. Choice of the Turbulence Model

The effect of the turbulence model on the numerical results have been studied in this section in order to achieve the adequate model. In fact, different turbulence models were studied using the software “Ansys Fluent 17.0” for solving the governing equations. Particularly, we have compared the BSL k-ω turbulence model, the standard k-ω turbulence model, the standard k-ε turbulence model, the SST k-ω turbulence model, the Realizable k-ε turbulence model and the RNG k-ε turbulence model. In the viewed direction set by the intersection of the two planes x = 0.06 m and z = -0.005 m, the superposition of the experimental results with the velocity profiles for the different turbulence models are presented in Figure 4. According to these results, the same profiles of the velocity have been observed and the values take down of the turbulence model. Particularly, it has been observed that the value founded with the experimental data is nearest to the standard k-ω tubulence model results. This study tends to show that the standard k-ω turbulence model is the most efficient to model the air flow in the present application. Therefore, the overall error designed between the numerical and the experimental data is equal to 5%. Thus, we found that the numerical results are in good agreement with the experimental data which confirms the validity of the numerical method.

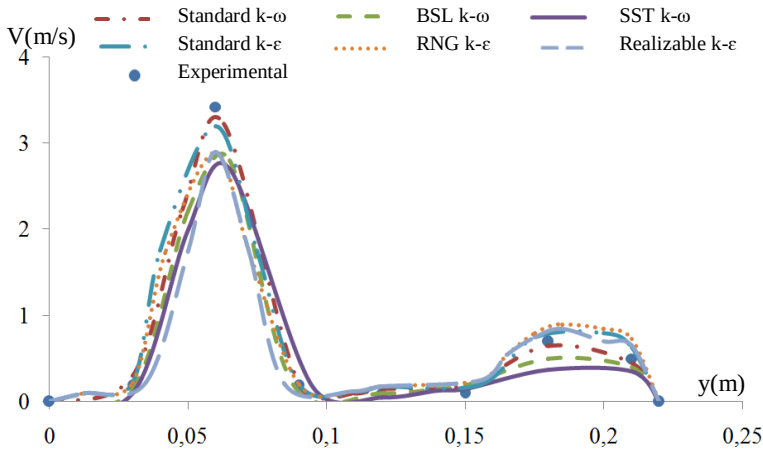

Figure 4. Velocity profiles in the direction defined by z = -0.005 m and x = 0.06 m.

4. Results and Discussion

The distribution of the velocity fields, the temperature, the total pressure, the turbulent kinetic energy and the turbulent viscosity are studied in this section. In the present study, the employed Reynolds number is equal to Re = 5100.

4.1. Velocity Fields

The distribution of the velocity fields in the plane defined by x = 0.06 m is shown in Figure 5 for the different studied turbulence models. From these results, it has been observed a discharge zone at the box inlet hole in all cases with average velocity equal to V = 3.4 $m.s^{-1}$. The inlet flow barges into the reverse wall of the box and then it moves inside the box with a turbulent behavior to evacuate through the top hole. Otherwise, both axial directions of the airflow are seen inside the box. The recirculation zone appeared in the whole area of the box is created by the change of the flow direction, specially by the first ascending flow. Meanwhile, the weak zone showed in the down area of the box is created by the second descending flow. In these conditions, the averaged velocity presents a very low value in the whole system when exclude the values in the discharge area which reaches V = 1.3 $m.s^{-1}$. The comparison between the different turbulence models affirms that the choice of

the adequate model presents a straight effect on the velocity fields. Particularly, it is noticed that the recirculation zone has been involved by the turbulence model choice. In this situation, the maximum value of the averaged velocity is obtained for the SST k-ω turbulence model and it reachs V = 4.75 $m.s^{-1}$. However, the minimum value is founded for the standard k-ε turbulence model and it reachs V = 4.42 $m.s^{-1}$.

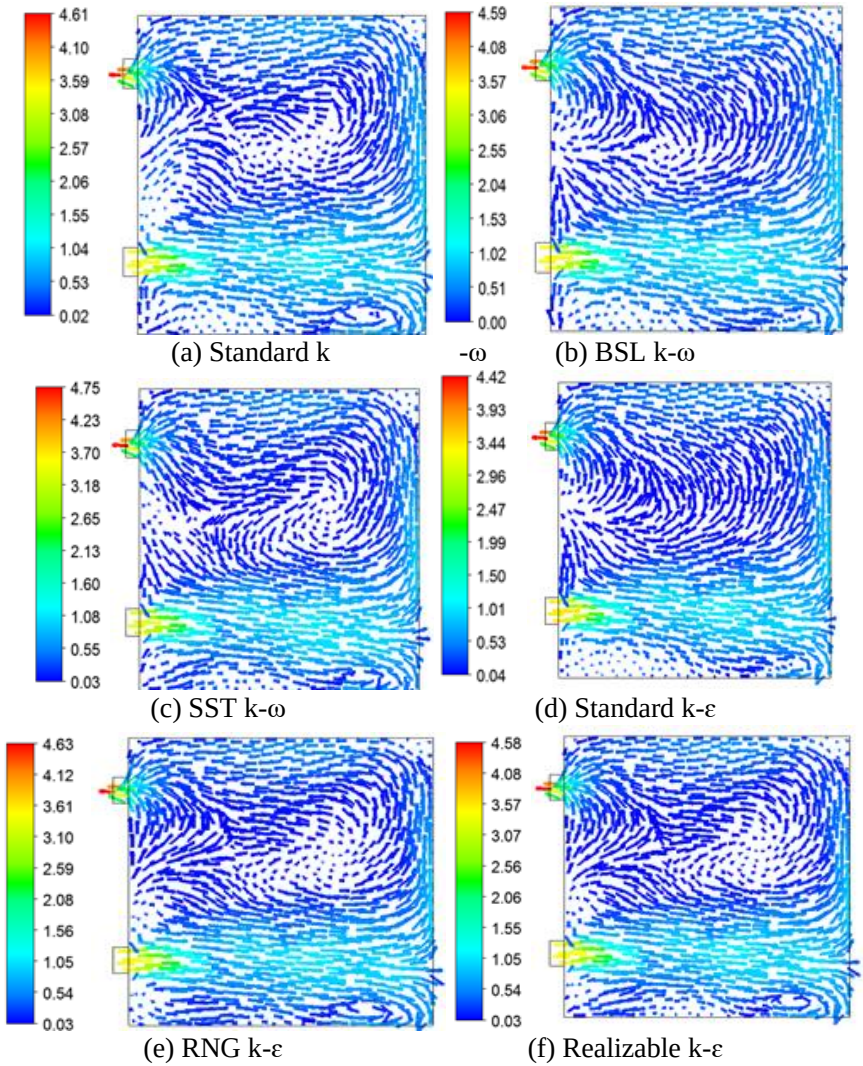

(a) Standard k -ω (b) BSL k-ω

(c) SST k-ω (d) Standard k-ε

(e) RNG k-ε (f) Realizable k-ε

Figure 5. Velocity fields.

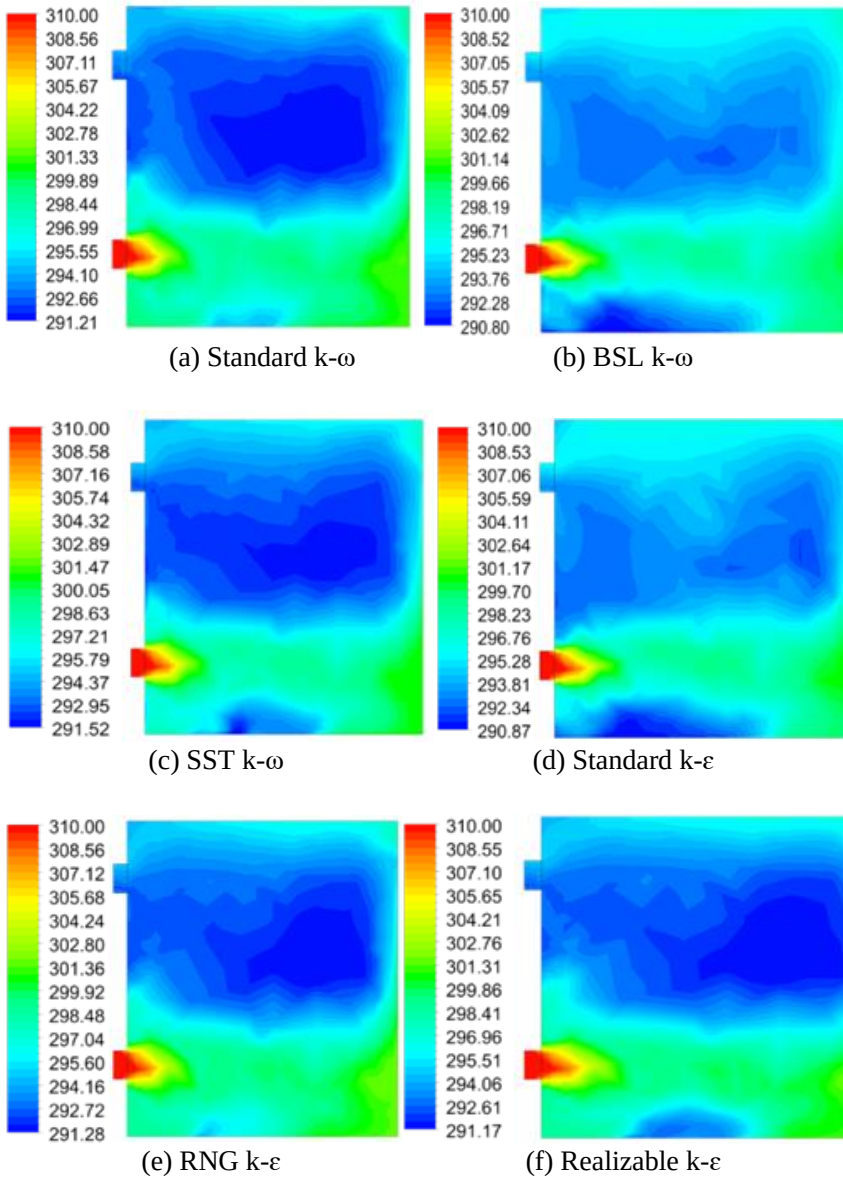

Figure 6. Distribution of the temperature.

4.2. Temperature

The distribution of the air temperature at t = 2 s and in the plane defined by x = 0.06 m is shown in Figure 6 for the considered turbulence models. According to these results, it has been observed that the temperature at the hole inlet is equal to T = 310 K while, it slightly decreases in the discharge area, at the hole inlet. However, the temperature decreases above the discharge area due to the recirculation region appeared into the whole area of the box prototype. Otherwise, the air temperature decreases gradually to reaches the minimum values at the system outlet with a value equal to T = 290 K. The comparison between the founded results affirms that the choice of the turbulence model presents a straight effect on the temperature distribution. Particularly, it has been noted that the minimum value of the temperature is obtained in the hole outlet for the BSL k-ω turbulence model and it is equal to T = 290.8 K. However, the maximum value of the temperature reaches T = 291.5 K for the SST k-ω turbulence model.

4.3. Total Pressure

Figure 7 shows the distribution of the total pressure in the plane defined by x = 0.06 m for all considered turbulence models. From these results, it is clear that a compression zone appears in the down hole of the box prototype for all cases. In fact, the total pressure decreases in the expulsion area, produced from the system inlet and attacked until the reverse wall of the box. This fact can be clarified by the recirculation zone showed at the whole area of the box prototype. From that point onward, the total pressure increases to reaches the peak value at the opposite wall. However, a depression zone is appeared at the top hole in the system outlet for all cases. A comparison between the different turbulence models gives that the turbulence model presents a straight effect on the distribution of the total pressure. In fact, it has been noted that the maximum value of the total pressure is founded for the standard k-ω and the SST k-ω turbulence models and presents a value equal to p = 101342 Pa. This value decreases slightly for the other turbulence models and reaches the minimum value equal to p = 101340 Pa, for the standard k-ε turbulence model.

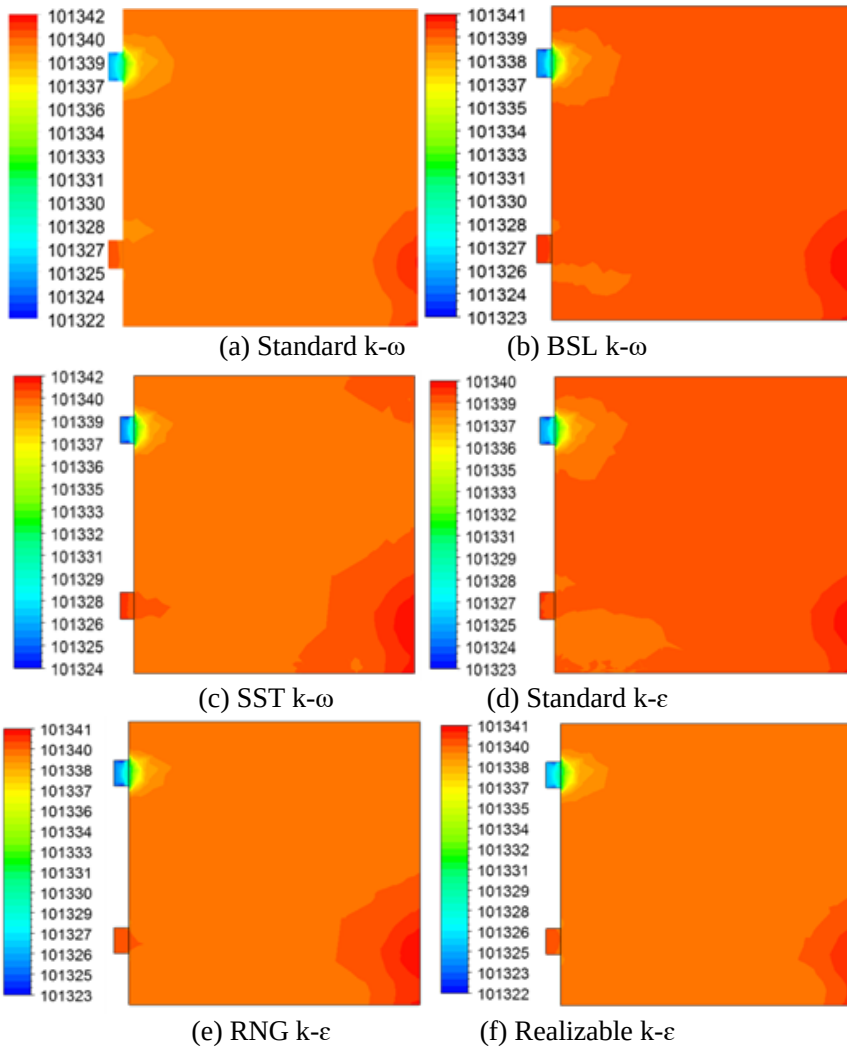

Figure 7. Distribution of the total pressure.

4.4. Turbulent Kinetic Energy

Figure 8 depicts the distribution of the turbulent kinetic energy in the plane defined by x = 0.06 m for the considered turbulence models. From these results, it can be seen that the turbulent kinetic energy presents a small value at the system inlet. In mean time, the turbulent kinetic energy increases

gradually in the expulsion area created in the down hole of the box. Otherwise, it has been observed that the maximum values of the turbulent kinetic energy appear at the discharge area near the reverse wall and at the top hole of the box outlet. As causes the other air proprieties, this fact is owing to the recirculation zone in the whole area of the box.

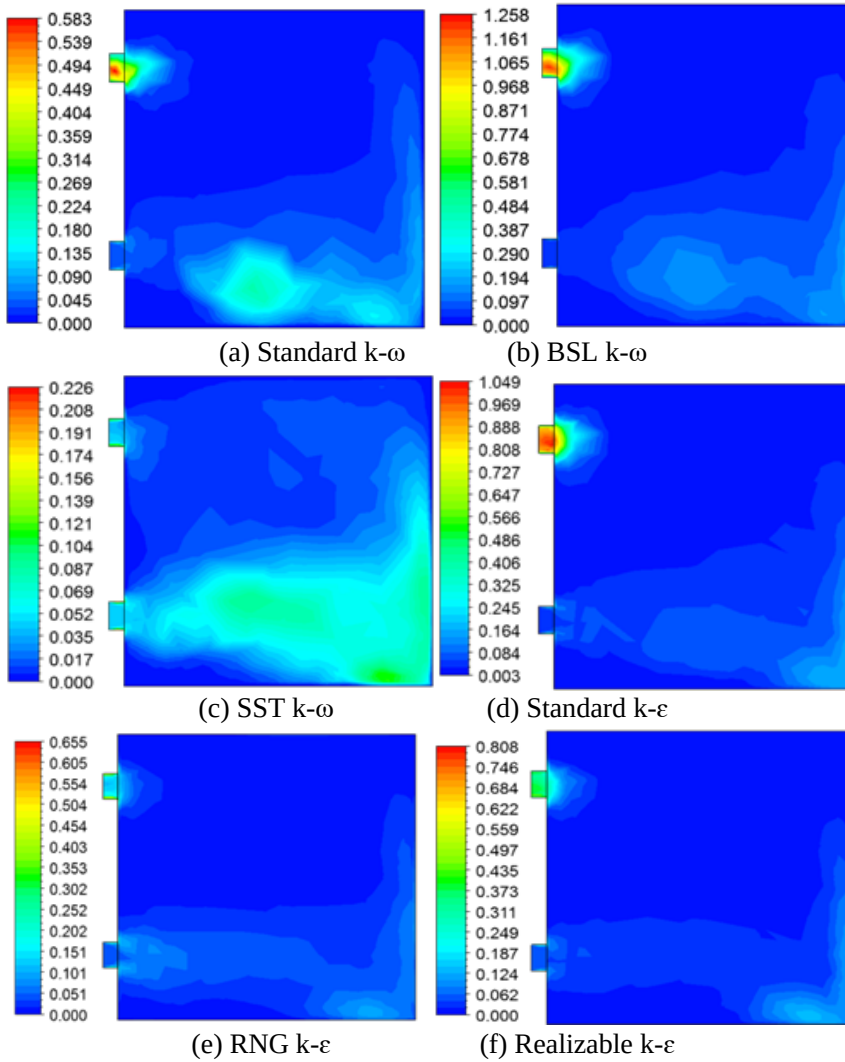

Figure 8. Distribution of the turbulent kinetic energy.

Indeed, the distribution of the turbulent kinetic energy in the four considered turbulence models affirms that the turbulence model presents a straight effect on the distribution of the turbulent kinetic energy. In fact, it has been observed that the maximum value of the turbulent kinetic energy is obtained in the hole outlet and it reaches $k = 1.258\ m^2.s^{-2}$ for the BSL k-ω turbulence model. However, this value reaches a low value, which is about $k = 0.226\ m^2.s^{-2}$, for the SST k-ω turbulence model.

4.5. Turbulent Viscosity

Figure 9 shows the distribution of the turbulent viscosity in the plane defined by x = 0.06 m and for the four turbulence models. According to these results, it can be seen that the turbulent viscosity presents a small value at the box inlet for all cases. However, the turbulent viscosity rises at the expulsion area which shown in the down hole of the system. The maximum values of the turbulent viscosity appear in the discharge area near the reverse wall. Otherwise, a peak value appears at the top hole of the box prototype due to the recirculation zone of the hot air in this region. By comparison of the obtained results, it has been observed a small effect of the different studied models on the distribution of the turbulent viscosity. In fact, the extension of the wake zone distinctiveness of the maximum values of the turbulent viscosity, obtained in the discharge area near the reverse wall, is more developed for the BSL k-ω turbulence model. Using this model, the maximum value of the turbulent viscosity reaches $\mu_t = 0.00192\ kg.m^{-1}.s^{-1}$ in the hole outlet. However, this parameter presents a low value equal to $\mu_t = 0.00032\ kg.m^{-1}.s^{-1}$ for the RNG k-ε turbulence model in the discharge area. In this case, the turbulent viscosity continues to decrease immensely in the outlet hole.

Conclusion

The present paper aims to investigate the impact of the turbulent model on the heat ventilation studied in a box prototype. Particularly, a computational study and an experimental validation have been developed to compare the standard k-ω, the SST k-ω, the BSL k-ω, the standard k-ε, the Realizable k-ε and the the RNG k-ε turbulence models. From the obtained results, it is noticed that the aerodynamic characteristics presents the same emergence nevertheless the

maximum values depend on the turbulence model. Particularly, it has been noted that the value founded with the standard k-ω tubulence model is nearest to the experimental data. This study tends to show that the standard k-ω turbulence model is the most efficient model to analyze the air flow in the box prototype. In the future, we suggest to extend this application with others geometrical arrangements.

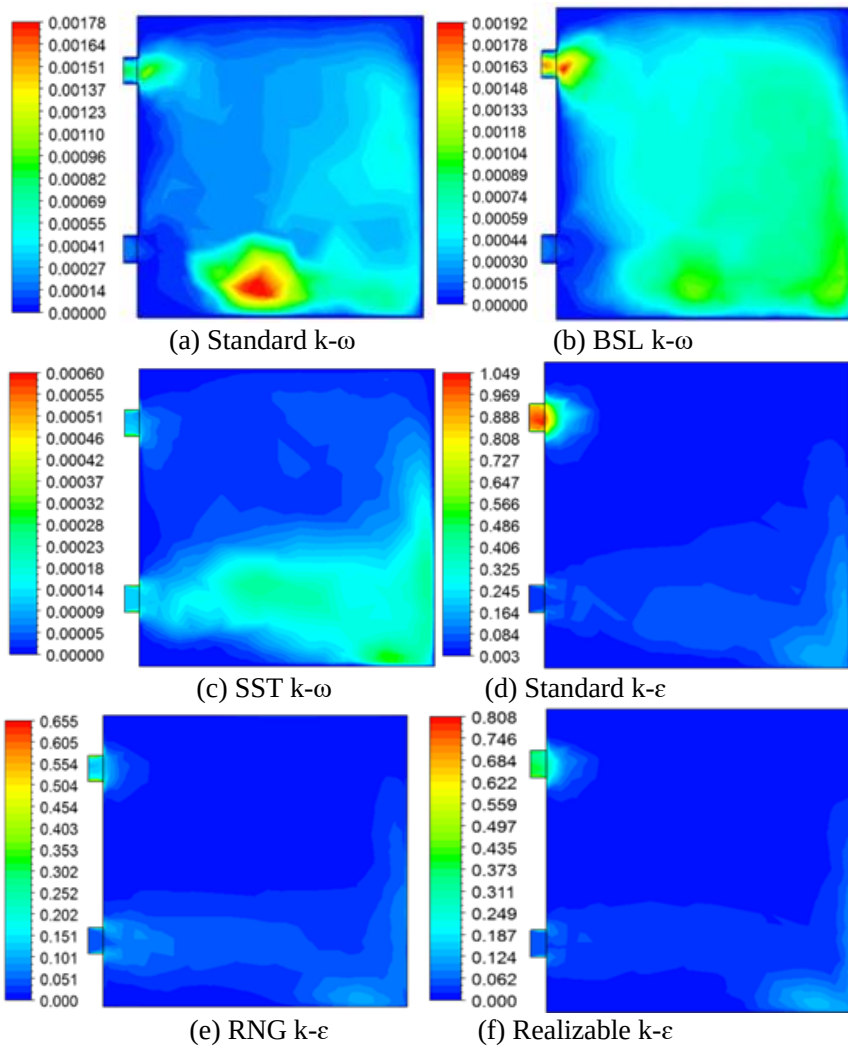

Figure 9. Distribution of the turbulent viscosity.

References

[1] S. Driss, Z. Driss, I. Kammoun, computational study and experimental validation of the heat ventilation in a living room with a solar patio system, *Energy and Building*, 119 (2016) 28-40.

[2] A. Ayadi, Z. Driss, A. Bouabidi, H. Nasraoui, M. Bsisa, M. S. Abid, A computational and an experimental study on the effect of the chimney height on the thermal characteristics of a solar chimney power plant, *Journal of Process Mechanical Engineering*, 231 (2017) 1-14.

[3] S. Driss, Z. Driss, I. Kammoun, Numerical simulation and wind tunnel experiments on wind-induced natural ventilation in isolated building with patio, *Energy*, 90 (2015) 917-925.

[4] H. Benguesmia, B. Bakri, Z. Driss, Effect of the turbulence model on the heat ventilation analysis in a box prototype, *Diagnostyka*, 21(3) (2020), 55-66.

[5] B. Bakri, S. Driss, A. Ketata, Z. Driss, H. Benguesmia, F. Hamrit, Study of the heat ventilation in a box prototype with the k-ω turbulence model, *Transylvanian Review Journal*, Vol XXXVI (30) (2018)7989-8000.

[6] B. Bakri, O. Eleuch, A. Ketata, S. Driss, Z. Driss, H. Benguesmia, Study of the turbulent flow in a newly solar air heater test bench with natural and forced convection modes, *Energy*, 161(2018)1028-1041.

[7] B. Bakri, A. Ketata, S. Driss, H. Benguesmia, Z. Driss, F. Hamrit, Unsteady investigation of the heat ventilation in a box prototype, *International Journal of Thermal Sciences*, 135 (2019)285-297.

[8] C. Teodosiu, F. Kuznik, R. Teodosiu, CFD modeling of buoyancy driven cavities with internal heat source: Application to heated rooms, 68 (2014) 403-411.

[9] X. Du, R. Bokel, A. V. D. Dobbelsteen, Building microclimate and summer thermal comfort in free-running buildings with diverse spaces: a Chinese vernacular house case, *Build. Environ.*, 822 (2014) 15-227.

[10] R. Z. Homod, Assessment regarding energy saving and decoupling for different AHU (air handling unit) and control strategies in the hot-humid climatic region of Iraq, *Energy*, 74 (2014) 762-774.

[11] F. J. Terrados, D. Moreno, "Patio" and "Botijo": Energetic strategies' architectural integration in"Patio 2.12" prototype. *Energy and Buildings*, 83 (2014) 70-88.

[12] E. Yasa, Microclimatic comfort measurements evaluation of building physics: The effect of building form and building settled area, on pedestrian level comfort around buildings, *Journal of Building Physics*, 40 (2016) 472-500.

[13] M. Premrov, V. Z. Leskovar, K. Mihalic, Influence of the building shape on the energy performance of timber-glass buildings in different climatic conditions, *Energy*, 108 (2016) 201-211.

[14] D. Johnston, Dominic Miles-Shenton, David Farmer, Quantifying the domestic building fabric 'performance gap,' *Building Services Engineering Research and Technology*, 36 (2015) 614-627.

[15] A. L. S. Chan, Investigation on the appropriate floor level of residential building for installing balcony, from a view point of energy and environmental performance. A case study in subtropical Hong Kong, *Energy*, 85 (2015) 620-634.

[16] M. Ibrahim, E. Wurtz, P. H. Biwole, P. Achard, Transferring the south solar energy to the north facade through embedded water pipes, *Energy*, 78 (2014) 834-845.

[17] Y. Nam, H. B. Chae, Numerical simulation for the optimum design of ground source heat pump system using building foundation as horizontal heat exchanger, *Energy*, 73 (2014) 933-942.

[18] M. R. Alam, M. F. M. Zain, A. B. M. A. Kaish, M. Jamil, Underground soil and thermal conductivity materials based heat reduction for energy-efficient building in tropical environment, *Indoor and Built Environment*, 24 (2013) 185-200.

[19] C. Rode, Global building physics, *Journal of Building Physics*, 36 (2012) 337-352.

[20] H. J. Han, Y. I. Jeon, S. H. Lim, W. W. Kim, K. Chen, New developments in illumination, heating and cooling technologies for energy-efficient buildings, *Energy*, 35 (2010) 2647-2653.

[21] K. J. Watson, J. Evans, A. Karvonen, T. Whitley, Re-conceiving building design quality: A review of building users in their social context, *Indoor and Built Environment*, 25 (2014) 509-523.

[22] D. J. Sailor, T. B. Elley, M. Gibson, Exploring the building energy impacts of green roof design decisions - a modeling study of buildings in four distinct climates, *Journal of Building Physics*, 35 (2011) 372-391.

[23] B. Bakri, S. Driss, A. Ketata, H. Benguesmia, F. Hamrit, Z. Driss, Study of the meshing effect on the turbulent flow in a building system with a k-ω turbulence model. *International Conference on Mechanics and Energy (ICME'2016)*, December 22-24 2016, Hammamet, Tunisia.

[24] B. Bakri, A. Ketata, S. Driss, H. Benguesmia, F. Hamrit, Z. Driss, Effect of the turbulence model on the aerodynamic structure to evaluate the thermal comfort in a building system, *International Conference on Mechanics and Energy (ICME'2016)*, December 22-24 2016, Hammamet, Tunisia.

[25] B. Bakri, A. Ketata, S. Driss, Z. Driss, H. Benguesmia, F. Hamrit, Unsteady simulation of the aerodynamic structure in a heated box prototype, *International Conference on Mechanics and Energy (ICME'2017)*, December 18-20 2017, Sousse, Tunisia.

[26] B. Bakri, S. Driss, A. Ketata, Z. Driss, H. Benguesmia, F. Hamrit, Study of the turbulent flow in a box prototype with the k-ω turbulence model, *Congrès Algérien de Mécanique, (CAM2017-289)*, 26-30 Novembre, Constantine-Algérie.

[27] B. Bakri, H. Benguesmia, A. Ketata, S. Driss, Z. Driss, F. Hamrit, Study of the natural convection flow in a solar air heater test bench, *International Conference on Mechanics and Energy (ICME'2018)*, December 20-22 2018, Hammamet, Tunisia.

[28] B. Bakri, H. Benguesmia, A. Ketata, H. Nasraoui, Z. Driss, Performance evaluation of the natural-convection of a solar air-heater with a plate absorber, *International Conference on Mechanics and Energy (ICME'2018)*, December 19-21 2019, Monastir, Tunisia.

[29] B. Bakri, H. Benguesmia, Study of the forced convective heat transfer in a solar air heater, *The First International Conference on Materials, Energy and Environment (MEE'2020, N°: EO05)*, January 20-21, 2020, El Oued University, Algeria.

[30] B. Bakri, H. Benguesmia, A. Ketata, S. Driss, Z. Driss, A comparative study of the turbulence models on the heat ventilation in a box prototype, *1ère Conférence*

National sur: la Transition Énergétique en Algérie Conférence (CNTEA1-2020), Mars 8-9, 2020, M'sila, Algeria.

[31] B. Bakri, H. Benguesmia, A. Ketata, S. Driss, Z. Driss, Choice of the appropriate turbulence model for modeling the air flow inside a room, *1ère Conférence National sur: la Transition Énergétique en Algérie Conférence (CNTEA1-2020)*, Mars 8-9, 2020, M'sila, Algeria.

[32] B. Bakri, H. Benguesmia, A. Ketata, S. Driss, Z. Driss, CFD Based performance analysis of a solar air heater test bench with unsteady turbulent flow, *9ème Journées des sciences de l'ingénieur JSI'2020*, September 25-27, 2020, Sfax, Tunisia.

[33] Z. Driss, O. Mlayeh, D. Driss, M. Maaloul, M. S. Abid, Numerical simulation and experimental validation of the turbulent flow around a small incurved Savonius wind rotor. *Energy*, 74 (2014) 506-517.

[34] Z. Driss, G. Bouzgarrou, W. Chtourou, H. Kchaou, M. S. Abid. Computational studies of the pitched blade turbines design effect on the stirred tank flow characteristics. *European Journal of Mechanics B/Fluids*, 29 (2010) 236-245.

[35] Z. Driss, O. Mlayah, S. Driss, M. Maaloul, M. S. Abid, Study of the incidence angle effect on the aerodynamic structure characteristics of an incurved Savonius wind rotor placed in a wind tunnel, *Energy*, 113 (2016) 894-908.

[36] Z. Driss, O. Mlayah, S. Driss, D. Driss, M. Maaloul, M. S. Abid, Study of the bucket design effect on the turbulent flow around unconventional Savonius wind rotors, *Energy*, 89 (2015) 708-729.

Chapter 4

Ventilation System Performance in a Heated Room Testing the Indoor Air Quality and Thermal Comfort

Sondes Ifa* and Zied Driss

Laboratory of Electro-Mechanic Systems (LASEM),
National School of Engineers of Sfax (ENIS),
University of Sfax (US), Sfax, Tunisia

Abstract

In relation with the study of the indoor air quality (IAQ) and the thermal comfort, the main goal of the major researches was the prediction of the thermal sensation for the existing persons in daily and working spaces. In this chapter, we are interested on the numerical simulations in room containing a sitting person and computer. The considered study uses the computational fluid dynamic (CFD) tool. In this case, ANSYS Fluent 17. software was employed. It is based on the resolution of the Navier Stokes equation using the finite volume method. The distribution of the temperature, velocity, turbulent kinetic energy, turbulent viscosity and dissipation rate were evaluated in different visualization directions and planes. Similarly, the indoor thermal comfort was tested by determining the predicted mean vote (PMV). The developed numerical results demonstrate that the presence of the heat sources affects the indoor air flow. Indeed, it causes the perturbation of the air flow and the non-homogeneity of the air characteristic. In addition, the thermal sensation is slightly hot. The adequate mesh and turbulence model are in good accord with the experimental data found from the literature.

* Corresponding Author's Email: ifa.sondes@yahoo.fr.

In: Indoor Air Quality
Editor: Robert M. Ridgway
ISBN: 979-8-88697-134-7

Keywords: ventilation, airflow, CFD, manikin, computer, indoor air quality, thermal comfort, PMV

Nomenclature

$C_{1\varepsilon/2\varepsilon/\mu}$	Constants of the k-ε turbulence models (dimensionless)
C_p	Specific heat ($J.kg^{-1}.K^{-1}$)
G_b	Generation of the kinetic energy due to the buoyancy ($kg.m^{-1}.s^{-3}$)
G_k	Generation of the kinetic energy due to the mean velocity ($kg.m^{-1}.s^{-3}$)
H	Room height (m)
H_f	Heat flux (W)
H_m	Manikin height (m)
k	Turbulent kinetic energy ($J.kg^{-1}$)
L	Room length (m)
M	Metabolic rate ($W.m^{-2}$)
P	Pressure (Pa)
Q	Flow rate ($m3.h^{-1}$)
T	Temperature (K)
T_a	Air temperature (°C)
W	Room width (m)
X_{ij}	Cartesian coordinate (m)
λ	Thermal conductivity ($W.m^{-2.}K^{-1}$)
ρ	Density ($kg.m^{-3}$)
μ	Viscosity ($kg.m^{-1}.s^{-1}$)
μ_t	Turbulent viscosity ($kg.m^{-1}.s^{-1}$)
δ_{ij}	Mean strain rate tension (dimensionless)
ε	Dissipation rate of the turbulent kinetic energy ($m^2.s^{-3}$)
$\sigma_{\varepsilon/k}$	Turbulent Prandtl number of ε and k (dimensionless)
$r_{\omega/k}$	Effective diffusivity of k and ω ($kg.m^{-2}$).

1. Introduction

Nowadays, the health and thermal comfort becomes a human necessity especially in case of the development of a new pollutants and contaminants as

COVID-19 virus. Therefore, the heating, ventilation and air conditioning HVAC systems are significantly employed in order to maintain a healthy indoor air. Additionally, to the thermal need, a reasonable energetic consumption is desired [1, 2]. In fact, the thermal and energetic study is developed using different numerical methods.

The Computational Fluid Dynamic (CFD) approach is a useful tool to characterize the HVAC systems efficiency in the occupied buildings. In this context, Murakami et al., [3] affirmed the importance of the CFD in the airflow characterization. The choice of the turbulent models and the boundary conditions is a basic step to obtain a precise numerical results that clearly explains the physical phenomenon. In this regard, the turbulent model for the Reynolds-Averaged Navier Stokes (RANS) approach are summarized by Zhai et al., [4]. The most employed turbulent models are the model with two equations as the k-ε and the k-ω turbulence models. The dependence between these models and the thermal description is examined by Zelensky et al., [5]. Similarly, same researchers used experimental techniques for the purpose of heat transfer study. In this way, the formation of the thermal plume above the head person was studied using the thermal imaging camera. Based on their study, it has been noted that the k-ε turbulent models are advantageous for the thermal simulation.

The correlation between the inlet velocity and the air distribution in an occupied space was tested by Mohammed [6]. He affirmed that the inlet velocity increase is not preferable in order to optimize the energy consumption. In addition, Chen et al., [7] examined the heat flow impact of the manikin. Based on the experimental results given by Xu et al., [8], Ahmed and Gao [9] studied a novel local exhaust ventilation system. They investigated the thermal comfort for existing person employing the predicted mean vote PMV and predicted percent of dissatisfied (PPD).

According to these previous studies, we have focused on the CFD simulations in order to analyze the indoor air flow in a room occupied by two heat sources. In this context, we have examined the impact of the meshing and the turbulent models on the indoor air quality for the purpose to select the most appropriate mesh and turbulence model. The numerical results developed by ANSYS Fluent 17.0 are approved by the experimental data developed by Xu et al., [8].

2. Geometrical System

The geometry employed in this study is prepared by SolidWorks software. This geometry is studied experimentally by Xu et al., [8]. Figures 1 and 2 show the geometrical parameters and dimensions of the investigated room. The dimensions of the considered room present a length L = 6 m, a width W = 3.9 m and a height H = 2.35 m as shown in Figure 2. The inlet opening is characterized by a length equal to l_i = 0.4 m and a width equal to w_i = 0.15 m. In addition, the outlet has a length equal to l_o = 0.34 m and a width equal to w_o = 0.14 m. The heat source examined in this works are the sitting manikin and the computer.

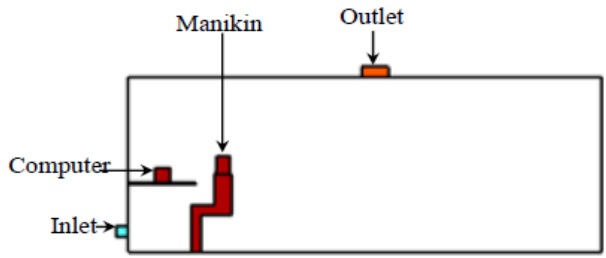

Figure 1. Geometrical dimensions.

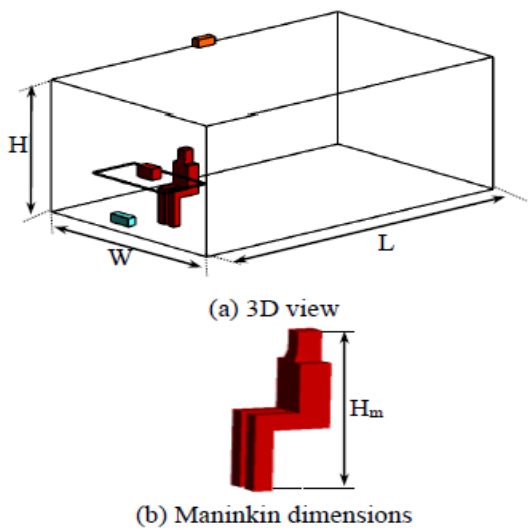

Figure 2. Geometrical dimensions.

3. Numerical Method

3.1. Boundary Conditions

The boundaries conditions are directly related to the stability of the results and they are applied for the whole domain. In fact, Table 1 sums up the considered boundary conditions and the temperature values of the different walls. Two heat sources are considered on the experimental study done by Xu et al., [8]. A heating panels are used to generate a heat flux equal to H_F = 76 W for the manikin and a lamp to generate a heat flux equal to H_F = 40 W for the computer. In the inlet, the air is characterized by a temperature equal to T = 19°C and a flow rate equal to Q = 43 $m^3 h^{-1}$. Table 2 presents the air properties. At the outlet, the pressure is equal to the atmospheric conditions.

Table 1. Boundary conditions

Boundary conditions		Values			
		Temperature T (°C)	Supply rate Q ($m^3.h^{-1}$)	Pressure P (Pa)	Heat flux H_f (W)
Inlet		19	43	-	-
Manikin		-	-	-	76
Computer		-	-	-	40
Outlet		-	-	0	-
Walls	East	25	-	-	-
	West	24.5	-	-	-
	North	24.8	-	-	-
	South	24.8	-	-	-
	Ceiling	24.9	-	-	-
	Floor	23.9	-	-	-

Table 2. Air properties

Properties	Values
Density	$\rho = 1.225\ kg.m^{-3}$
Specific heat	$C_p = 1006.43\ J.kg^{-1}.K^{-1}$
Thermal conductivity	$\lambda = 0.0242\ W.m^{-1}.K^{-1}$
Viscosity	$\mu = 1.7894\ 10^{-5}\ kg.m^{-1}.s^{-1}$

3.2. Mathematical Formulation

For the study of the Heating, ventilation and air conditioning (HVAC) systems and its optimization, the Computational Fluid Dynamics (CFD) analysis is developed. It is based on the resolution of the Navier Stokes equations [10].

In fact, the airflow characterization is governed by the continuity equation and the momentum equation which are presented as:

$$\frac{\partial r}{\partial t}+\frac{\partial (r\ u_i)}{\partial x_i}=0 \tag{1}$$

$$\frac{\partial (\rho u_i)}{\partial t}+\frac{\partial (\rho u_i u_j)}{\partial x_j}=-\frac{\partial p}{\partial x_i}+\frac{\partial}{\partial x_i}[\mu (\frac{\partial u_i}{\partial x_j}+\frac{\partial u_j}{\partial x_i}-\frac{2}{3}\delta_{ij}\frac{\partial u_i}{\partial x_i})]+\frac{\partial (-\rho \overline{u_i' u_j'})}{\partial x_j} \tag{2}$$

where ρ is the density (kg.m^{-3}), p is the pressure (Pa), μ is the dynamic viscosity (kg.m^{-1}.s^{-1}), x_i is the caractesian coordinate (m) for i = 1, 2 and 3, u_i is the velocity component (m.s^{-1}) in the x_i direction, δ_{ij} is the mean strain rate tension, $\overline{u_i' u_j'}$ is the Reynolds stresses.

The Reynolds constraints and the average velocity gradient are linked by the Boussinesq hypothesis. This hypothesis is used for k-ε and k-ω turbulence models. It is characterized by a relatively acceptable calculation coast with the turbulent viscosity calculation. For the k-ε and k-ω turbulence models, the resolution of the two additionally transport equation for the turbulent kinetic energy k and the dissipation rates ε and ω. The turbulent viscosity μ_t is calculated as function of k and ε. The Boussinesq hypothesis equations are written as follows:

$$-\rho \overline{u_i' u_j'}=\mu_t[\frac{\partial u_i}{\partial x_j}+\frac{\partial u_j}{\partial x_i}]-\frac{2}{3}[\rho k+\mu_t \frac{\partial u_i}{\partial x_i}]\delta_{ij} \tag{3}$$

The turbulent viscosity for the k-ω turbulence model is written as follows:

$$\mu_t = \rho \alpha^* \frac{k}{\omega} \tag{4}$$

where:

$$\alpha^* = \alpha_\infty \left(\frac{\alpha^*_0 + \frac{Re_t}{R_k}}{1 + \frac{Re_t}{R_k}} \right) \tag{5}$$

$$Re_t = \frac{\rho k}{\mu \omega} \tag{6}$$

$$\alpha^*_0 = \frac{\beta_i}{3} \tag{7}$$

where $R_k = 6$ and $\beta_i = 0.072$.

3.3. Meshing Choice

The characterization of the air flow along the all domain is based on the discretization of this domain on elementary volume. In fact, the considered mesh is unstructured formed by tetrahedral elements. It is locally refined in the important gradient area. The meshing choice is based on the comparison of the temperature and the velocity between different meshes with cells numbers range from 309927 to 2466198. These meshing are shown in Figure 3. The temperature and velocity profiles are taken along the direction defined by y = 0.29 m, y = -0.1 m and y = -0.45 m as shown in Figure 4. Indeed, the distribution of the temperature and the velocity are shown along these directions. Based on these results, it has been observed that the temperature increases reaching the ceiling. Around the manikin, it reaches T = 299 K at a height equal to H = 1.8 m. According to the velocity results presented in Figure

6, it has been noted that the good agreement with the experimental data is given with the 2166447 cells and 2466198 cells. In these conditions, the velocity is lower than V = 0.1 $m.s^{-1}$ for the zone occupied by the manikin. Consequently, we affirm that the domain refinement with 2166447 elements is in good agreement with the experimental study [8].

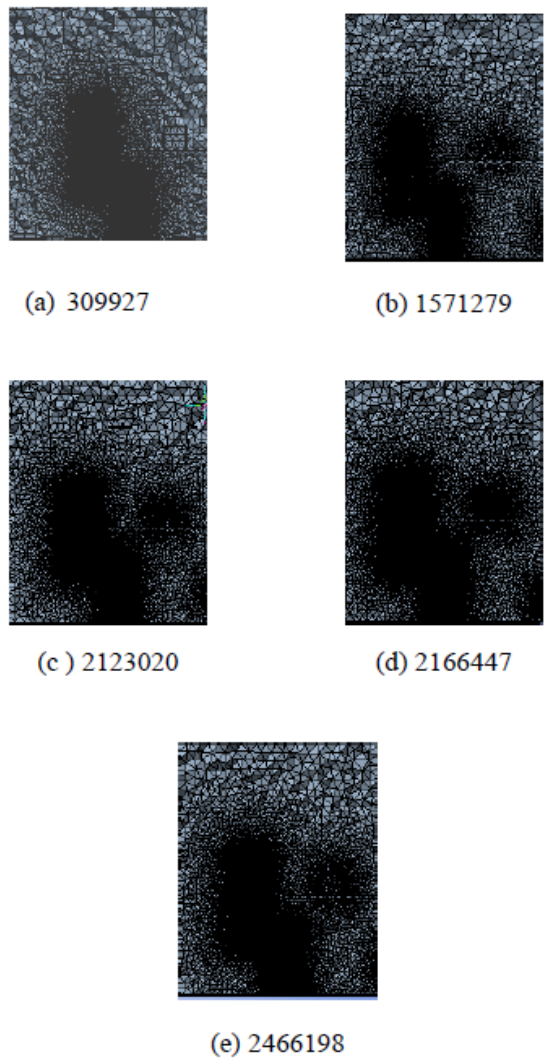

Figure 3. Meshing.

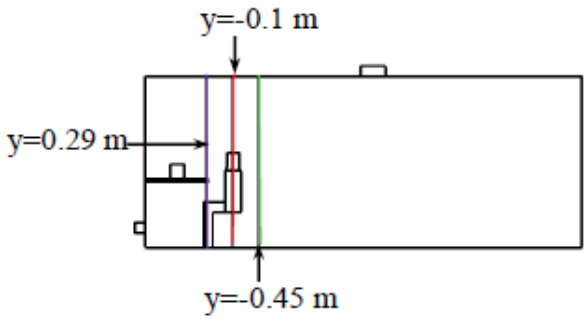

Figure 4. Visualization directions.

3.4. Turbulence Model Choice

The aim of this section is to choose the appropriate turbulence model. This choice is based on the comparison between the temperature and velocity results given by different turbulence models. Figure 5 presents the temperature distribution for the standard k-ε model, the RNG k-ε model, the standard k-ω model and the SST k-ω model along four directions. These directions are defined by y = 0.29 m, y = -0.1 m and y = -0.45 m. The comparison between the numerical and the experimental results proves that the RNG k-ε values are nearest to the experimental values. Figure 6 presents the velocity distribution in the same considered directions. Depending on these results, the biggest error from the experimental values is predicted for the k-ω models. However, the RNG k-ε gives the numerical values that are in good agreement with the experience in the majority of the points.

4. Local Results

In this section, the distribution of the temperature, the velocity fields, the static pressure, the turbulent kinetic energy, the dissipation rate of the turbulent kinetic energy and the turbulent viscosity are shown. These results are presented in the planes defined by x = 0.2 m, x = 1.9 m, y = -0.1 m and y = -0.4 m as displayed in Figure 7.

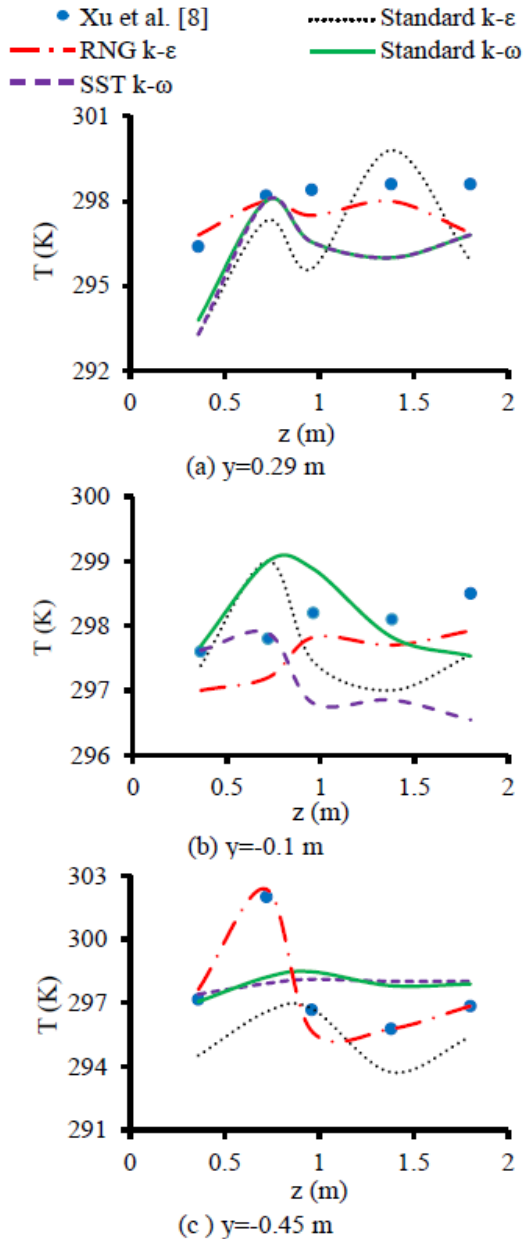

Figure 5. Temperature profiles along the different direction.

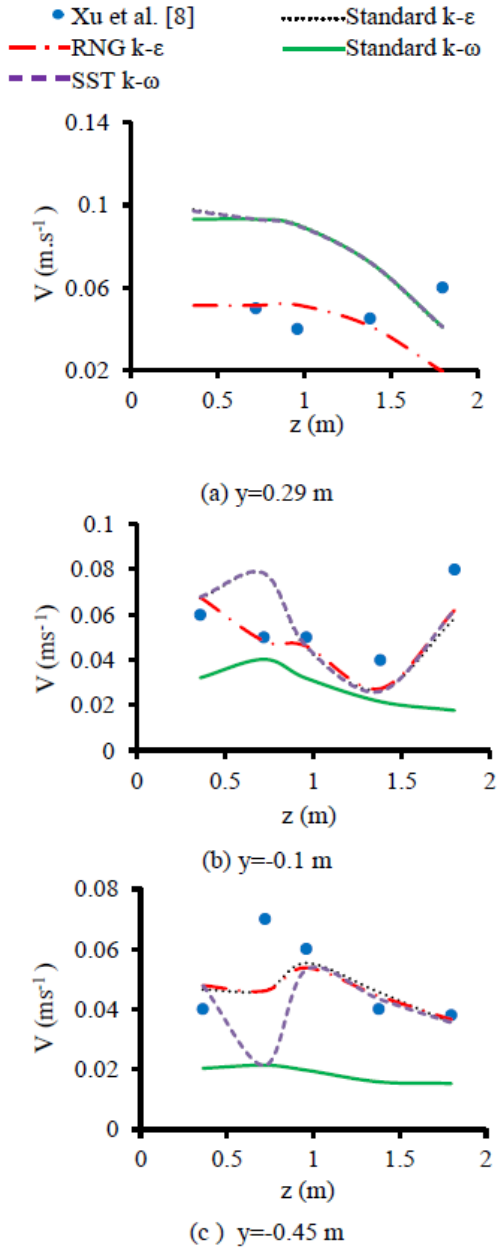

Figure 6. Velocity profiles along the different directions.

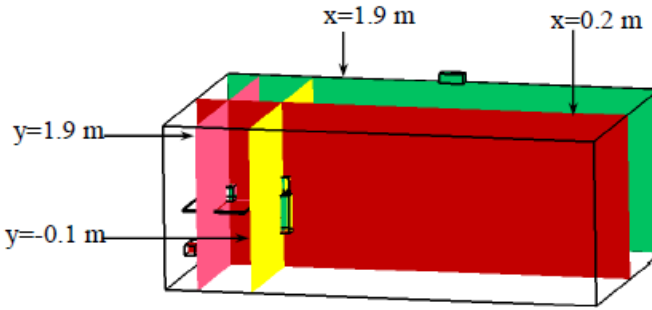

Figure 7. Visualization planes.

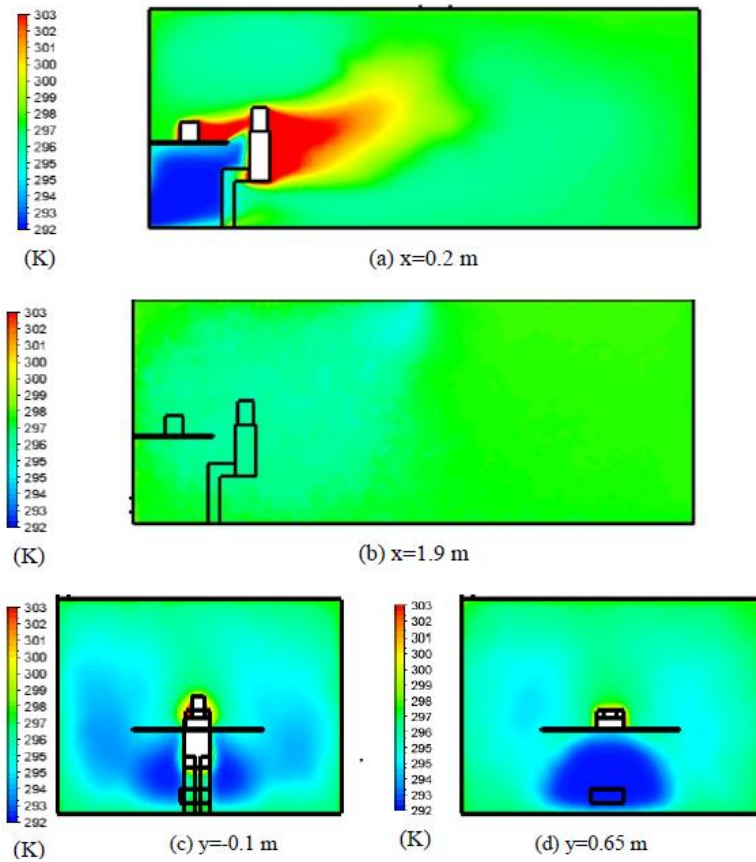

Figure 8. Temperature distribution in different planes.

4.1. Temperature

Figure 8 presents the temperature distribution in the planes defined by x = 0.2 m, x = 1.9 m, y = -0.1 m and y = 0.65 m. Based on these results, it has been noted that the thermal plume was formed around the manikin and the computer. This formation is explained by the temperature difference between the human body and the indoor environment. Therefore, the heat transfer between theses surfaces causes the formation of this plume [11-14]. In this zone, the temperature is equal to T = 303 K. Below the table and near to the floor, the coldest zone was formed where the temperature is equal to T = 292 K. In the rest of the room, the temperature ranges from T = 297 K to T = 299 K. Indeed, it is interesting to mention that the temperature difference between the floor and the head of the manikin is significant. This difference ranges from $\Delta T = 5$ K to $\Delta T = 7$ K and it was affirmed by different researches like Causone et al., [15] and Krajcik et al., [16]. As the result of this stratification, the indoor climate becomes discomfort [17]. For this reason, a temperature uniformity is required in order to maintain a healthy homogenous indoor environment.

4.2. Velocity Fields

Figure 9 shows the velocity fields in the planes defined by x = 0.2 m, x = 1.9 m, y = -0.1 m and y = 0.65 m. In accordance with these results, it has been observed that the biggest velocity values are shown in the inlet and outlet opening as presented in the plane x = 0.2 m and x = 1.9 m and it reaches $V = 0.2$ m.s^{-1}. Moreover, the planes defined by x = 0.2 m, y = -0.1 m and y = 0.65 m prove that the velocity remains highest around the sitting person and it ranges from $V = 0.11$ m.s^{-1} to $V = 0.17$ m.s^{-1}. The perturbation of the indoor air flow is observed due to the presence of the heat sources. As consequence, the recirculation zones are formed around the manikin and the computer. This non-homogeneity of the velocity inside the room causes the human thermal discomfort.

4.3. Static Pressure

Figure 10 shows the static pressure distribution in the planes defined by x = 0.2 m, x = 1.9 m, y = -0.1 m and y = 0.65 m. Based on these distributions, the

pressure stratification is observed in the occupied room. In the outlet opening, the atmospheric pressure is governed by the boundary conditions and it is equal to P = 0 Pa. Around the sitting person, it ranges from P = 2 Pa to P = 2.5 Pa. In the rest of the room, the pressure increases progressively. It reaches 3 Pa near to the walls, especially the west as shown in the planes defined by x = 0.2 m and x = 1.9 m.

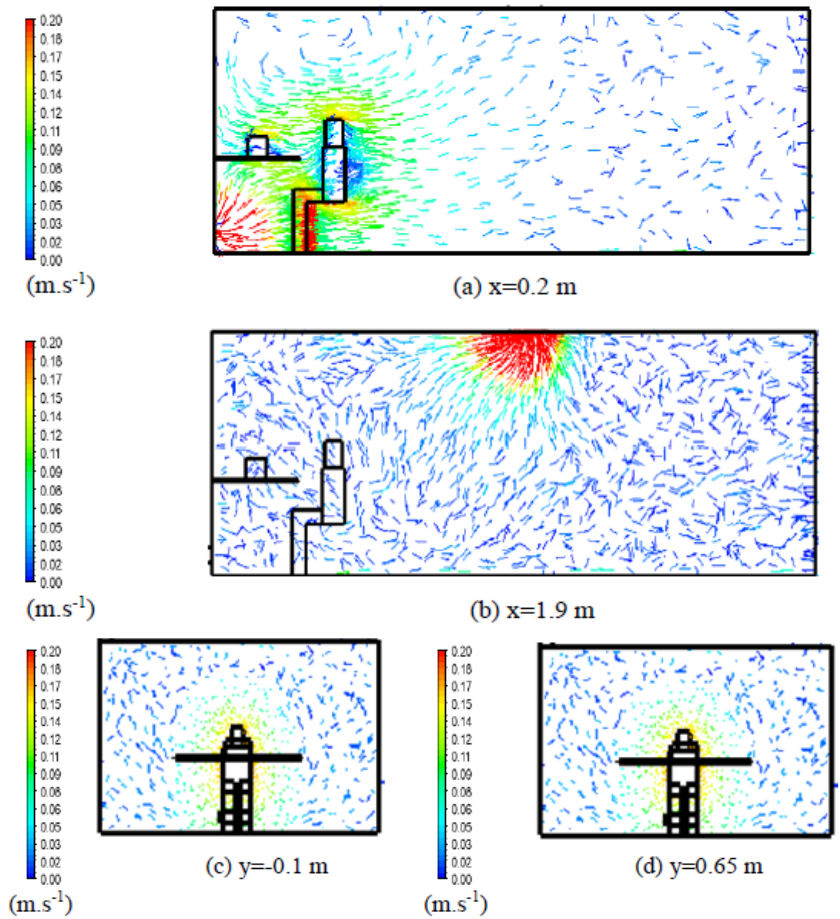

Figure 9. Velocity fields in different planes.

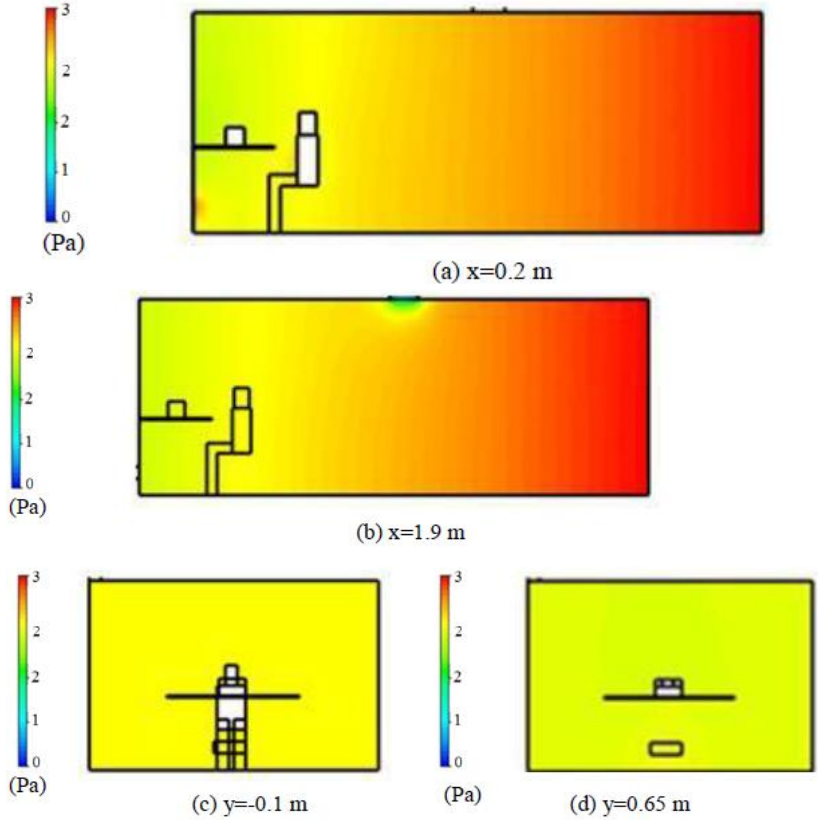

Figure 10. Static pressure distribution in different planes.

4.4. Turbulent Kinetic Energy

Physically, the dissipation of energy is made by the fluctuating viscosity stress. Hence, the production of the turbulent kinetic energy is defined in the characteristic equation of the turbulence models by the term G_k. Figure 11 displays the distribution of the turbulent kinetic energy in different planes defined by x = 0.2 m, x = 1.9 m, y = -0.1 m and y = 0.65 m. Eventuality, it has been observed that the turbulent kinetic energy ranges from $k = 8\ 10^{-5}$ J.kg^{-1} to $k = 1.1\ 10^{-4}$ J.kg^{-1}. The planes identified by x = 0.2 m and y = 0.1 m show that this energy cannot rise above $k = 9.62\ 10^{-5}$ J around the computer and the manikin.

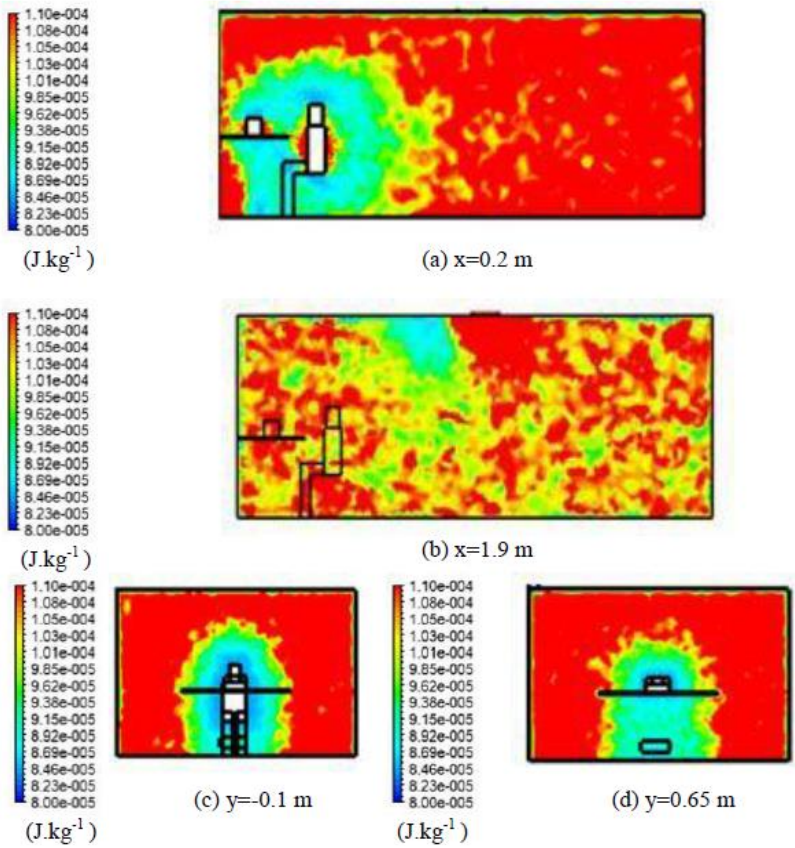

Figure 11. Turbulent kinetic energy distribution in different planes.

4.5. Dissipation Rate of the Turbulent Kinetic Energy

The dissipation rate of the turbulent kinetic energy presents the speed of the conversion of the turbulent kinetic energy in the internal thermal energy. In consequence, it is considered as one of the turbulence characteristics. Figure 12 presents the distribution of the dissipation rate of the turbulent kinetic energy for the four planes defined by x = 0.2 m, x = 1.9 m, y = -0.1 m and y = 0.65 m. Based on these results, it has been noted that the dissipation rate of the turbulent kinetic energy is more important in the inlet and outlet opening where it attains its peak that is equal to $\varepsilon = 2\ 10^{-4}\ m^2.s^{-3}$. Away of these zones, the dissipation rate of the turbulent kinetic energy is lower than $\varepsilon = 3.5\ 10^{-5}\ m^2.s^{-3}$.

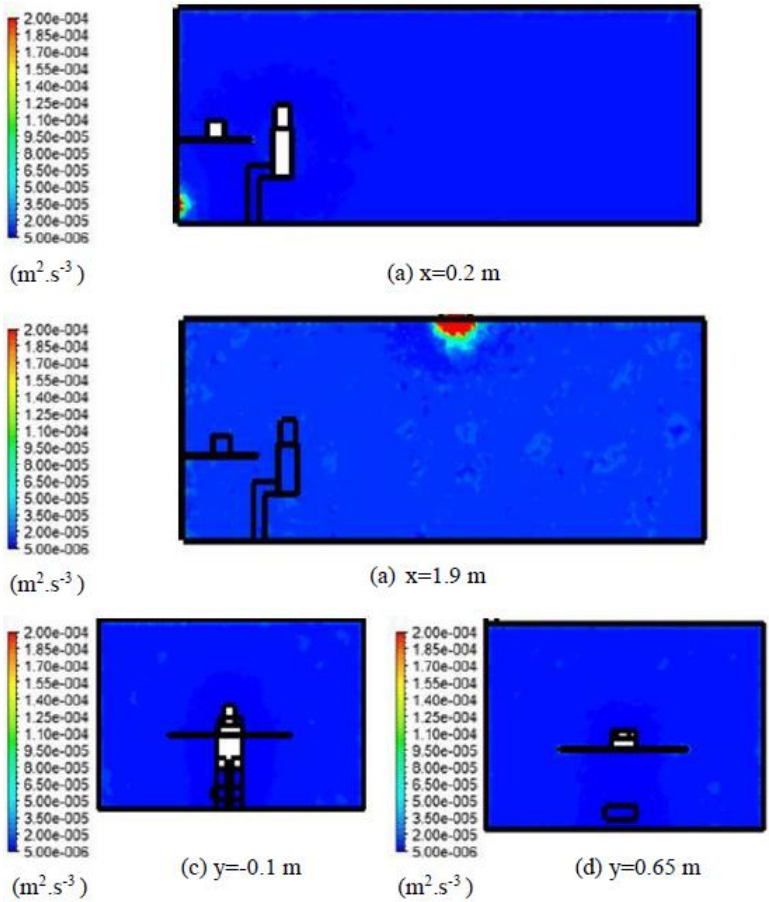

Figure 12. Dissipation rate of the turbulent kinetic energy distribution in different planes.

4.6. Turbulent Viscosity

Figure 13 shows the distribution of the turbulent viscosity in the different planes defined by x = 0.2 m, x = 1.9 m, y = -0.1 m and y = 0.65 m. For the RNG k-ε model, the turbulent viscosity is expressed as a function of the turbulent kinetic energy. Indeed, it is expressed by the friction of the internal fluid. As a result, there is a linear combination between the turbulent viscosity and the turbulent kinetic energy which explains the similarity between their

distributions. Therefore, the maximum values of the turbulent viscosity equal to $\mu_t = 1.7\ 10^{-4}$ Pa s are observed near the walls.

4.7. Thermal Index PMV

The thermal comfort is an important human necessity. It is a state of balance desired front the cold and warm sensation. In this sense, there are various thermal index like PMV (Predicted Mean Vote) that is the popular employed index. It was determinate by Fanger [18]. This index presents the combination between the ambient conditions, the human metabolism, the heat transfer coefficient and the clothes coefficient [19-24]. The PMV depends on the variation of the human metabolism (M, W), the air pressure p_a (bar) and the air temperature T_a (°C). Figure 14 presents the PMV evaluation in function of the temperature in the occupied zone. Based on these results, the PMV presents a linear variation and it can be expressed by this correlation equation:

$$PMV = 0.015T - 2.951 \tag{8}$$

According to the profiles shown in Figure 14, it has been cited that the PMV increases progressively in function of the augmentation of the indoor temperature. In addition, for the direction which is located between the two heat sources, this index ranges from PMV = 1.5 to PMV = 1.8. Whereas, it does not exceed PMV = 1.7 above and behind the manikin. Therefore, for the three directions the PMV is superior to 1. Based on the PMV scale shown in the Table 3, the climate is slightly warm. The indoor temperature can be considered as the most significant environmental factor. In this case, the highest dependence between the PMV comfort index and the temperature is demonstrated. Otherwise, it is necessary to maintain an indoor environment which does not help the development of the virus like the COVID-19.

Figure 15 presents the PMV profiles for the directions around the head person defined by y = 0.29 m, y = -0.1 m and z = -0.29 m. For the first direction which is in front of the person face, the PMV increases slightly until reaching PMV = 1.98 at z = 0.81 m and then it decreases. For the second direction, this index is rather high with a value equal to PMV = 2.06 then it declines gradually. Above the manikin head, the PMV ranges between 1.92 and 1.96. Overall, the PMV shows that the environment around the occupant head is warm (+2) but comfortable (+1).

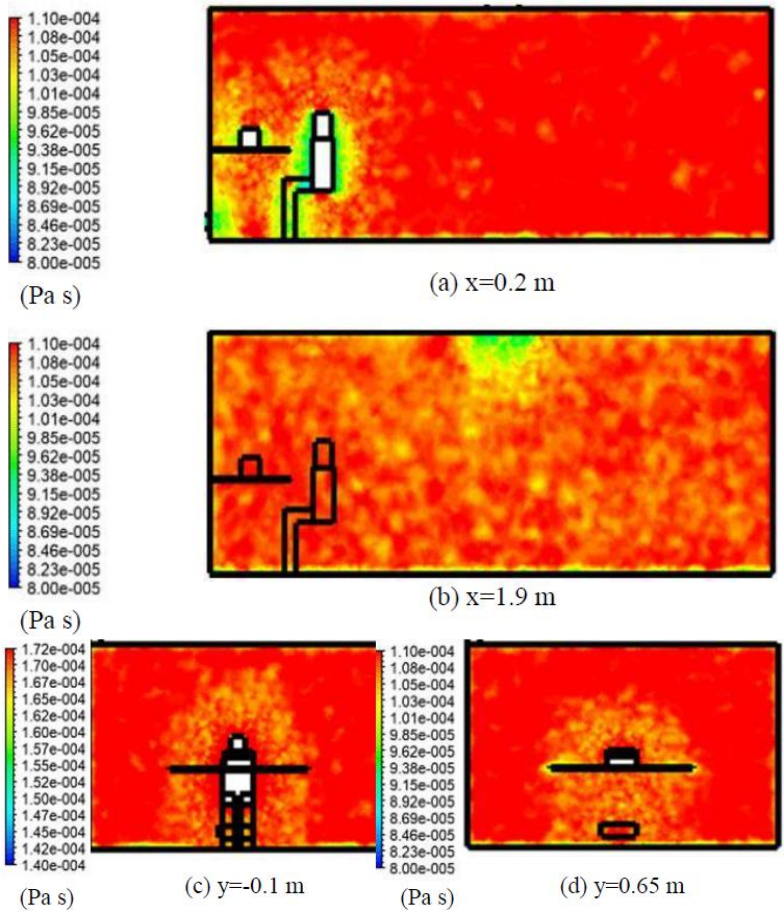

Figure 13. Turbulent viscosity distribution in different planes.

Table 3. PMV scale [18]

Sensation	PMV value
Much too hot	+3
Too hot	+2
Hot but comfortable	+1
Neutral	0
Cold but comfortable	-1
Too cold	-2
Much too cold	-3

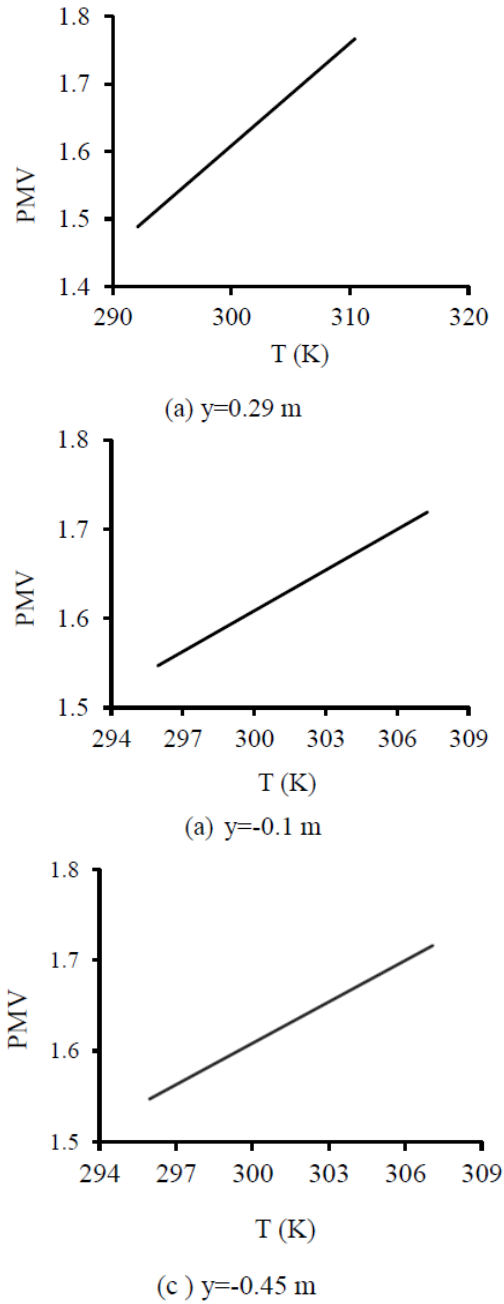

Figure 14. Profiles of PMV in function of the temperature along different directions in the plane x = 0.2 m.

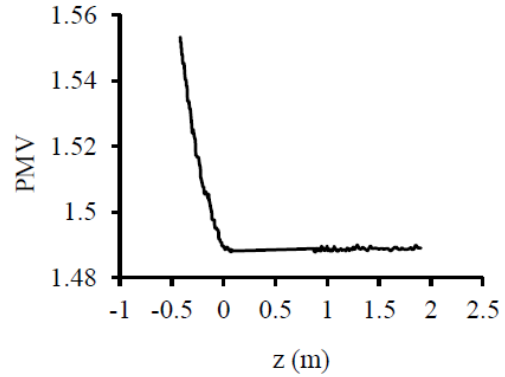

(a) y=0.29m

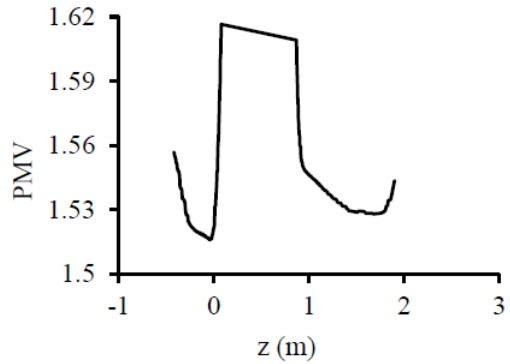

(b) y=-0.1 m

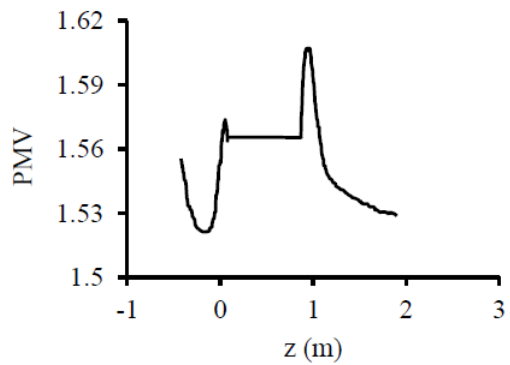

(c) y=-0.45 m

Figure 15. PMV profiles along different directions in the plane x = 0.2 m.

Conclusion

In this chapter, the impact of the numerical parameters inside a room containing two heat sources, which are the manikin and the computer, was tested. Numerical results given by the CFD tool were compared with the experimental results found in the literature confirm the good agreement with a meshing containing 216647 elements. In addition, the RNG k-ε turbulence model is considered as the most appropriate model. The PMV index shows that the indoor environment is hot but acceptable. In future works, it is recommended to improve the air conditioning conditions to attain the thermal comfort.

References

[1] Guo, Y., G. Zhang, J. Zhou, J. Wu and W. J. Shen (2012). "A techno-economic comparison of a direct expansion ground-source and a secondary loop ground-coupled heat pump system for cooling in a residential building." *Applied Thermal Engineering* 35: 29-39.

[2] Calay, R. K. and W. C. J. Wang (2013). "A hybrid energy efficient building ventilation system." *Applied Thermal Engineering* 57(1-2): 7-13.

[3] Murakami, S., S. Kato and J. J. Zeng (2000). "Combined simulation of airflow, radiation and moisture transport for heat release from a human body." *Building Environment* 35(6): 489-500.

[4] Zhai, Z. J., Z. Zhang, W. Zhang and Q. Y. j. Chen (2007). "Evaluation of various turbulence models in predicting airflow and turbulence in enclosed environments by CFD: Part 1 - Summary of prevalent turbulence models." *Hvac R Research* 13(6): 853-870.

[5] Zelensky, P., M. Barták, J. Hensen and R. Vavricka (2013). "Influence of turbulence model on thermal plume in indoor air flow simulation." *Proceedings of the 11th REHVA World Congress & 8th International Conference on IAQVEC* (CLIMA 2013), Energy efficient, smart and healthy buildings, Prague, Czech Republic, Citeseer.

[6] Mohammed, R. H. (2014). "Numerical investigation of displacement ventilation effectiveness." *International Journal of Environmental and Ecological Engineering* 8(2): 250-255.

[7] Chen, Y., J. Wang, F. Xiong, W. Liang, S. Wang and P. Ding (2015). "Characteristics of human body micro-thermal environment under displacement ventilation." *Procedia Engineering* 121: 1375-1381.

[8] Xu, Y., X. Yang, C. Yang and J. Srebric (2009). "Contaminant dispersion with personal displacement ventilation, Part I: Base case study." *Building and Environment* 44(10): 2121-2128.

[9] Ahmed, A. Q., S. Gao and A. K. J. Kareem (2017). "Energy saving and indoor thermal comfort evaluation using a novel local exhaust ventilation system for office rooms." *Applied Thermal Engineering* 110: 821-834.

[10] Fluent, A. (2017) 14.5, *Theory Guide, ANSYS*. Inc, Canonsburg, PA

[11] Ifa, S., Driss, Z. (2021). "Experimental study of indoor air quality for cooling condition using ARDUINO system and PMV index testing the effect of heat sources." *International Journal of Air-Conditioning and Refrigeration*, 29(3), 1-8. https://doi.org/10.1142/S2010132521500218.

[12] Ifa, S., Driss, Z. (2021). "Numerical simulation and experimental validation of the ventilation system performance in a heated room." *Air Quality, Atmosphere and Health*, 14(2), 171-179. https://doi.org/10.1007/s11869-020-00923-6.

[13] Johnson, A., B. Fetcher and C. J. Saunders (1996). "Air movement around a worker in a low-speed flow field." *The Annals of Occupational Hygiene* 40(1): 57-64.

[14] Bjørn, E. and P. V. J. Nielsen (2002). "Dispersal of exhaled air and personal exposure in displacement ventilated rooms." *Indoor Air* 12(3): 147-164.

[15] Causone, F., F. Baldin, B. W. Olesen and S. P. J. Corgnati (2010). "Floor heating and cooling combined with displacement ventilation: Possibilities and limitations." *Energy Buildings* 42(12): 2338-2352.

[16] Krajčík, M., R. Tomasi, A. Simone and B. W. J. Olesen (2013). "Experimental study including subjective evaluations of mixing and displacement ventilation combined with radiant floor heating/cooling system." *Hvacr Research* 19(8): 1063-1072.

[17] ISO (2004). "Ergonomics of the thermal environment analytical determination and interpretation of thermal comfort using calculation of the PMV and PPD indices and local thermal comfort criteria, management," 2005, https://www.iso.org/standard/39155.html.

[18] ASHRAE (2017). "Thermal environmental conditions for human occupancy." *ANSI/ASHRAE Standard*, pp. 55-2017.

[19] Zhang, S., Cheng, Y., Oladokun, M. O., Lin, Z. (2019) "Subzone control method of stratum ventilation for thermal comfort improvement." *Build Environ* 149:39-47. https://doi.org/10.1016/j.buildenv.2018.11.041.

[20] Kong, X., Xi, C., Li, H., Lin, Z. (2019) "A comparative experimental study on the performance of mixing ventilation and stratum ventilation for space heating." *Build Environ* 157:34-46. https://doi.org/10.1016/j.buildenv.2019.04.045.

[21] Bashir, M. F., Benghoul, M., Numan, U., Shakoor, A., Komal, B. (2020) "Environmental pollution and COVID-19 outbreak : insights from Germany." *Air Qual Atmos Health*. https://doi.org/10.1007/s11869-020-00893-9.

[22] Zambrano-Monserrate, M. A. (2020) "Has air quality improved in Ecuador during the COVID-19 pandemic ? A parametric analysis." *Air Qual Atmos Health* 929-938. https://doi.org/10.1007/s11869-020-00866-y.

[23] Jiang, Y., Xu, J. (2020) "The association between COVID-19 deaths and short-term ambient air pollution/meteorological condition exposure: a retrospective study from Wuhan, China." *Air Qual Atmos Health*. https://doi.org/10.1007/s11869-020-00906-7.

[24] Sher, R., Usmani, S. A., Mahmoud, A., Thulasyammal, A., Pillai, T. R., Jhanjhi, N. Z., Hashem, I. A. T. (2020) "Air pollution and its health impacts in Malaysia: a review." *Air Qual Atmos Health* 13:1093-1118. https://doi.org/10.1007/s11869-020-00867-x.

Chapter 5

Evaluation of Airflow in Spaces Equipped with Vertical Confluent Jets Ventilation Systems

Eusébio Conceição[1], Mª Inês Conceição[2], João Gomes[3], Mª Manuela Lúcio[1] and Hazim Awbi[4]

[1]FCT, Universidade do Algarve,
Campus de Gambelas, Faro, Portugal
[2]Instituto Superior Técnico, Lisboa, Portugal
[3]CINTAL, Campus de Gambelas, Faro, Portugal
[4]School of Built Environment,
University of Reading, Reading, United Kingdom

Abstract

In this research the evaluation of airflow in spaces equipped with vertical confluent jets ventilation system is analyzed. The influence of the airflow rate in the airflow topology, namely the air velocity field and the air quality acceptable airflow rate, is analyzed. This vertical confluent jets ventilation system consists of two sets of 50 nozzles located in a horizontal inlet ventilation ducts system, placed on each of the opposite walls. The horizontal inlet ventilation ducts system is placed near the wall surface, at 1.8m high. The exhaust of the vertical confluent jets ventilation system is made in the lower area of a vertical duct placed in the central area of the occupation area. The exhaust area is placed at 1.5 m high. Three different airflow rates are analyzed. The first, second and third airflow rate guarantee an acceptable airflow rate, according to international standards, for 4.7, 5.8 and 7.0 persons. The two sets of 50 nozzles guarantee a uniform airflow at the bottom of the wall. For all

In: Indoor Air Quality
Editor: Robert M. Ridgway
ISBN: 979-8-88697-134-7

airflow rates, considering the current design, the air velocity field promotes good air distribution along the floor. The interaction between the different airflows in the occupied central zone causes an upward flow of air towards the exhaust zone.

Keywords: airflow, indoor air quality, Confluent Jets System, CFD

Introduction

The confluents jets ventilation (CJV) system, used as Heating Ventilating and Air Conditioning (HVAC) system, is utilized to improve the indoor air quality, thermal comfort and Draught Risk conditions of the occupants. The airflow, mainly with regard to air velocity field, influences the transport of contaminants inside the spaces and, therefore, indoor air quality conditions. The airflow, mainly with regard to air velocity field around the human body, influences the heat exchange by convection and, therefore, thermal comfort conditions. The airflow, particularly the air velocity fluctuations field, influences the air turbulent intensity in the bare sections of the human body and therefore the Draught Risk conditions.

The CJV system has a group of consecutive nozzles in its construction. In the work presented here, the CJV system has two groups of nozzles aligned in each of the rectangular ducts, installed at a height of 1.8m on opposite walls. In a CJV system, the inlet airflow takes a downward direction along the wall surface and is then distributed over the floor in the occupancy zone. In the central area of the occupied space, this airflow existing at floor level, under the exhaust system, tends to take an upward direction towards the exhaust duct. With this ventilation system, all contaminants released during the occupants' breathing process are transported directly to the exhaust system, thus improving indoor air quality conditions.

In this work, the airflow rate and the airflow field promoted by a CJV system are analyzed. The influence of airflow rate in achieving acceptable indoor air quality will be analyzed. The airflow field will be analyzed using the air velocity field obtained between the inlet and exhaust systems. Finally, the different airflow topologies used will also be analyzed.

Literature Review

The CJV system uses the airflow, promoted by one or more groups of nozzles, to improve thermal comfort and indoor air quality levels. Arghand et al. (2015) studied the airflow and the thermal comfort levels, Karimipanah et al. (2000) studied different air distribution systems, and Cho et al. (2008) analysed the CJV system and the displacement ventilation system. The airflow field, obtained inside the virtual room, is used to evaluate comfort conditions, particularly the thermal comfort, air quality and Draught Risk. Conceição et al. (1997a) carried out an experimental work in a bus cabin experimental chamber where the air velocity field, the air temperature field and the air turbulence intensity were measured, without occupants, in vertical planes of that cabin and, when occupied, in around the occupants. Other examples can be seen in Conceição et al. (2008a), work in which these kinds of experimental measurements were made in a real experimental classroom. In this work the air velocity, air temperature, air turbulence intensity, Draught Risk and air velocity fluctuations were measured. The measurements of these variables were carried out in vertical lines distributed throughout the classroom.

Several studies have been conducted on the area of CJV systems. Most of the studies conducted on the area of CJV systems fall into the category of experimental measurements (Yin et al., 2016; Arghand et al., 2015; Cho et al., 2008; Ghahremanian and Moshfegh, 2014a; Janbakhsh and Moshfegh, 2014a; Andersson et al., 2018), although some numerical works on this type of ventilation system are also available (Cho et al., 2008; Ghahremanian and Moshfegh, 2014a; Andersson et al., 2018; Ghahremanian and Moshfegh, 2014b; Janbakhsh and Moshfegh, 2014). In Yin et al. (2016), an experimental method was used to visualize and investigate the airflow characteristics of a square column attached ventilation mode, whose results show that this system has the advantages of mixing and displacement ventilation. Cho et al. (2008) had investigated the characteristics of wall confluent jets in a compartment through Computer Fluid Dynamics and experimental tests and concluded that this type of confluent jets has a greater spread over the floor than displacement flow. Similar conclusions are obtained in the experimental study developed by Janbakhsh and Moshfegh (2014a) in a mock-up office environment, where an acceptable draught in the occupied zone was also found. Good indoor environment with lower energy consumption (Andersson et al., 2018) and better performance than the conventional mixing systems (Arghand et al., 2015) can be obtained with CJV systems.

The thermal comfort indexes, developed by Fanger (1970) and presented in ISO 7730 (2005) and in ASHRAE 55 (2017), take into account the values of the air velocity, air temperature, air relative humidity and Mean Radiant Temperature measured around the occupants. Using the indexes proposed by Fanger (1970), and the adaptive thermal comfort concept, Conceição et al. (2010) evaluated the levels of thermal comfort existing in a school building with complex topology. In this study, the environmental variables and the thermal comfort indexes were numerically evaluated.

The airflow rate and the airflow topology are used in the indoor air quality evaluation. ASHRAE 62.1 (2016) defines the acceptable airflow rate depending, mainly, on the occupancy level, used tracer gas techniques, based on the concentration decay method and the pulse injection method, to assess the most suitable airflow rate in a passenger compartment of a bus. The airflow rate obtained using the tracer gas concentration method serves to assess whether the indoor air quality is acceptable as proposed in international standards (ASHRAE 62.1, 2016).

The Draught Risk index was developed by Fanger et al. (1988), being also presented in ISO 7730 (2005). This index depends on the values of air velocity, air temperature and air turbulence intensity obtained around the different sections of the human body.

The work of Conceição et al. (2018) used a virtual classroom, equipped with a desk-type personalized ventilation system, to assess the Draft Risk, as well as to obtain their fields of air temperature, air velocity and carbon dioxide concentration. In order to evaluate the airflow field a numerical software, developed by the authors, is used.

Building Thermal Modelling (see Conceição and Lúcio, 2010), and the coupling of the Human Thermal Modelling (see Conceição and Awbi, 2021) and the Computational Fluids Dynamics (see Conceição et al., 2008b) are used to evaluate, respectively, the surrounding room surfaces, the human body temperatures distribution and the airflow variables around the occupants and inside the occupied spaces.

Method

Numerical Method

The software considers three numerical models (next page):

- Building Thermal Modelling;
- Human Thermal Modelling;
- Computational Fluids Dynamics.

The Building Thermal Modelling is used to calculate the surrounding surfaces temperatures of the virtual chamber and the inlet and exhaust airflow rate (with air velocity). These surrounding surfaces geometry and temperatures and the airflow rate are used as input values for the Computational Fluids Dynamics. The surrounding surfaces geometry and temperatures, using the human body surfaces geometry and temperatures, are used to calculate the Mean Radiant Temperature (through the view factors) to which the human body sections are subjected (used by the Human Thermal Modelling).

The Human Thermal Modelling is used to evaluate the temperature of the skin, blood and clothing and to evaluate the water in the skin and in the clothing. The surface temperatures and clothing temperatures are used by the Computational Fluids Dynamics as input data.

The Computational Fluids Dynamics is used to evaluate the environmental variables around the occupants and inside the virtual chamber. The human body surrounding air temperature and air velocity are used as input data in the Human Thermal Modelling.

Numerical Methodology

This numerical study presents a virtual chamber equipped with a vertical CJV system (Figure 1) that has an inlet system (whose airflow is represented in green in Figure 1) and an exhaust system (whose airflow is represented in red in Figure 1).

This vertical CJV system consists of two groups of 50 nozzles placed in each of the horizontal ducts of the inlet system existing on opposite walls (see Figure 1).

The horizontal ducts of the inlet system are mounted close to the wall surface at a height of 1.8m. The exhaust of the vertical CJV system is done through the lower area of the vertical duct installed in the center of the occupied area and connected to the ceiling (see Figure 1). The lower area of the exhaust duct is 1.5m high.

Table 1. Air velocity and airflow rate in the inlet system

Inlet air velocity (m/s)	Nozzle airflow rate (m^3/s)	Airflow rate (m^3/s)	Airflow rate (m^3/h)	Number of people with acceptable IAQ
8	0.000226	0.0452	162.86	4.7
10	0.000283	0.0565	203.57	5.8
12	0.000339	0.0679	244.28	7.0

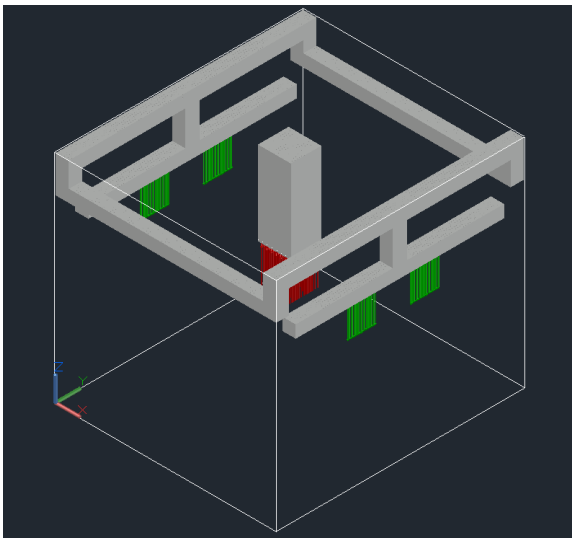

Figure 1. Scheme of the virtual chamber equipped with an inlet system (airflow represent in green) and an exhaust system (airflow represent in red).

Results and Discussion

In this section, the airflow fields for inlet air velocities of 8m/s and 12 m/s in planes placed at 0.076m, 0.202m, 0.704m and 1,225m in the X direction are presented. The airflow fields obtained for an inlet air velocity of 8m/s are shown between Figures 2 and 5, while for an inlet air velocity of 12m/s they are shown between Figures 6 and 9. The results obtained for the plane placed at 0.076m are presented in Figures 2 and 6, for the plane placed at 0.202m they are presented in Figures 3 and 7, for the plane placed at 0.704m they are presented in Figures 4 and 8, and for the plane placed at 1.225m they are shown in Figures 5 and 9.

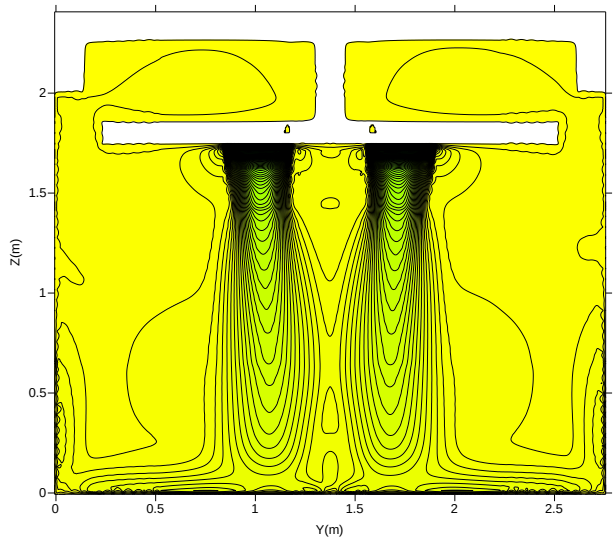

Figure 2. Field of the airflow, in a plane placed at 0.076m in the X direction, for an inlet air velocity of 8m/s.

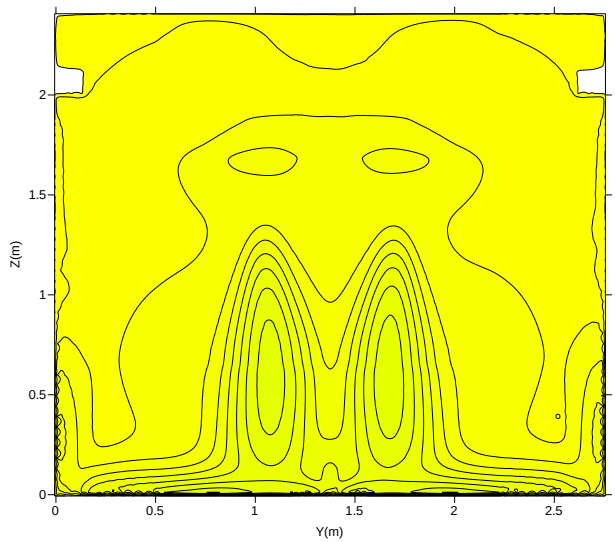

Figure 3. Field of the airflow, in a plane placed at 0.202m in the X direction, for an inlet air velocity of 8m/s.

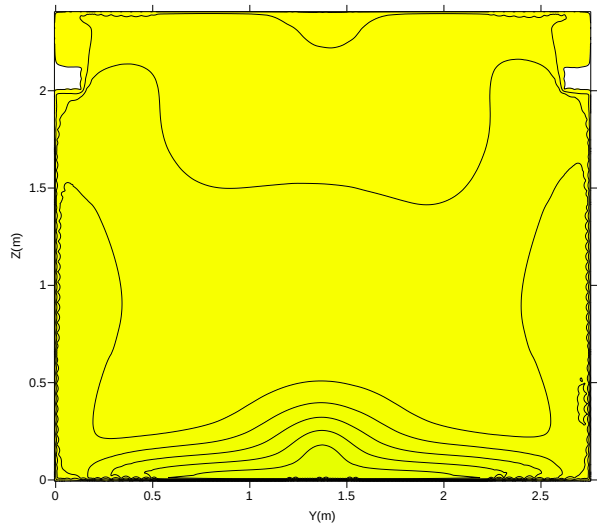

Figure 4. Field of the airflow, in a plane placed at 0.704m in the X direction, for an inlet air velocity of 8m/s.

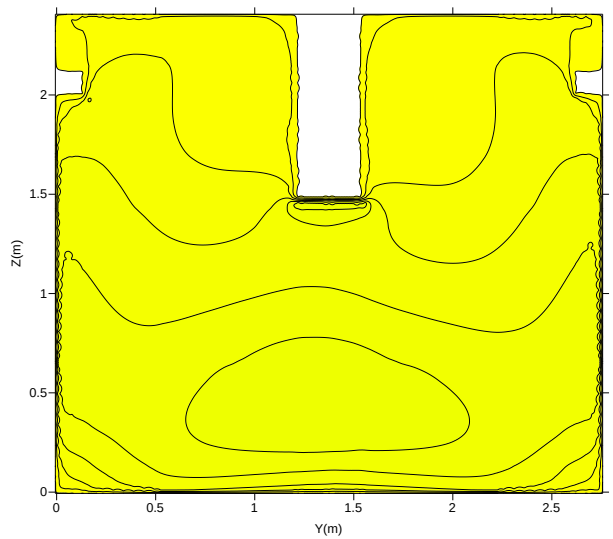

Figure 5. Field of the airflow, in a plane placed at 1.225m in the X direction, for an inlet air velocity of 8m/s.

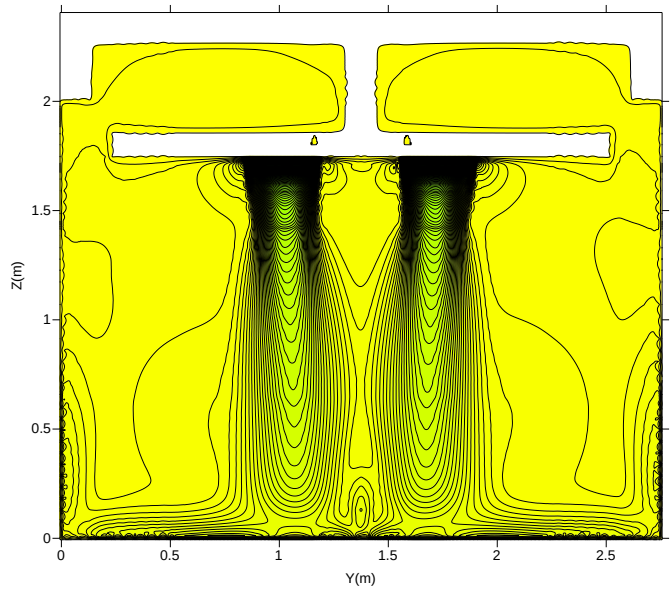

Figure 6. Field of the airflow, in a plane placed at 0.076m in the X direction, for an inlet air velocity of 12m/s.

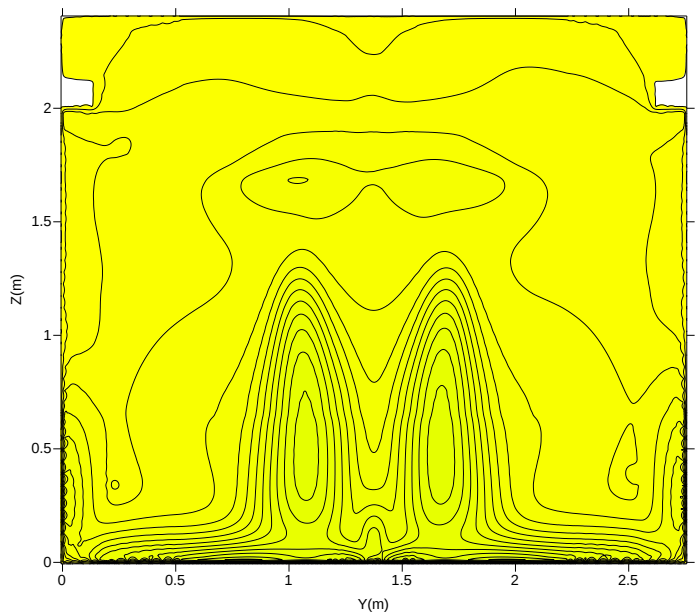

Figure 7. Field of the airflow, in a plane placed at 0.202m in the X direction, for an inlet air velocity of 12m/s.

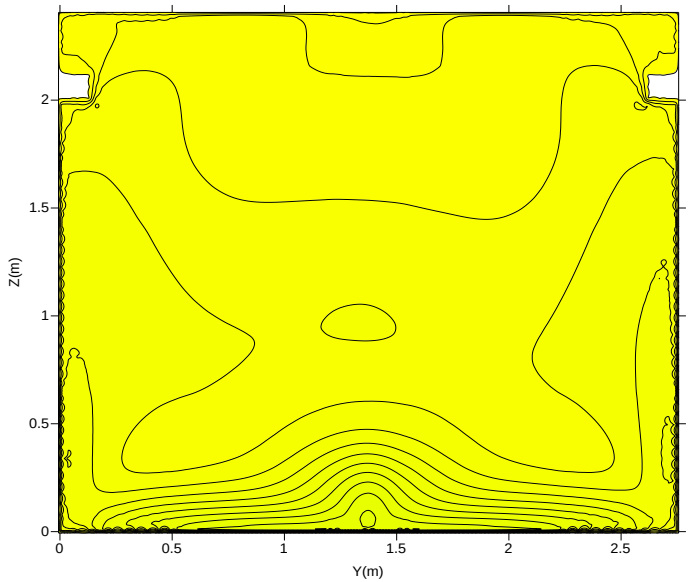

Figure 8. Field of the airflow, in a plane placed at 0.704m in the X direction, for an inlet air velocity of 12m/s.

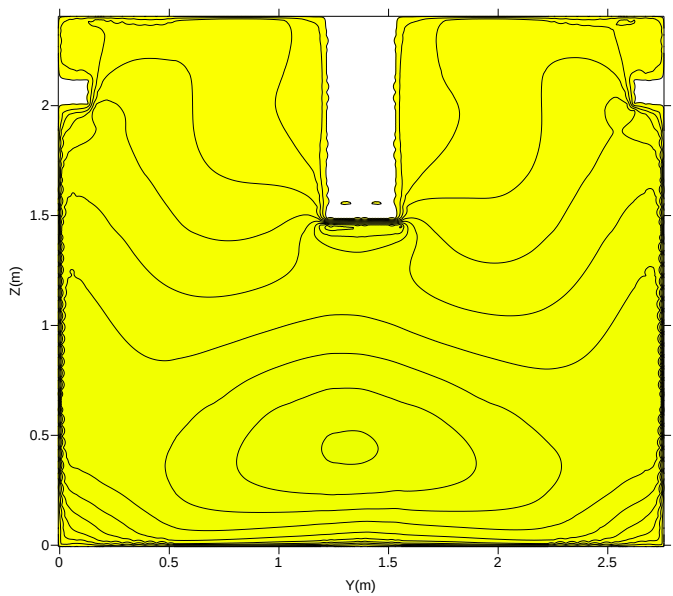

Figure 9. Field of the airflow, in a plane placed at 1.225m in the X direction, for an inlet air velocity of 12m/s.

According to the results obtained, it appears that there is an interaction of the jets of the two nozzles groups from the upper area of the wall. The jets of these two groups of nozzles, located in the horizontal ducts of the inlet system, ensure an even distribution of airflow in the lower area of the wall. As the inlet airflow increases, the air velocity at the bottom of the wall increases. In this case, the air velocity of the downward flow, in the direction perpendicular to the wall, increases the influence of the airflow in the occupied zone. The air velocity field, for all airflows considered, provides a good distribution of the airflow along the floor surface. As the inlet airflow increases, the air velocity at the floor surface increases.

The interaction between the airflows in the occupied central zone promotes an upward flow towards the exhaust zone. As the inlet airflow increases, the air velocity in the occupied zone increases.

Conclusion

In this work, the airflow distribution was evaluated inside a virtual chamber equipped with a vertical CJV system for three values of the inlet air velocity (8, 10 and 12m/s).

According to the results obtained, the airflow rate values used are acceptable for 4.7 occupants, for an inlet air velocity of 8m/s, for 5.8 occupants, for an inlet air velocity of 10m/s, and for 7.0 occupants, for an inlet air velocity of 12 m/s.

As the inlet airflow increases, the air velocity at the bottom of the wall increases and the airflow, in the direction perpendicular to the wall, increases the influence of the airflow in the occupied zone. All airflow rates provide a good distribution of airflow along the floor. The interaction between the airflows in the occupied central zone promotes an upward flow towards the exhaust area. When the inlet airflow increases, the air velocity increases in the occupied zone and close to the floor.

Therefore, due to the existence of airflow distributions with ascending characteristics in the occupied zone, the contaminants released in the breathing zone of the occupants can be transported to the exhaust zone.

Acknowledgment

The authors acknowledge to the project (70156-Safeair) from Algarve Regional Operational Program (CRESC Algarve 2020), under the PORTUGAL 2020 Partnership Agreement, through the European Regional Development Fund (ERDF).

References

Andersson H, Cehlin M and Moshfegh B. (2018). Experimental and numerical investigations of a new ventilation supply device based on confluent jets. *Building and Environment* 137, 18-33.

ANSI/ASHRAE Standard 55. (2017). *Thermal Environmental Conditions for Human Occupancy.* American Society of Heating, Refrigerating and Air-Conditioning Engineers: Atlanta, GA, USA.

ANSI/ASHRAE Standard 62-1. (2016). *Ventilation for Acceptable Indoor Air Quality*, American Society of Heating, Refrigerating and Air-Conditioning Engineers: Atlanta, GA, USA.

Arghand T, Karimipanah T, Awbi H, Cehlin M, Larsson U and Linden E. (2015). An experimental investigation of the flow and comfort parameters for under-floor, confluent jets and mixing ventilation systems in an open-plan office. *Building and Environment* 92, 48-60.

Cho Y, Awbi H and Karimipanah T. (2008). Theoretical and experimental investigation of wall confluent jets ventilation and comparison with wall displacement ventilation. *Building and Environment* 43(6), 1091-1100.

Conceição E, Silva M and Viegas D. (1997a). Airflow around a passenger seated in a bus. *HVAC&R Research* 3(4), 311-323.

Conceição E, Silva M and Viegas D. (1997b). Air quality inside the passenger compartment of a bus. *Journal of Exposure Analysis and Environmental Epidemiology* 7(4), 521-534.

Conceição E, Lúcio M, Vicente V and Rosão V. (2008a). Evaluation of local thermal discomfort in a classroom equipped with crossed ventilation. *International Journal of Ventilation* 7(3), 267-277.

Conceição E, Vicente V and Lúcio M. (2008b). Airflow inside school building office compartments with moderate environments. *HVAC&R Research* 195-207.

Conceição E and Lúcio M. (2010). Numerical study of the influence of opaque external trees with pyramidal shape on the thermal behaviour of a school building in summer conditions. *Indoor and Built Environment* 19(6), 657-667.

Conceição E, Nunes A, Gomes J and Lúcio M. (2010). Application of a school building thermal response numerical model in the evolution of the adaptive thermal comfort level in the Mediterranean environment. *International Journal of Ventilation* 9(3), 287-304.

Conceição E, Santiago C, Lúcio M and Awbi H. (2018). Predicting the air quality, thermal comfort and draught risk for a virtual classroom with desk-type personalized ventilation systems. *Buildings* 8(2), 35.

Conceição E and Awbi H. (2021). Evaluation of integral effect of thermal comfort, air quality and draught risk for desks equipped with personalized ventilation systems. *Energies* 14(11), 3235.

Fanger P. (1970). *Thermal Comfort: Analysis and Applications in Environmental Engineering*. Danish Technical Press, Copenhagen, Denmark.

Fanger P, Melikov A, Hanzawa H and Ring J. (1988). Air turbulence and sensation of draught. *Energy and Buildings* 12, 21-39.

Ghahremanian S and Moshfegh B. (2014a). A study on proximal region of low Reynolds confluent jets – Part 2: Numerical prediction of the flow field. *ASHRAE Transactions* 120, 271-285.

Ghahremanian S and Moshfegh B. (2014b). A study on proximal region of low Reynolds confluent jets – Part 1: Evaluation of turbulence models in prediction of inlet boundary conditions. *ASHRAE Transactions* 120, pp. 256-270.

ISO 7730. (2005). *Ergonomics of the Thermal Environments—Analytical Determination and Interpretation of Thermal Comfort Using Calculation of the PMV and PPD Indices and Local Thermal Comfort Criteria*. International Standard Organization, Geneva, Switzerland.

Janbakhsh S and Moshfegh B. (2014a). Experimental investigation of a ventilation system based on wall confluent jets. *Building and Environment* 80, 18-31.

Janbakhsh S and Moshfegh B. (2014b). Numerical study of a ventilation system based on wall confluent jets. *HVAC&R Research* 20, 846-861.

Karimipanah T, Sandberg M and Awbi H. (2000). A comparative study of different air distribution systems in a classroom. In: *Proceedings of 7th International Conference on Air Distribution in Rooms, ROOMVENT* 2000, 1013-1018, Elsevier, Amsterdam.

Yin H, Li A, Liu Z, Sun Y and Chen T. (2016). Experimental study on airflow characteristics of a square column attached ventilation mode. *Building and Environment* 109, 112-120.

Index

A

aerodynamic structure, 2, 40, 41, 87, 88
air pollutants, 53, 55, 59, 60
air pollution, xi, xii, 43, 44, 48, 49, 52, 55, 57, 58, 59, 60, 61, 114
air quality, xi, xii, xiii, xiv, 43, 44, 48, 53, 57, 59, 60, 61, 62, 89, 90, 92, 113, 114, 115, 116, 117, 118, 128, 129
air temperature, 3, 79, 107, 117, 118, 119, 120
airflow, ix, xi, xiii, 69, 76, 90, 91, 94, 112, 115, 116, 117, 118, 119, 120, 121, 122, 123, 124, 125, 126, 127, 128, 129
ambient air, xii, 43, 48, 53, 56, 114
aromatic hydrocarbons, 49, 60
atmospheric pressure, 6, 103

B

biological agents, 49, 51
biomonitoring, 49, 60
box prototype, xi, xii, 1, 4, 5, 8, 13, 17, 20, 24, 28, 32, 38, 39, 40, 63, 66, 67, 68, 69, 79, 80, 83, 85, 87

C

carbon, 54, 55, 62, 119
carbon dioxide, 55, 119
CFD, xiii, 2, 40, 64, 66, 67, 85, 87, 89, 90, 91, 92, 94, 112, 116
children, 44, 45, 46, 54, 56, 57, 58, 59, 60, 61
classroom, 51, 54, 55, 117, 119, 128, 129
Confluent Jets System, 116

D

draught, 118, 128, 129

E

energy, xii, xiii, 2, 7, 24, 27, 28, 37, 39, 41, 45, 64, 65, 66, 67, 71, 72, 74, 76, 81, 82, 85, 86, 89, 90, 91, 95, 98, 105, 106, 107, 112, 118
environment, xi, 2, 6, 38, 43, 44, 45, 48, 49, 51, 53, 56, 59, 60, 67, 86, 102, 108, 112, 113, 118, 128
environmental conditions, 44, 56, 114
European Commission, 46, 47, 58, 59
experimental validation, xii, 3, 41, 63, 66, 83, 84, 88, 113
exposure, xii, 43, 48, 53, 54, 59, 60, 113, 114

F

formaldehyde, 52, 53, 55

G

gaseous pollutants, 44

H

health, xii, 43, 44, 48, 51, 52, 53, 54, 55, 56, 58, 59, 60, 61, 91, 114
health effects, 44, 51, 52, 55, 58, 59
heat transfer, 6, 40, 87, 91, 102, 107
heat ventilation, xi, xii, 2, 39, 40, 63, 66, 67, 83, 84, 85, 87

human, xii, 43, 91, 102, 107, 112, 113, 114, 116, 119, 120

I

indoor air, xi, xii, xiii, 43, 44, 48, 52, 55, 57, 58, 59, 61, 89, 90, 91, 92, 102, 112, 113, 116, 117, 118
indoor air quality (IAQ), xi, xii, xiii, 43, 44, 49, 50, 52, 53, 55, 56, 57, 59, 61, 89, 90, 92, 113, 116, 117, 118, 120
indoors, xii, 43, 44, 53, 54, 55

M

manikin, 90, 92, 93, 94, 96, 102, 105, 108, 112

P

particulate matter (PM), 44, 49, 54, 55, 60, 62
PMV, xiii, 90, 92, 107, 108, 109, 110, 111, 112, 113, 129
pollutants, 44, 49, 50, 51, 53, 54, 55, 57, 59, 60, 91
pollution, iii, xi, xii, 43, 44, 48, 49, 52, 55, 57, 58, 59, 60, 61, 114

S

school, xii, 43, 44, 45, 46, 47, 48, 49, 50, 51, 52, 53, 55, 56, 57, 58, 59, 60, 61, 62, 118, 128
solar air heater, xi, 1, 2, 4, 5, 6, 7, 8, 12, 17, 20, 24, 28, 32, 38, 39, 40, 41, 85, 87
structure, 2, 40, 41, 48, 86, 87, 88
susceptible populations, xii, 43, 44
sustainable energy, xii, 2, 39

T

temperature, xii, xiii, 2, 3, 7, 12, 14, 15, 16, 35, 36, 37, 39, 52, 69, 76, 79, 89, 90, 93, 96, 98, 102, 107, 110, 117, 118, 119, 120
thermal comfort, xiii, 40, 67, 85, 87, 89, 90, 91, 92, 107, 112, 113, 114, 116, 117, 118, 128, 129
traffic emissions, 44, 54, 56
turbulence, xiii, 7, 39, 40, 63, 64, 65, 66, 68, 70, 72, 73, 74, 75, 76, 79, 81, 82, 83, 85, 86, 87, 90, 91, 92, 95, 98, 105, 106, 112, 117, 119, 129

V

velocity, xii, xiii, 2, 6, 7, 8, 10, 11, 12, 35, 37, 39, 65, 69, 75, 76, 89, 90, 91, 95, 96, 98, 102, 115, 116, 117, 118, 119, 120, 121, 122, 123, 124, 125, 126, 127
ventilation, ix, xi, xii, xiii, 1, 2, 39, 40, 51, 52, 57, 63, 66, 67, 83, 84, 85, 87, 89, 90, 91, 92, 94, 112, 113, 114, 115, 116, 117, 118, 119, 128, 129
viscosity, xiii, 7, 32, 34, 35, 64, 66, 72, 74, 76, 82, 84, 89, 90, 95, 98, 105, 107, 109

INDOOR AIR QUALITY

CONTROL, HEALTH IMPLICATIONS AND CHALLENGES

ROBERT M. RIDGWAY
EDITOR

nova
science publishers

www.novapublishers.com

ISBN-13: 979-8-88697-134-7